A Persistent-Mode MgB_2 0.5-T/240-mm Solid-Nitrogen-Cooled Magnet for MRI

by

Jiayin Ling

Submitted to the Department of Mechanical Engineering
in partial fulfillment of the requirements for the degree of

Doctor of Philosophy in Mechanical Engineering

at the

MASSACHUSETTS INSTITUTE OF TECHNOLOGY

February 2016

Signature redacted

Author .....
Department of Mechanical Engineering
January 14, 2016

Signature redacted

Certified by .....
Professor Yukikazu Iwasa
Thesis Supervisor

Signature redacted

Accepted by .....
Professor Rohan Abeyaratne
Chairman, Committee on Graduate Students

A Persistent-Mode MgB_2 0.5-T/240-mm Solid-Nitrogen-Cooled Magnet for MRI

by

Jiayin Ling

Submitted to the Department of Mechanical Engineering
on January 14, 2016, in partial fulfillment of the
requirements for the degree of
Doctor of Philosophy in Mechanical Engineering

Abstract

Magnetic resonance imaging (MRI) has become one of the major noninvasive diagnostic imaging tools today. The annual $5-billion market drives magnet engineers to develop advanced and innovative, high-quality, low-cost, easy-to-operate MRI magnets.

Because superconductors carry more than 100 times higher current density than copper, while generating no Joule heat, they are the only practical choice for diagnostic MRI magnets with field strengths above 1 T. A low-temperature superconductor of niobium titanium (NbTi) with a critical temperature of 9.8 K stands out among other superconductors because of its excellent mechanical properties, adequate electromagnetic properties and low manufacturing cost. Since the MRI magnet became available in the 1970s, most commercial superconducting MRI magnets have been of NbTi wire and operated in liquid helium bath at 4.2 K.

Nowadays, the sharply increasing price of helium has driven magnet designers to consider other superconductors with higher critical temperature for liquid-helium-free MRI magnets. Discovered in 2001, a new high-temperature superconductor of magnesium diboride (MgB_2) with a critical temperature of 39 K has spurred intensive R&D effort. A combination of high critical temperature, low manufacturing cost, and good in-field performance makes it viable competitor to NbTi and the basis for this thesis study.

This dissertation, a result of the 0.5-T/240-mm MgB_2 magnet project performed in the Magnet Technology Division of the Francis Bitter Magnet Laboratory, includes design, construction and operation details of the magnet. Each key component of the magnet, i.e., superconducting joint and persistent-current switch (PCS), was designed and tested to evaluate its performance. Each PCS was designed also to absorb energy when protecting the magnet; its protection performance, as well as switching function, was evaluated before deployed. Each finished coil module was tested separately before assembled to complete the magnet. The magnet was operated in persistent-mode in the temperature range 10-15 K. During operation, this liquid-helium-free magnet was immersed in a volume of solid nitrogen that provided a needed thermal mass to

the magnet. Temporal and spatial field homogeneity are critical parameters of MRI magnets. Thus actual fields were measured and compared with the designed values to demonstrate its acceptability to MRI application. Operation also examined and validated a protection technique deployed for this magnet, as protection is one of the vital requirements of the superconducting magnet.

Thesis Supervisor: Professor Yukikazu Iwasa
Title: Head and Research Professor, Magnet Technology Division, Francis Bitter Magnet Laboratory

Acknowledgments

Immeasurable appreciation and deepest gratitude for the help and support are extended to the following persons who in one way or another have contributed in making this study possible.

Prof. Yukikazu Iwasa, my thesis advisor, first and foremost, for his great training in my research and guidance in my life. He shared his most insightful knowledge with me and helped me overcome difficulties in my research. He introduced me to a great job after graduation. He also shared extreme detailed and helpful comments and editing on this thesis, making this one a good integrity.

Dr. John Voccio, my closest colleague in this study, for his selfless help and advice. He generated great and simple solutions to tough problems. He accompanied me days and nights during tests and helped me finish them.

Dr. Juan Bascuñán, my senior colleague, for his endless support and encouragement. He helped me prepare all the necessary materials and devices for experiments. He also gave me great ideas and suggestions on tests.

Prof. Seungyong Hahn, my colleague and friend, for his encouragement and selfless advices. His encouragement always made me excited to continue this study. He also advised me how to become a successful researcher.

Prof. John G. Brisson and Prof. Leon R. Glicksman, my thesis committee members, for their talent ideas and comments on my research and corrections on this thesis.

Mr. Julio Colque and Mr. Peter Allen, and other technicians in our lab, for their excellent work on helping and assisting me in finishing this study.

Dr. Michael J. Tarkanian, manager of DMSE foundry, for letting me use their furnace to heat-treat the coils for my study.

My parents, for their endless love, encouragement and support. You are always my heroes.

Wenqing, my dearest, for her selfless sacrifice of her job opportunities to support me. Her love always encourage me to proceed.

My best friends, for their love and support. We spent a lot of happy hours together. Your friendship always warmed my heart in this chilly city.

And Luke, my son, for your presence that gives me utmost happiness. I believe that you will benefit more from superconductivity.

And all others not mentioned above, for your contribution in a way or other to the completion of this thesis.

During the 5-year journey at MIT, I was accompanied by so many great persons. I was not traveling alone. Thank you all.

Contents

List of Figures

List of Tables

Chapter 1

Introduction

1.1 Magnetic Resonance Imaging

Medical imaging is critical for quality health care for early detection and efficient treatment of disease and injury. Magnetic resonance imaging (MRI) has become one of the major noninvasive diagnostic imaging tools today. The annual $5-billion market [3] drives magnet engineers to develop advanced and innovative, high-quality, low-cost, easy-to-operate MRI units.

Because superconductors carry more than 100 times higher current density than copper, while generating no Joule heat, they are the only practical choice for ≥ 1 T MRI magnets. A low-temperature superconductor of niobium titanium (NbTi) with a critical temperature of 9.8 K stands out among other superconductors, because of its excellent mechanical properties, adequate electromagnetic properties and low manufacturing cost [4]. Since the MRI magnet became available in the 1970's, most commercial superconducting MRI magnets have been of NbTi wire and operated in helium bath at 4.2 K [5].

1.1.1 Number of MRI Units

Because MRI units are usually expensive due to their superconductors, cryogens and intellectual properties, MRI units, despite the high needs everywhere in the world,

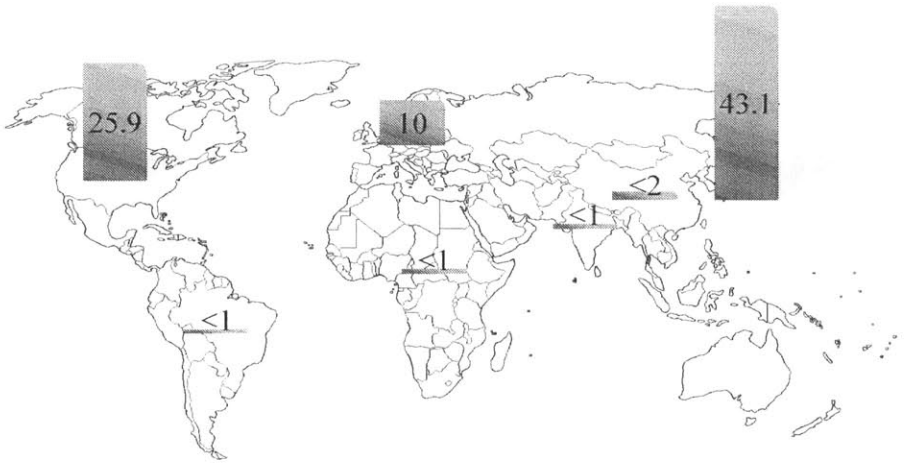

Figure 1-1: MRI units per million persons in selected regions of the world, including USA (2007 data), Japan (2008), Europe (2013), China (2012), India (2013), Africa (2013) and South America (2013).

concentrate in the developed countries. Figure 1-1 shows MRI units per million persons in selected regions of the world [6–8]. Japan has the highest MRI unit density of 43.1 (2008 data). The USA, the largest medical devices market, has a density of 25.9 (2007). In contrast, MRI densities are <2 in China (2012), and $\ll 1$ in India, Africa and South America (all 2013 data). These MRI densities demonstrate that there is big MRI market in the emerging countries.

There are many articles that report long waiting periods for MRI scans even in developed countries. For example, in Canada, the average waiting period for non-urgent patients is 84 days in 2015 [9]. Another article reported that, in France, an oncologic patient in need of an "emergent" MRI lumbar scan must wait an average of 38 days in 2014 [10]. These waiting days indicate that there is a shortage of MRI units to a certain extent even in developed regions of the world, not to mention an acute shortage in most of the world.

1.1.2 Cost of MRI

A 1.5-T whole-body MRI unit from the major manufactures costs around one million dollars. The high cost of MRI units is a major reason that limits for MRI units to proliferate more widely throughout the world. Cryogen, liquid helium (LHe) specifically

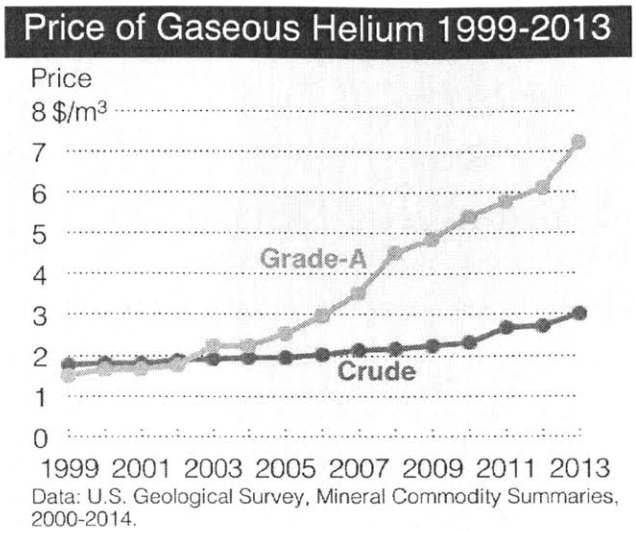

Figure 1-2: Helium price vs. year plots in 1999-2013.

to NbTi magnets, is one of the factors that drive the price of MRI high.

An MRI unit requires at least 2000 liters (L) of LHe filled in production facilities. In addition, helium slowly boils off during operation and needs to be replenished periodically. The price of helium varies quite much globally. In the US, the major helium source in the world, a liter of LHe costs \$10-20. In other continents, it can cost as high as \$30-50. The cost of helium alone contributes \$60,000-100,000 to the total price of an MRI unit.

Even in the US, the price of helium has been continuously rising in this century. The price of high purity gaseous helium in 2013 is almost four times of the 1999 price. And the rate of price rising, as seen from Figure 1-2, is accelerating. If the trend continues, the helium price will double in 10 years, which will drive MRI price even higher.

In addition to the helium cost, the required operating temperature of 4.2 K for NbTi consumes a large amount of cooling power, which contributes a significant portion to the operational cost of MRI units. Assume a cooling power of 10 kW is needed by an MRI unit to maintain 4.2 K environment for its NbTi magnet, an MRI unit consumes a total of $\sim$1,000,000 kWh during a 10-year lifetime. If the electricity rate is \$0.1 per kWh, the cooling cost of an MRI unit in its lifetime can be as high as

$100,000. By increasing the operating temperature from 4.2 K to 15 K, the required cooling power can nearly be halved.

1.2 Liquid-Helium-Free Option

Nowadays, the sharply increasing price of helium has opened a new opportunity for superconductors, e.g., MgB_2 is unquestionably more easily adoptable to LHe-free operation than NbTi. Adopting LHe-free option and bringing up the magnet operating temperature from 4.2 K to 10-15 K could save altogether $100,000-$150,000. This saving would make secondhand MRI machines—a 1.5-T unit typically ranges $300,000-500,000—more affordable in developing regions than their LHe rivals.

1.2.1 High Temperature Superconductors

In the mid 1980's, Müeller and Bednorz discovered a complex superconducting compound, consisting of copper, oxygen and rare earth elements [11]. This discovery opened the gate to discovering high temperature superconductors (HTS). In the following few years, many similar compounds were discovered to be superconductors, and the critical temperature records were broken again and again. In the early 1990s, two compounds of this family, $Bi_2Sr_2Ca_2Cu_3O_{10+x}$, known commonly as Bi2223 (critical temperature 110 K) and $YBa_2Cu_3O_{7-x}$, YBCO (critical temperature 93 K) [12, 13], have successfully been transformed into marketplace conductors. These two superconductors perform well in high magnetic field, i.e., their critical currents are sufficient even at high fields. However, the prices of these two superconductors are still one to two orders of magnitude higher than the price of NbTi, making them noncompetitive for most applications in which NbTi suffices.

Discovered in 2001, a new HTS of magnesium diboride (MgB_2) with a critical temperature of 39 K has spurred intensive R&D effort [14]. For applications below 3 T, a combination of high critical temperature, low manufacturing cost, and good in-field performance makes MgB_2 a viable and promising competitor to NbTi. The higher critical temperature makes an MgB_2 magnet suitable to operate, for example,

in solid nitrogen (SN2) in the 10-20 K temperature range. Note that in the range 10-20 K, SN2 enthalpy density is >10 times greater than those of metals, making an MgB_2-SN2 system operating in the 10-20 K range to possess a thermal mass density far greater than a conduction-cooled system. Even without SN2, MgB_2 will operate at 10-20 K much more stably than NbTi at 4.2 K, simply because of its higher critical temperature and higher enthalpy density compared with NbTi.

Since MgB_2 wire and tape became commercially available, people from both industry and academia have shown interests in building MRI magnets with MgB_2 wires/tapes. Stenvall *et al* built a react-and-wind solenoid with 46-m commercial MgB_2 tape from Columbus Superconductors [15], exploring the technologies for cryogen-free MgB_2 magnet. Zhang *et al* [16,17] made a 2-solenoid magnet with 60-m long MgB_2 wire to investigate its thermal stability. Their magnet generated 1-T field at its center at 290 A. In another study, Li *et al* made a 1.5-T MgB_2 magnet to explore its thermal stability and quench characteristics [18]. They also built a few prototype MgB_2 coils to explore the feasibility of persistent-mode magnets with wind-and-react procedure [19]. Mine *et al* have reported their development of a 3-T 250-mm-bore MgB_2 magnet system with react-and-wind procedure [20,21]. A 6-coil magnet system was built, but they found large "remnant" voltages in the coils, which impaired persistent-mode operation. Paramed, a company in Genoa, Italy, has commercialized a 0.5-T MRI system of a driven-mode MgB_2 magnet supplied by ASG Superconductors [22,23]. At Francis Bitter Magnet Laboratory, MIT, Yao *et al* reported a 10-coil 700-mm-bore MgB_2 magnet built with react-and-wound procedure, tested in SN2 in the range 10-15 K [24]. The magnet generated a center field of 0.54 T at 88 A. They also developed a technique to splice multifilamentary MgB_2 wires with a superconducting joint [25,26], which was later found to work more reliably with monofilament wire [27,28].

1.2.2 Helium-Free Cryogens

In the absence of LHe, an LHe-free magnet, comprising materials all of relatively low heat capacities even at 20 K, has practically no thermal mass. For thermally stable

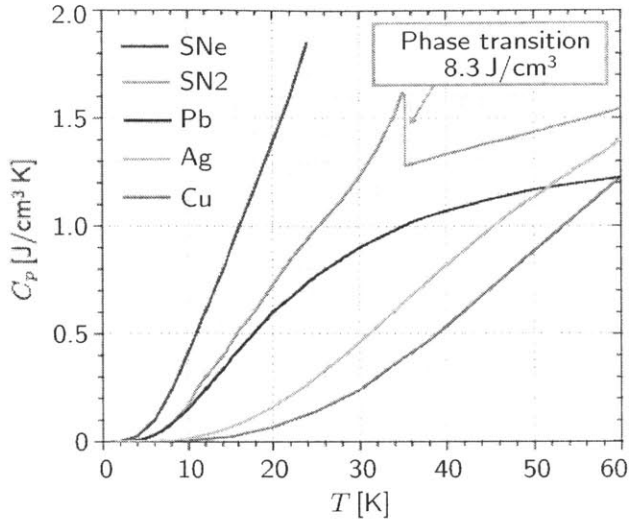

Figure 1-3: Heat capacities of major cryogenic materials, e.g., solid neon (SNe), solid nitrogen (SN2), lead, silver, and copper, at cryogenic temperature [1].

operation, it is desirable to enhance the thermal mass of an LHe-free superconducting magnet.

Figure 1-3, data from [1], plots the heat capacities of selected materials that are commonly considered as thermal mass enhancers. SN2 stands out of these materials due to the combination of its high heat capacity, light weight, low cost, and environmental safety. Solid neon (SNe), with a good heat capacity, is not a practical candidate because it is about 500 times more expensive than SN2. Liquid hydrogen (LH2), with melting point at 13.8 K and boiling point at 20.3 K in the right range, is another potential good competitor to SN2. However, in case of a magnet quench, the release of a large amount of gaseous hydrogen can cause significant hazard in hospitals. Thus, LH2 is an unsuitable cryogen for MRI.

In the presence of SN2, an MRI magnet is more thermally stable than a conduction-cooled "dry" magnet. And more importantly, in the event of power outage, SN2, an effective thermal reservoir, could keep the temperature of the magnet within its operating range for a certain period [29, 30].

1.3 Objectives

Research on MgB_2 MRI magnet has been actively conducted worldwide, chiefly to reduce the manufacturing and operational cost of MRI units and thus proliferate MRI scans. The objective of my thesis is to contribute in further advancing MRI magnet technology that specifically incorporates MgB_2 as a superconductor and SN2 as a thermal mass enhancer for LHe-free operation.

For my thesis work, I was assigned as the principal team member of an MgB_2 MRI magnet project at the MIT Francis Bitter Magnet Lab. The project had one specific aim: complete a solid-nitrogen cooled, persistent-mode 0.5-T center field and 240-mm bore MgB_2 magnet. As such, I was chiefly responsible for design and construction of most magnet components, which included persistent-current switches and superconducting joints, both indispensable elements for persistent-mode operation. Last but not least, I single-handedly assembled and successfully operated the magnet. The completion at our lab of such an innovative and first-ever persistent-mode MgB_2 magnet may be considered a major milestone in MRI magnet technology. I expect, and hope, that my thesis work will facilitate in promoting further R&D work in this technology and resulting in readily available MRI medical care everywhere, here and particularly in developing countries. I believe that such a great outcome will ultimately benefit the entire humanity.

Chapter 2

Design

2.1 Key Design Concepts

MRI magnets require high temporal stability of magnetic field. An acceptable field shift for a typical MRI magnet is <0.1 parts-per-million (ppm) per hour. If such a magnet is driven by a power supply, the power supply must maintain a highly stabilized current with fluctuations <0.1 ppm over a period of 1 hour. A high-stable power supply is not only an expensive extra cost to an MRI unit but also, most importantly, its cold-end terminals become another source of heat input to the cold environment. Therefore, all of the commercial NbTi MRI magnets operate in persistent mode. When operated in persistent mode, the superconducting joints of these magnets are able to restrict the decay of the current <0.1 ppm/hr. In order to be competitive with its NbTi rivals in terms of cost, an MgB_2 MRI magnet has to operate in persistent mode as well. Paramed, a company in Genoa, Italy, has already commercialized a 0.5-T MRI system with a driven-mode MgB_2 magnet supplied by ASG Superconductors. This reality demonstrates, from another aspect, that it is neither intellectually exciting nor innovative to develop another driven-mode MgB_2 superconducting magnet. It was decided that for this project the MgB_2 magnet would operate in persistent-mode. "Persistent-mode" is the first design principle.

A persistent-mode superconducting magnet requires a technique to make superconducting splices. Early in the project, the team developed a technique to splice

multifilament MgB_2 wires [25, 26]. Later, this splicing technique was proved to be much more repeatable with *monofilament* MgB_2 wires [27, 28]. In order to reduce the risk of wasting the entire magnet, the project team decided to make the magnet wound with monofilament wire terminated with more reliable splices of monofilament wires. "Monofilament" is the second design principle.

The splicing technique has been developed to work with both unreacted and reacted MgB_2 wires. When it is applied to unreacted wires, however, it involves a simpler procedure and results in higher critical currents than that applied to reacted wires. So, because of the joints, it is preferable to wind the magnet with unreacted MgB_2 wires first, make joint between terminals, and then heat treat the magnet together with the joint, i.e., the wind-and-react procedure. In addition to the splicing technique, the mechanical property of MgB_2 wire is also suited to the wind-and-react procedure. MgB_2 behaves essentially as a ceramic and can be easily damaged by handling. It is risky to wind and handle the wire after reaction, because handling may cause small cracks in the MgB_2 core and degrade its critical current density. If the magnet is wound before reaction, no damage can be made to the core of the wire while it is still a mixture of magnesium and boron power. Thus, it is less risky and eventually perhaps more economical to employ the wind-and-react procedure. "Wind-and-react" is the third design principle.

Our wire supplier, Hyper Tech Research, Inc., could comfortably provide us monofilament MgB_2 wire of uniform-quality length up to about 300 m. A magnet generating 0.5 T uniformly over a 12-cm diameter spherical volume (DSV) requires wire much longer than 300 m. Thus, there are two options: 1) use superconducting joints to directly connect coils wound with <300 m wire; or 2) terminate each coil with its own superconducting joint and then connect coils with resistive joints. In Option 1 all coils need to be heat-treated at the same time. It is difficult to find a furnace big enough. Also, it is risky to heat treat the entire magnet in a single batch. Thus, Option 2 suitable for this magnet. If the magnet is damaged during heat treatment, handling or test, the damage is very likely within a single coil module or a few coil modules. The damaged modules can be replaced with healthy spare ones

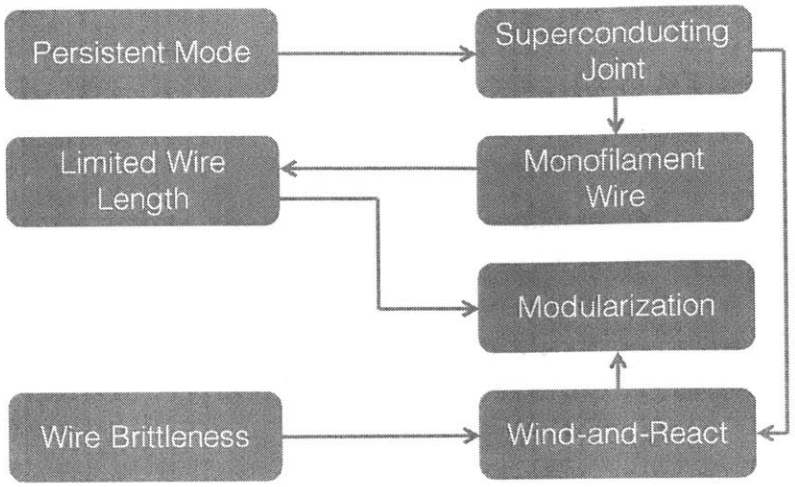

Figure 2-1: The key design concepts and logic of considerations.

to keep the entire magnet intact. In this way, the cost of making and repairing the magnet can be reduced. "Modularization" is the forth design principle.

I summarize the logic of considerations and list the key design concepts in Figure 2-1.

2.2 Electromagnetic Design

The magnet was designed principally by Dr. Seungyong Hahn based on the stated design principles. A schematic drawing of the magnet is shown in Figure 2-2. It consists of 8 coil modules, each of them containing wire <300 m. The magnet totally consumes 2.1-km long monofilament MgB_2 wire, manufactured by Hyper Tech. Each coil has a winding inner diameter of 276 mm and outer diameter of 290 mm. The total magnet height, including seven gaps, each 14-30 mm, between adjacent modules, is 460 mm. At 102 A, the magnet generates a center field of 0.5 T and at the same time a peak field of 0.7 T on its inner wall. A peak-to-peak field error in a 12-cm DSV is smaller than 200 ppm. The key parameters of the magnet are summarized in Table 2.1 [2].

The inner diameter of 276 mm of the magnet is sufficient for MR imaging human extremities, which has more and more clinical values nowadays. A center field of

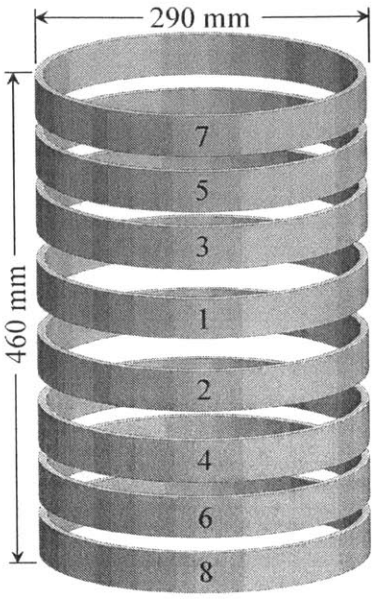

Figure 2-2: The electromagnetic design of the MgB_2 magnet. It consists of 8 coil modules; each module has its own PCS and superconducting joint.

Table 2.1: Magnet Key Parameters [2]

Parameter	Value
Inner Diameter	276 mm
Outer Diameter	290 mm
Total Height	460 mm
Operating Current	102 A
Center Field	0.5 T
Peak Field	0.7 T
Overall Current Density	11.3 kA/cm^2
Single Strand Length	<300 m
Total Conductor Length	2.1 km
Field Error in 12 cm DSV	<200 ppm

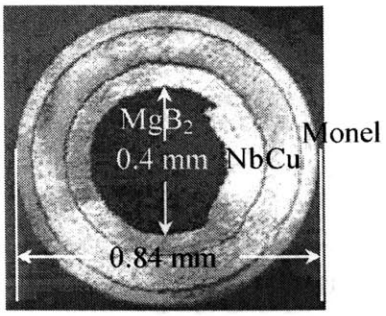

Figure 2-3: MgB_2 wire cross-section. From innermost to outermost: MgB_2, niobium, copper, and monel. Photo courtesy of Hyper Tech.

0.5 T is the low threshold of a superconducting magnet vs. its permanent magnet counterpart. Our magnet parameters were deliberately chosen so that the magnet can not only be operated in lab but also be used in an MRI clinic. In addition, the technologies developed for this magnet can be scaled up to build whole-body MRI magnets.

In order to maintain the electrical performance of the wire, the hoop strain in the wire should be smaller than 0.5% [31]. Using the simplest BJR-model to estimate the hoop stress with a Young's modulus of 100 GPa for MgB_2 wire [1], I computed a safe hoop strain smaller than 0.02%. Even if the magnet is upscaled to 1.5 T, the hoop strain 0.18%, 9 times larger than that of the 0.5-T magnet, is still well below the critical value.

2.3 Wire Selection

The Hyper Tech Φ0.84-mm bare monofilament MgB_2 wire consists, from inner most to outermost, of a Φ0.4-mm MgB_2 core, a 70-μm barrier layer of niobium to enclose MgB_2, a 100-μm layer of copper, and a 45-μm layer of Monel to provide mechanical strength. The copper layer takes about 35% of the total cross-sectional area of the wire. The wire is 1.0 mm with s-glass insulation. Altogether 12 reels of unreacted wire were purchased from Hyper Tech. A photo of the bare wire cross-section is shown in Figure 2-3.

The wire has self-field (i.e., no external field) critical currents, measured at FBML,

of >400 A current at 10 K and >200 A at 20 K. These numbers were measured here at FBML. Other properties of the wires can be found in literature [32,33]. The wires carry $\geq$ 100 A at around 15 K in the magnet.

2.4 Superconducting Joint

A joint was fabricated through the following steps: (1) etch the copper and Monel surrounding the filament with nitric acid (Figure 2-4a); (2) shear filament at an acute angle (Figure 2-4b); (3) fill billet with pre-mixed Mg+B powder and insert copper plug into billet without pressure (Figure 2-4c); (4) insert the two wires side by side into the billet in the opening between the copper flat surface and billet (Figure 2-4d), aligning wires so that the angle-cut surfaces face each other (Figure 2-4e); (5) press the copper plug to partially seal the top of the billet; (6) use ceramic paste to further seal the top of the billet (Figure 2-4f). Since a Nb barrier layer protects the MgB_2 filament, if each wire was slit right angle to its axis, its end surface exposed to the Mg+B mixture ingot in the joint would be small. Therefore, each wire was cut at an acute angle to enlarge this contact area.

Figure 2-5 shows a summary of critical current results of 10 sample superconducting joints of monofilament MgB_2 wires. Critical currents were measured by the four-probe method. Figure 2-5 data show that all of the joints had acceptable (>100 A) critical currents at 15 K, in self field. Most of the joints had critical currents well above 100 A even at 20 K, which should suffice for use in this MgB_2 magnet.

For one of the best samples, its critical temperature was determined by measuring its resistance during cool- down. The resistance of the joint is plotted vs. temperature in Figure 2-6, showing the onset of the superconducting transition is about 36 K. However, it is not fully superconducting above 32 K. This rather broad transition observed in the joint might be due to a slight difference in composition in the two wires and in the ingot. The steeper section may represent the transition of wire, while the gradual section may represent the transition of the joint.

Monofilament wire that works much more reliably with this splicing technique has

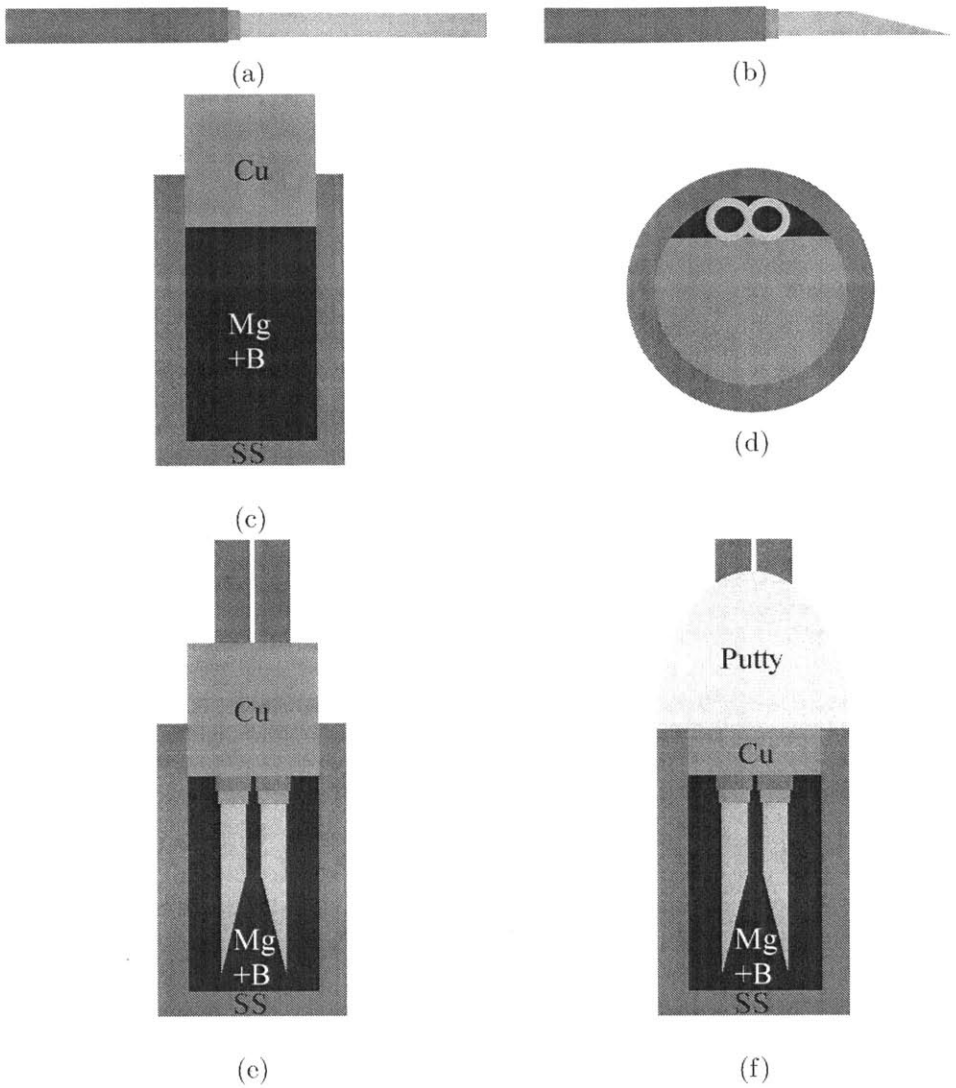

Figure 2-4: Schematic drawings of splicing process. (a) etch wire; (b) shear wire; (c) fill powder; (d) insert wires; (e) align wires; (f) seal joint.

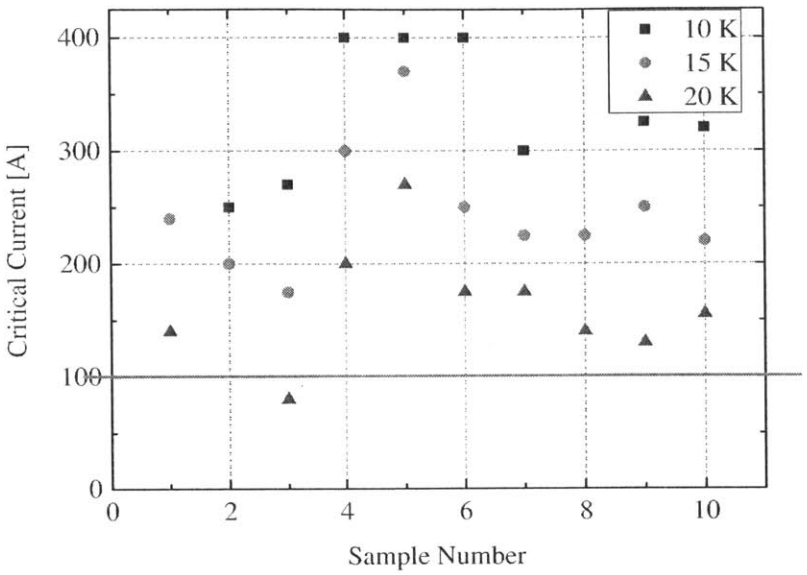

Figure 2-5: Self-field critical currents of 10 sample superconducting joints samples at 10 K, 15 K, and 20 K.

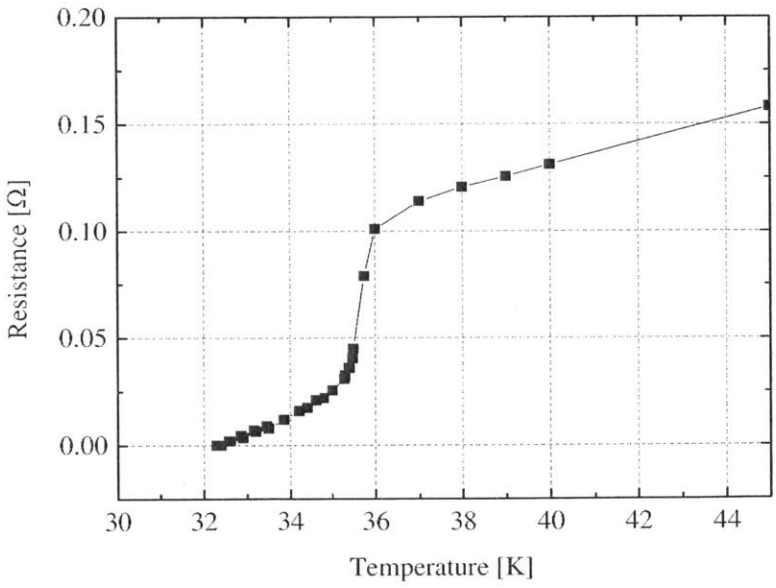

Figure 2-6: Superconducting transition of an MgB_2 joint.

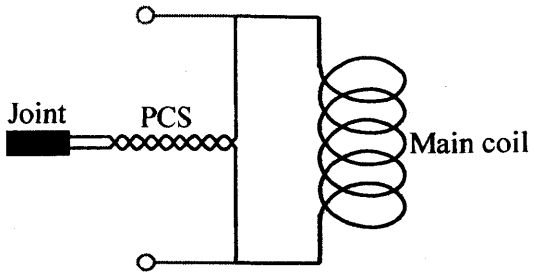

Figure 2-7: A circuit diagram of a coil module. Each coil has its own persistent-current switch (PCS), terminated with a superconducting joint.

two issues that multifilament wire does not have: higher chance of flux jumping and larger screening current field (SCF). This is because magnetization is proportional to filament size [1]. For magnet applications, including MRI, NbTi wire usually consists of many filaments, each diameter of a few micrometers. At this filament size flux jumping is effectively eliminated. The MgB_2 wire used in this magnet has a filament diameter of $\sim$400 μm, about two orders of magnitude greater than its NbTi counterpart. I have demonstrated in my masters thesis, with both short samples and sample coils, that flux jumping does not exist in this monofilament MgB_2 wire [34]. The SCF of this magnet was measured and discussed in Chapter 5.

2.5 Coil Connection

Because of the reasons stated in Section 2.1, we manufactured coil modules individually and assemble them to complete the magnet. So, each coil module has its own persistent current switch (PCS) and superconducting joint and forms a complete superconducting loop. In a coil module, the PCS and the joint were made of the same continuous wire used to wind the main coil. The two end wires from the main coil were non-inductively co-wound into the PCS. Then, the two ends from the PCS were spliced to form a superconducting joint. Two terminals were placed between the PCS and main coil to connect to the neighboring coils or a power supply. A circuit diagram of a single coil module is shown in Figure 2-7.

Figure 2-8 shows a circuit diagram of the 8 coil modules for this magnet. The

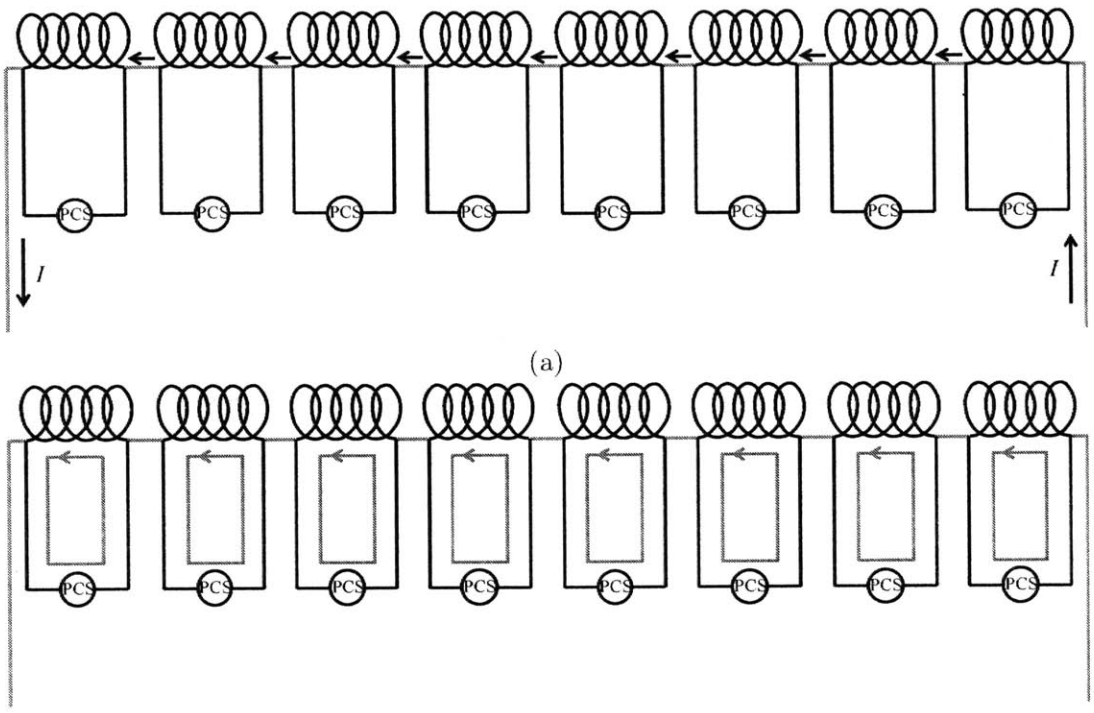

Figure 2-8: Circuit diagrams of 8 coil modules connected in series. Red lines indicate resistance. (a) PCS's open, the coil modules may be charged. (b) PCS's closed, persistent current loops may be sustained in coils.

joints are omitted in this circuit diagram. Each coil was connected to other coils or the power supply via its terminals that were between the main coil and PCS. These connections, different from the superconducting joint in each coil, are resistive. When we charge or discharge the coil, we open all 8 PCS's—each PCS in the resistive stage—and the 8 coils are connected in series, effectively, as shown in Figure 2-8a. When we reach the target current, we close all of the PCS's and then gradually reduce the supplied current and remove the external power supply. A persistent current will then be sustained in each coil, as shown in Figure 2-8b.

Though the connections between coils are resistive, they do not cause current to decay when the magnet is operated in persistent mode. When the magnet is operated in persistent mode, each coil module sustains a persistent current individually in its superconducting loop, keeping the magnet field in persistent mode.

When we energize the magnet, we should keep the supplied current at the target value for a period that is a few times longer than the time constant of the magnet-PCS circuit. By doing this, the bypass current in each PCS will reduce to essentially 0 so that the current in each coil will equal exactly to the supplied current. When we close the PCS's and remove the power supply, each coil will sustain the same current that equals the supplied current. Because the mutual inductances between coils are different, if current in a coil decays, the currents in the other coils will change differently. But, since all coil modules are superconducting, the currents in them are not expected to decay while the magnet is normally operated.

2.6 Persistent Current Switch

2.6.1 Location

In this magnet, each coil module has its own PCS, and the PCS must be heat treated together with the rest of the winding, including a joint. The PCS has to be placed close to the main winding so that later the entire module can be heat treated and assembled easily. There are two options to place the PCS: concentric or aside, as

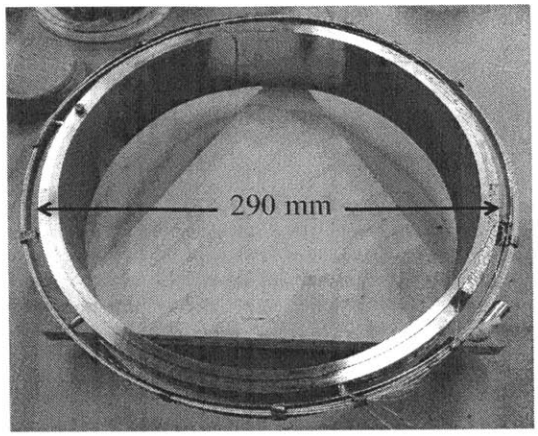

(a)

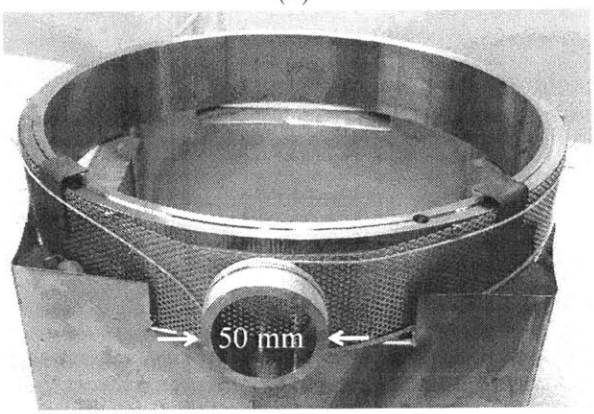

(b)

Figure 2-9: Two options for PCS location in each coil module. (a) PCS is placed concentrically around the main winding. (b) PCS is placed closely on the side of the main winding.

shown in Figure 2-9. Figure 2-9a shows Option 1 in which the PCS is concentrically wound around the main winding. Figure 2-9b shows Option 2 where the PCS is placed closely on the outer side of the main winding. Both winding options require non-inductive winding. Namely, the two ends from the main winding have to be co-wound and the currents flow in the opposite direction in each wire.

Both winding options were experimented with, and in both options the PCS worked well. The advantage of Option 1 is that the PCS generates concentric error field in the bore, even when it is not perfectly non-inductively wound. However, in Option 1, the PCS has a large surface area. When the PCS is open and above

40 K, the PCS, with a large surface area, can emanate a significant amount of heat to the surrounding cryogen. In Option 2, by non-inductive winding, we can essentially remove the error field generated by the PCS. Even if there is some uncompensated error field, it can be shimmed later. If the heat from the PCS is large, the PCS may not be opened and closed promptly, and it may require a huge amount of heating power to maintain resistive at >40 K. This heating problem can become worse than the error field. By weighing the disadvantage against the advantage, Option 2 was eventually employed to wind the PCS's.

2.6.2 Thermal Insulation

When open, a PCS has to be maintained resistive at >40 K while the environmental temperature is 10-15 K. The PCS's then have to be insulated very well so that the PCS's heating to the cryogenic environment is minimal. In order to design the insulation, a model of PCS is developed and heat transfer is estimated. A schematic drawing of a PCS cross-section is shown in Figure 2-10.

Heat transfer between the PCS and the environment includes three parts: conduction, convection and radiation. Because Styrofoam pieces surround the PCS, there is no direct convection between the PCS and the cryogen. Radiation heat input can be estimated with the following equation:

$$Q = A\epsilon\sigma(T_{\text{out}}^4 - T_{\text{in}}^4) \approx 1 \text{ mW} \tag{2.1}$$

Conduction heat input can be estimated with the following equations:

$$Q = A\frac{k_{\text{foam}}(T_{\text{in}} - T_{\text{out}})}{d} \approx 0.1 \text{ W} \tag{2.2a}$$

$$Q = A\frac{k_{\text{s.s.}}(T_{\text{in}} - T_{\text{out}})}{d} \approx 0.1 \text{ W} \tag{2.2b}$$

In these equations, A is the total surface area—top, bottom and side—of the PCS, $T_{\text{in}} = 40$ K is the temperature inside the PCS, $T_{\text{out}} = 10$ K is the environment temperature. The average thermal conductivity of styrofoam at 10-40 K is $k_{\text{foam}} =$

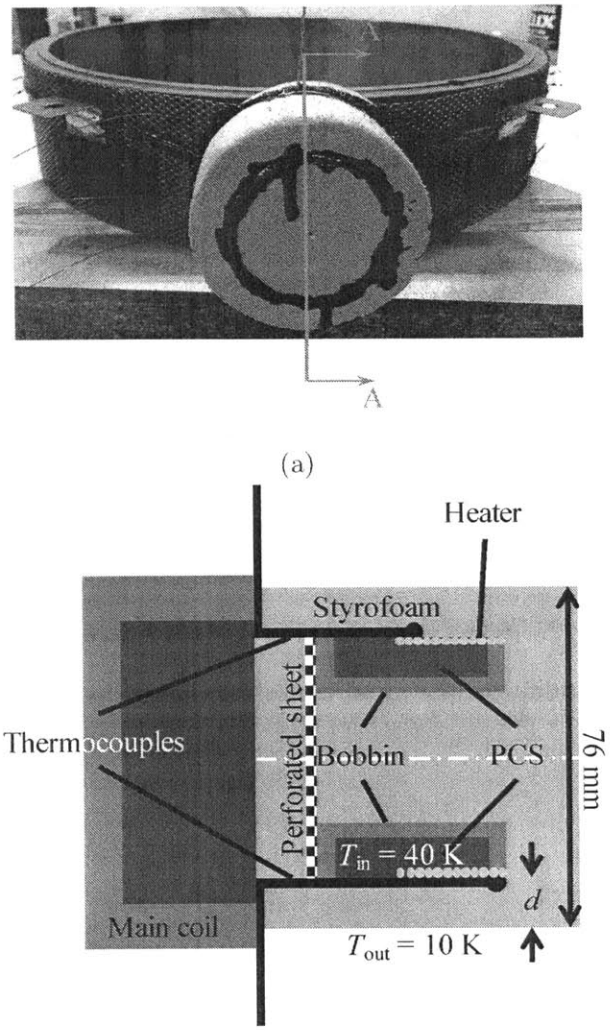

Figure 2-10: Schematic drawing of PCS section A-A. Pink styrofoam insulates PCS at >40 K from the cryogen at ~10 K.

0.01 W/mK [1], and the average thermal conductivity of stainless steel at 10-40 K is $k_{s.s.} = 3$ W/mK [1]. In real application, insulation cannot be perfect, so actual heat leak may be greater than the estimate above. In this magnet, a 12 mm layer of Styrofoam should be suffice to insulate the PCS's and keep the required heating power to <1 W.

2.6.3 Thermal Diffusion

A heater made of resistive wire is usually used to heat up a PCS. To make sure the PCS can be heated uniformly and opened promptly, I checked the time for heat to diffuse from the heater to the center of out monofilamant MgB_2 wire. The heater was wound closely and epoxied to the outermost layer of the MgB_2 wire in the PCS. Thus, we may assume that the diffusion distance from the heater to the center of its neighboring MgB_2 wire is the wire radius, $R = 0.5$ mm. The average diffusivity of the metal layers, in the temperature range 10-44 K, may be estimated with copper properties as $\alpha = 0.01$ m^2/s. Therefore, the diffusion time constant is

$$\tau \approx \frac{R^2}{\alpha} = \frac{0.0005^2}{0.01} = 2.5 \times 10^{-5} \text{ s} \tag{2.3}$$

There may be gaps between the heater and the MgB_2 wire that are filled with epoxy. A gap would slow down the thermal diffusion process. Assume a gap width is the same as the MgB_2 wire radius $d = 0.5$ mm. The average diffusivity of epoxy, in the temperature range 10-44 K, is $\alpha \approx 2 \times 10^{-6}$ m^2/s. The time for heat to penetrate an epoxy-filled gap can be estimated as

$$\tau \approx \frac{d^2}{\alpha} = \frac{0.0005^2}{2 \times 10^{-6}} \approx 0.1 \text{ s} \tag{2.4}$$

This diffusion time of 0.1 s, though much longer than that in a MgB_2 wire, is still much shorter than the required time to activate a PCS (Section 2.7). It means that the thermal diffusion in the PCS will not adversely affect the PCS opening time.

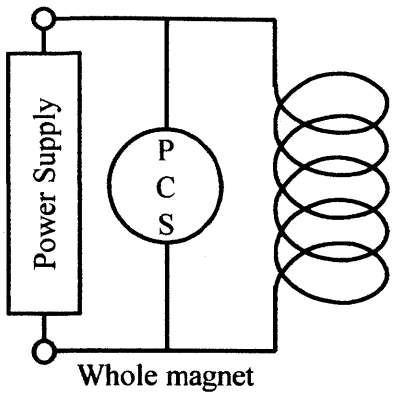

Figure 2-11: Circuit diagram of a magnet-PCS unit consolidated from the 8 coil modules.

2.6.4 Wire Length

The wire length in a PCS should be determined by the required normal-state resistance. The PCS resistance should be large enough to make its normal-state bypass current less than 1/10 of the coil current [1]. In order to simplify calculation, I consolidate the 8 coil modules into a single magnet-PCS unit. An equivalent circuit diagram is drawn in Figure 2-11.

The magnet inductance L is 0.74 H. If the magnet is charged or discharged at a ramping rate of 0.1 A/s, the total voltage V across the magnet is

$$V = L\frac{dI}{dt} = 74 \text{ mV} \tag{2.5}$$

To limit the PCS bypass current to <1 A, the PCS resistance needs to be

$$R_{\text{PCS}} \geqslant \frac{V}{1 \text{ A}} = 74 \text{ m}\Omega \tag{2.6}$$

When the PCS is at >40 K, the copper layer in the wire mainly conducts current. With copper resistivity of $\rho_{\text{Cu}} = 0.28$ nΩ·m at 40 K and its cross-sectional area of $A_{\text{Cu}} = 1.9 \times 10^{-7}$ m^2, the wire length corresponding to 74 mΩ resistance is

$$l_{\text{PCS}} = \frac{R_{\text{PCS}} A_{\text{Cu}}}{\rho_{\text{Cu}}} = 50 \text{ m} \tag{2.7}$$

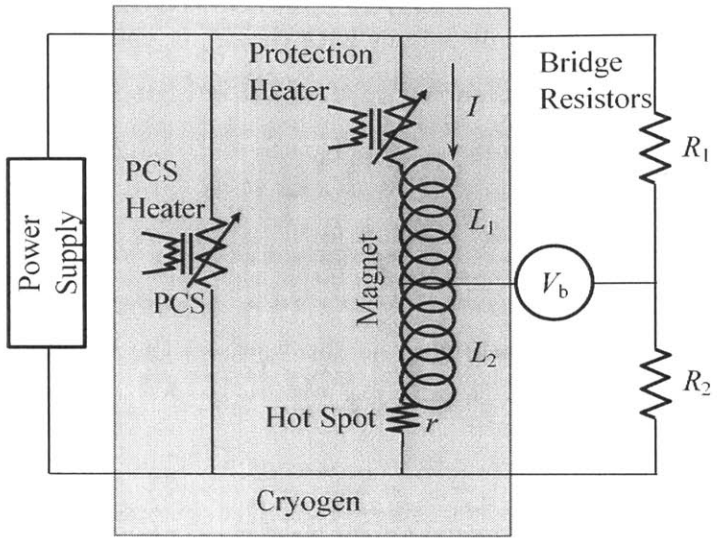

Figure 2-12: A circuit diagram shows the mechanism of the detect-and-activate-the-heater technique.

The result indicates that a total of 50 m MgB_2 wire, or ~6 m in each PCS, is required for this magnet.

2.7 Protection

2.7.1 Detect-and-Activate-the-Heater Technique

Because the magnet is operated in persistent mode, it has to be actively protected. A detect-and-activate-the-heater technique was employed to protect this magnet. A circuit diagram shown in Figure 2-12 illustrates the mechanism of this active protection technique. The basic concept of this protection technique is as follows [1]: when a quench is initiated and detected, most magnet energy will be released, by means of an activated heater embedded or right next to a designated winding volume. This actively heated volume is large enough from being overheated.

When a superconducting magnet is operated in persistent mode, it is impossible to detect quench initiation from the magnet terminals. In persistent mode, the terminals of the magnet are short-circuited by the PCS, and the voltage across the terminals always remains 0. In order to detect a quench, a voltage tap is attached to the center

of the magnet, and a bridge circuit is built with the center voltage tap together with the two terminal voltage taps, as shown on the right in Figure 2-12 [35].

The resistors R_1 and R_2 should be properly chosen to balance the bridge:

$$\frac{L_1}{R_1} = \frac{L_2}{R_2} \tag{2.8}$$

When a quench generates a resistance r in the winding, the bridge becomes unbalanced, and the detected bridge voltage V_b is

$$V_b = \frac{R_1}{R_1 + R_2} r \cdot I \tag{2.9}$$

where I is the operating current.

Once a nonzero bridge voltage is detected, the voltage is sent to an insulated-gate bipolar transistor (IGBT), which activates the designated energy absorber immediately. As remarked above, the energy absorber is a part of the winding, which should have a sufficient volume to absorb the entire magnetic energy while maintaining its own temperature below a safe value, e.g., 100 K. Because the energy absorber is a part of the winding, it is superconducting during normal operation. To activate it, the IGBT sends a current in the protection heater to heat it up. Once the absorber is heated above its critical temperature, it becomes resistive and gradually absorbs the magnetic energy through Joule heating.

As a part of the winding, an energy absorber has to be cooled the same as the rest of the magnet. Therefore, to overcome the cooling power to the absorber, the protection heater is usually cumbersome and requires significant heating power.

2.7.2 PCS as Energy Absorber

In this magnet, I did not deploy separate energy absorbers. Instead, as a major innovation of the magnet, I combined the switching and energy-absorbing functions into a single unit—a modified PCS. A circuit diagram of this design concept is shown in Figure 2-13. To charge or discharge the magnet, we open all 8 PCS's as usual.

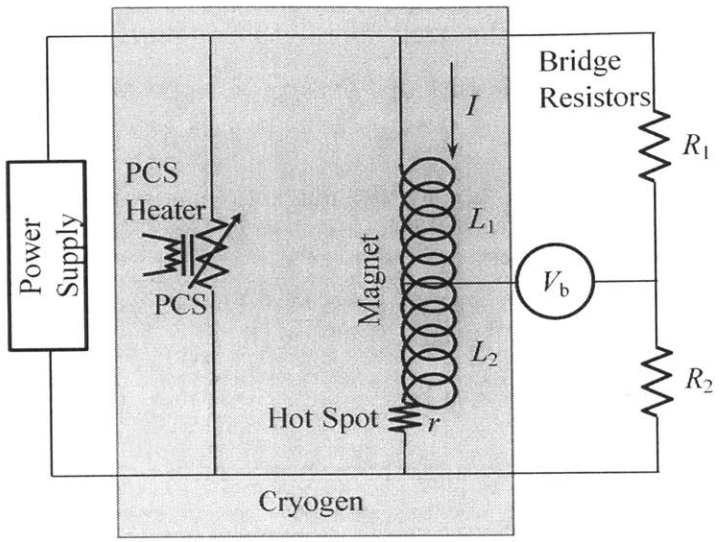

Figure 2-13: Circuit diagram of a detect-and-activate-the-heater protection concept with PCS as the energy absorber.

When a quench is detected in the magnet, the IGBT sends a current in the PCS heaters to heat up the PCS's. Because the total PCS resistance is much larger than the resistance of an initial quench spot, most of the magnetic energy will be dumped into the PCS's. In this design, we do not need separate energy absorbers or cumbersome protection heaters: each PCS has its own heater for both switching and protection. In addition, each PCS is thermally insulated from the environment, enabling each PCS to be heated more easily and quickly than heating up a section of each coil module, resulting in an efficient active protection procedure.

2.7.3 Energy Criterion

In order to absorb the entire magnetic energy safely, the total volume of the PCS's has to be large enough. It is generally considered safe to keep the temperature of a superconducting wire <200 K [1].

The total magnetic energy of the magnet at its peak current of 100 A is

$$E = \frac{1}{2}LI^2 = 3.7\text{kJ} \tag{2.10}$$

The properties of materials in the MgB_2 wire can be approximated with those of respective copper properties. The enthalpy density of copper from 40 K—the PCS is heated to normal state and starts to absorb energy—to 200 K is $\Delta h = 3 \times 10^5$ kJ/m^3 [1]. The PCS volume required to absorb the magnetic energy is

$$V = \frac{E}{\Delta h} = 1.2 \times 10^{-5} \text{ m}^3 \tag{2.11}$$

The corresponding MgB_2 wire length is

$$l_{\text{PCS}} = \frac{V}{A_{\text{cd}}} = 22 \text{ m} \tag{2.12}$$

where A_{cd} is the cross-sectional area of the MgB_2 wire. This length of 22 m is shorter than the required length for switching. So, it is reasonable to use the PCS's to absorb energy and protect the magnet.

2.7.4 Time Criterion

The energy absorber needs to soak up the magnetic energy not only safely, but also promptly. The magnet-PCS circuit is equivalent to an L-R circuit. The resistance of the PCS, when activated as the absorber, should be large enough to provide a short time constant, preventing the initial quench spot, i.e., a hot spot, from burning out.

In order to estimate the required PCS resistance, I estimated the time for an initial quench spot to develop and burn out. Assuming that a hot spot is heated adiabatically by a constant current, the thermal equation is

$$A_{\text{cd}} C_{\text{cd}}(T) \frac{dT}{dt} = \frac{\rho_{\text{m}}}{A_{\text{m}}} I^2(t) \tag{2.13}$$

In this equation, C_{cd} is the average unit volume specific heat of the MgB_2 wire, ρ_{m} is the electric resistivity of the matrix material—copper in the MgB_2 wire—and A_{m} is the cross-sectional area of the copper layer. Rearrange this equation and integrate

over time, I obtained

$$\int_{T_i}^{T_f} \frac{C_{\mathrm{m}}(T)}{\rho_{\mathrm{m}}(T)}\, dT = \left(\frac{A_{\mathrm{m}}}{A_{\mathrm{cd}}}\right) J_{\mathrm{m}}^2 \tau \tag{2.14}$$

Here, I approximated the average specific heat C_{cd} with the specific heat of copper C_{m}. The current density in the matrix is $J_{\mathrm{m}} = I/A_{\mathrm{m}}$. The time constant τ indicates how long it takes for the hot spot to be heated from its initial temperature T_i to a final temperature T_f under a constant current I. We can then define the integral as

$$Z(T_f, T_i) \equiv \int_{T_i}^{T_f} \frac{C_{\mathrm{m}}(T)}{\rho_{\mathrm{m}}(T)}\, dT \tag{2.15}$$

Iwasa introduced the concept of Z-function in his textbook "Case Studies in Superconducting Magnets—Design and Operational Issues," both the 1st Edition (1994) and the 2nd Edition (2009) [1]. Z-function is defined such that it is determined only by the specific heat and electric resistivity—both are material properties. Therefore, Z-function is also a temperature-dependent material property. Z-functions of selected common matrix metals are plotted vs. temperature in Figure 2-14 [1].

In Figure 2-14, the vertical axis shows Z-function from 0 K to a specific temperature T, e.g., $Z(T, 0)$. In order to find Z-function between any temperature interval (T_f, T_i), I simply need to find both $Z(T_f, 0)$ and $Z(T_i, 0)$, and their difference $Z(T_f, 0) - Z(T_i, 0) = Z(T_f, T_i)$. This can be demonstrated:

$$Z(T_f, T_i) = \int_{T_i}^{T_f} \frac{C_{\mathrm{m}}(T)}{\rho_{\mathrm{m}}(T)}\, dT = \int_{0}^{T_f} \frac{C_{\mathrm{m}}(T)}{\rho_{\mathrm{m}}(T)}\, dT - \int_{0}^{T_i} \frac{C_{\mathrm{m}}(T)}{\rho_{\mathrm{m}}(T)}\, dT = Z(T_f, 0) - Z(T_i, 0) \tag{2.16}$$

The above calculation assumed a constant current. In this magnet, while the energy absorber is activated, the current will discharge exponentially. Under this discharging current, a thermal balance equation is similar to Equation 2.14:

$$Z(T_f, T_i) = \left(\frac{A_{\mathrm{m}}}{A_{\mathrm{cd}}}\right) J_{\mathrm{m}}^2 \left(\frac{L}{2R_{\mathrm{PCS}}}\right) \tag{2.17}$$

Here, instead of τ in Equation 2.14, an equivalent time constant $L/2R_{\mathrm{PCS}}$ appears. When the energy absorber is activated, the current through a hot spot decreases

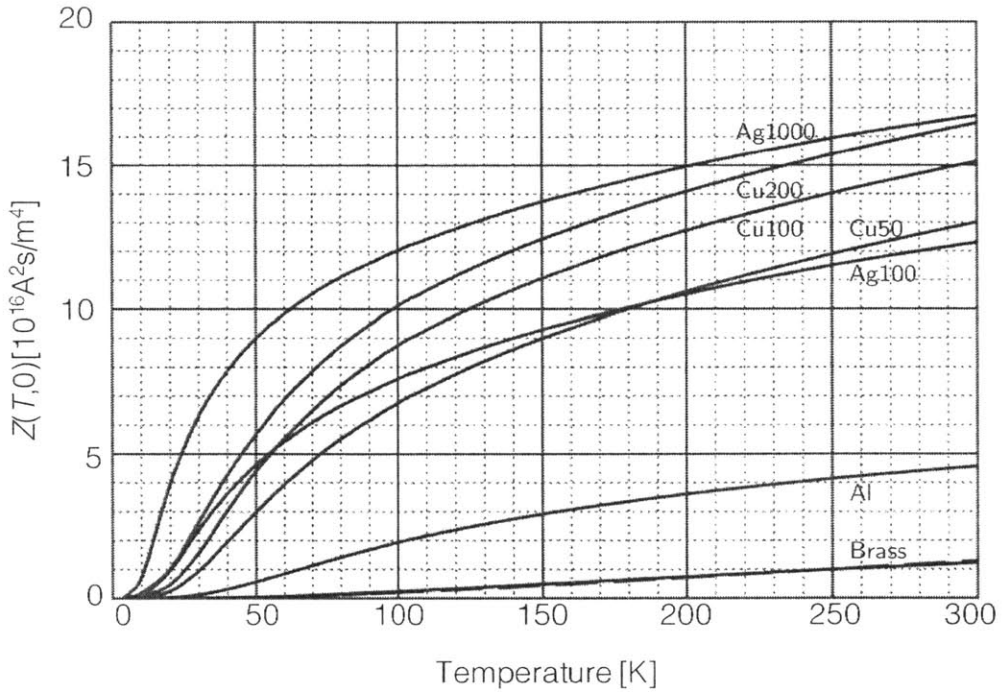

Figure 2-14: Z-functions of selected common matrix metals plotted vs. temperature [1].

exponentially with a time constant $L/R_{\rm PCS}$. While the current decreases from the operating current I to 0, the hot spot temperature rises from the operating temperature T_i to a final temperature T_f.

The operating temperature of this magnet is $T_i = 10 - 15$ K, and the relatively safe maximum temperature in a superconducting wire is $T_f = 200$ K. From these two temperatures, I determined, from Figure 2-14, $Z(200\text{K}, 10\text{K}) = 15 \times 10^{16}$ A^{2}s/m^4. Substituting the cross-sectional areas $A_{\rm m} = 0.19$ mm^2 and $A_{\rm cd} = 0.55$ mm^2 into Equation 2.17, I obtained the desired PCS resistance

$$R_{\rm PCS} = \left(\frac{A_{\rm m}}{A_{\rm cd}}\right) J_{\rm m}^2 \left[\frac{L}{2Z(200\text{K}, 10\text{K})}\right] = 230 \text{ m}\Omega \tag{2.18}$$

The wire length corresponding to this resistance is

$$l_{\rm PCS} = \frac{R_{\rm PCS} A_{\rm Cu}}{\rho_{\rm Cu}} = 156 \text{ m} \tag{2.19}$$

This result indicates that a total of 156 m MgB_2 wire in the PCS could discharge the magnet fast enough to prevent a hot spot from burning out.

2.7.5 Second Energy Criterion

Three criteria of designing the PCS was discussed in Section 2.6.4, 2.7.3, and 2.7.4. Switching, energy-absorbing, and discharge-time criteria require the wire in PCS to be longer than, respectively, 50 m, 22 m, and 156 m. The three criteria are the sufficient conditions for PCS design. All three criteria give lower bounds of the wire length in PCS. Therefore, for this 8-coil magnet, it seems safer to use a total wire length >156 m for 8 PCS's.

All the energy to open the PCS's will be dissipated in the cryogenic environment, however, which eventually needs to be taken away by a cryocooler or liquid helium vapor. With either cooling source, large energy dissipation should be avoided. It means that the heat to open the PCS's should be minimized. For each PCS this energy is simply the product of the PCS volume and its enthalpy density. The PCS is

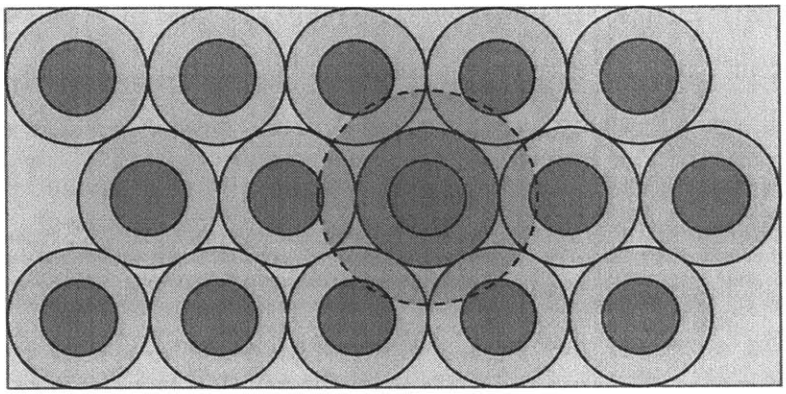

Figure 2-15: Heat at an initial quench spot conducts to surrounding solid nitrogen and neighboring wire.

wound with MgB_2 wire, which has a fixed enthalpy density. The only option is then to minimize the PCS volume, namely, the length of MgB_2 wire in the PCS.

A total length of 156 m in 8 PCS's, determined by the discharge-time criterion, is sufficient. Considering that all 8 main coils contain over 2,000 m of the wire and are not really under adiabatic condition, 156 m can be shortened.

This magnet was operated in a volume of solid nitrogen that filled the void between MgB_2 wires, as shown in Figure 2-15. With the presence of solid nitrogen, Joule heat at an initial quench spot would conduct to the surrounding solid nitrogen and neighboring wire. The thermal diffusivity of solid nitrogen is $\mathcal{D} = 0.58 \times 10^{-6}$ m^2/s at 20 K and 70×10^{-6} m^2/s at 10 K [1]. The thermal diffusivity of copper is 0.17 m^2/s at 10 K and 0.029 m^2/s at 20 K [1]. At 20 K, in a period equal to the magnet discharge time constant $\tau = L/R_{\rm PCS} \approx 3$ s, the Joule heat could diffuse to a spherical volume of radius

$$L = \sqrt{\mathcal{D}\tau} = 1.3 \text{ mm} \tag{2.20}$$

The materials in this spherical volume would absorb some thermal energy and help keep the quench spot temperature low. Therefore, the discharge time constant can be longer than that estimated in Section 2.7.4.

A total length of 80 m of MgB_2 wire was wound in the PCS's, namely, 10 m wire in the PCS of each coil module. The corresponding PCS resistance is 118 mΩ, resulting in a discharge time constant $\tau = L/R_{\rm PCS} \approx 6$ s. In this period, A spherical volume

of radius

$$L = \sqrt{\mathcal{D}\tau} = 1.8 \text{ mm} \tag{2.21}$$

would be heated. Considering an 8% volumetric shrinkage of solid nitrogen from 63 K to 10 K, the solid nitrogen volume in the heated sphere is still >10 times larger than the volume of the initial quench spot in the wire, which would absorb more energy than the quench spot itself and keep the spot temperature below a safe value.

The total volume of this 80-m wire in the PCS is

$$V = \frac{1}{4}\pi D_{\text{PCS}}^2 l_{\text{PCS}} = 4.4 \times 10^{-5} \text{ m}^3 \tag{2.22}$$

The PCS has to be heated up from ~10 K to >40 K to become open. The enthalpy density of the wire from 10-40 K is

$$\Delta h = 6 \times 10^3 \text{ kJ/m}^3 \tag{2.23}$$

The total thermal energy to open this PCS is then

$$E = \Delta h V = 264 \text{ J} \tag{2.24}$$

In the experiment, a two-stage GM cryocooler was deployed to cool the cold mass. The 2nd stage cold head provides 8 W cooling power at 10 K and 15 W at 18 K. If the 2nd stage cold head spares 6 W cooling power to the PCS's, this thermal energy of 264 J can be conducted away in about 40 s.

2.8 Multi-Coil Consideration

In Sections 2.6.4 and 2.7, I derived all the parameters based on a consolidated magnet-PCS unit. However, the magnet consists of 8 coil modules, each having its own PCS and running in persistent-mode independently. The mutual inductances between each pair of coils will change the design parameters.

The differential equations governing the currents in the coils are:

$$M_{11}\frac{dI_1}{dt} + M_{12}\frac{dI_2}{dt} + M_{13}\frac{dI_3}{dt} + \cdots + M_{18}\frac{dI_8}{dt} + I_{\mathrm{PCS1}}R_{\mathrm{PCS1}} = 0 \tag{2.25a}$$

$$M_{21}\frac{dI_2}{dt} + M_{22}\frac{dI_2}{dt} + M_{23}\frac{dI_3}{dt} + \cdots + M_{28}\frac{dI_8}{dt} + I_{\mathrm{PCS2}}R_{\mathrm{PCS2}} = 0 \tag{2.25b}$$

$$M_{31}\frac{dI_1}{dt} + M_{32}\frac{dI_2}{dt} + M_{33}\frac{dI_3}{dt} + \cdots + M_{38}\frac{dI_8}{dt} + I_{\mathrm{PCS3}}R_{\mathrm{PCS3}} = 0 \tag{2.25c}$$

$$\vdots$$

$$M_{81}\frac{dI_1}{dt} + M_{82}\frac{dI_2}{dt} + M_{83}\frac{dI_3}{dt} + \cdots + M_{88}\frac{dI_8}{dt} + I_{\mathrm{PCS8}}R_{\mathrm{PCS8}} = 0 \tag{2.25d}$$

In the above equations, M_{ii} is the self inductance of the i^{th} coil, M_{ij} is the mutual inductance between the i^{th} and the j^{th} coil, I_i is the current in the i^{th} coil, $I_{\mathrm{PCS}i}$ is the current in the PCS of the i^{th} coil, and $R_{\mathrm{PCS}i}$ is the PCS resistance of the i^{th} coil. The values of self and mutual inductances are summarized in Appendix A.

In order to keep the current and ramping rate the same in each coil during charging and discharging process, the PCS resistances need to satisfy

$$R_{\mathrm{PCS1}} : R_{\mathrm{PCS2}} : R_{\mathrm{PCS3}} : \cdots : R_{\mathrm{PCS8}} = \sum_{n=1}^{8} M_{1n} : \sum_{n=1}^{8} M_{2n} : \sum_{n=1}^{8} M_{3n} : \cdots : \sum_{n=1}^{8} M_{8n} \tag{2.26}$$

In this magnet, I wound the 8 PCS's equally so that all PCS bobbins had the same dimensions, simplifying the winding process. Thus, the PCS resistances were the same and did not satisfy the ideal ratio in Equation 2.26. During charging and discharging process, therefore, the currents in coils were slightly different. However, as long as all PCS's were open for long enough, the currents in all coils eventually became constant and equal to the supplied current.

In the event of active protection, the self and mutual inductances would lead to different ramping rates in different coils, which in turn would result in different final PCS temperatures. Since 10-m wire in each PCS is much longer than the length of ~3 m determined by absorbing-energy criterion, all PCS's should remain <200 K.

Chapter 3

Manufacturing

The magnet consists of 8 coil modules. Each module was wound-and-reacted in the same way, and then assembled into the final magnet assembly.

3.1 Winding

3.1.1 Coil Mandrel

Because the wind-and-react procedure was employed, the coil mandrels needed to undergo heat treatment together with the wires. The material for coil mandrel must have a melting point greater than the heat-treatment temperature, and its mechanical properties after heat treatment should be unchanged. Obviously, no plastic could withstand heat treatment at 700°C. Among common structural metals, stainless steel is the best option because of its high strength, high melting point and low cost. For this magnet, 304 stainless steel, a non-magnetic and corrosion-resistive steel, was chosen to make the coil mandrels.

A coil mandrel was made from a stainless steel cylinder. A 3-D model of a machined mandrel is shown in Figure 3-1. A groove was cut in the cylinder for the winding. On the upper side of the groove, a slot was cut for the lead-in and lead-out MgB_2 wires. A few holes were drilled and tapped on both upper and lower edges of the mandrel to later secure the PCS. A window was cut on the upper side of the

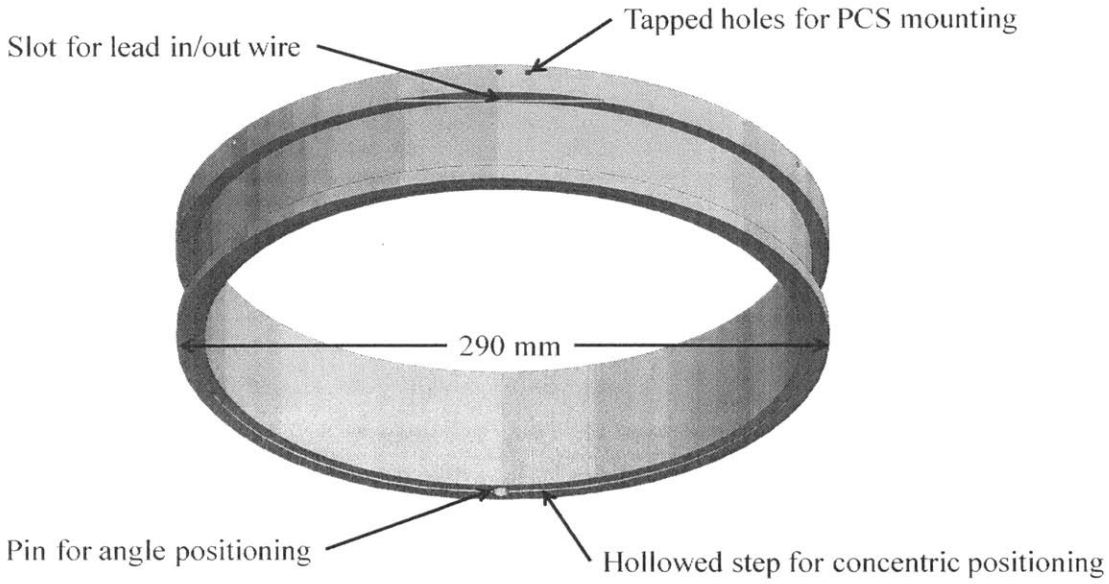

Figure 3-1: 3-D model of coil mandrel.

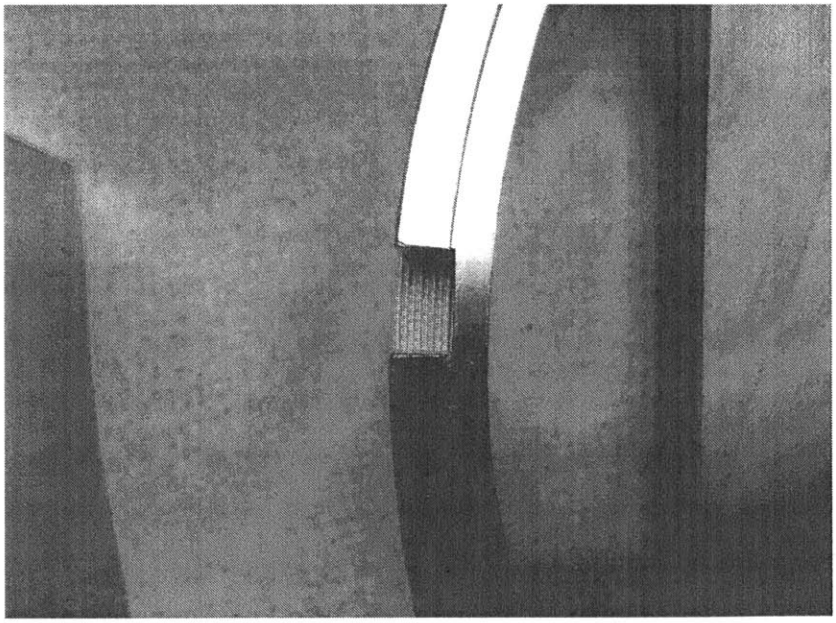

Figure 3-2: Window on the upper side of the mandrel for center voltage tap.

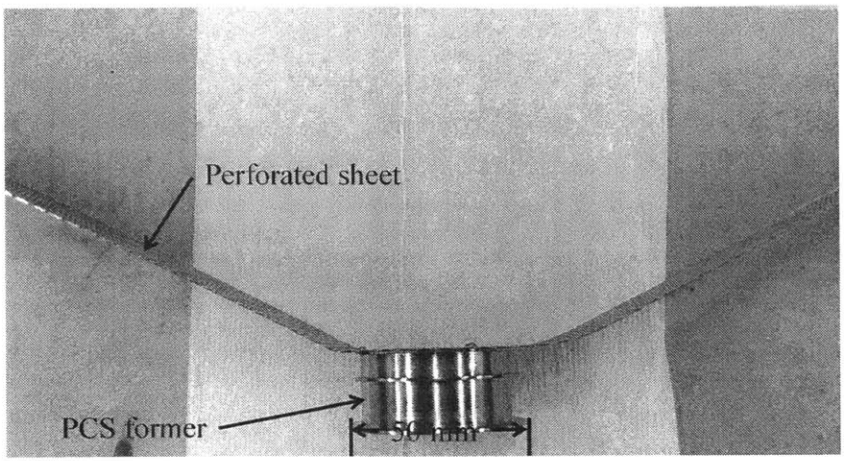

Figure 3-3: PCS former attached to perforated stainless steel sheet.

mandrel, as shown in Figure 3-2, for the center voltage tap to attach to the middle of the winding.

Because 8 coil modules were to be assembled to form the magnet, it was very important to position the coils accurately. A protruding step was machined on the upper side of the mandrel and a hollowed step was machined on the lower side. When being assembled, the protruding step of the lower module fitted into the hollowed step of the upper module, so that the neighboring coils were concentrically assembled. The neighboring coils were mortised so as to secure their relative orientation.

3.1.2 PCS Former

The PCS's were placed on the side of the coils. In order to secure the PCS former, it was bolted to a perforated stainless steel sheet that was in turn bolted on side of the coil mandrel, as shown in Figure 3-3. The perforated sheet was selected to secure the PCS former, because it provided a stable surface to secure other components of the module, i.e., leading wires, lugs and the joint. In addition, the small holes in the sheet were able to grasp epoxy, resulting in good epoxy quality.

A PCS former has a diameter of 50 mm and a height of 21 mm. The wall of a former is 0.7 mm thin, so that the former has little heat capacity, absorbing little thermal energy when the PCS opens. A PCS former was designed to have two winding

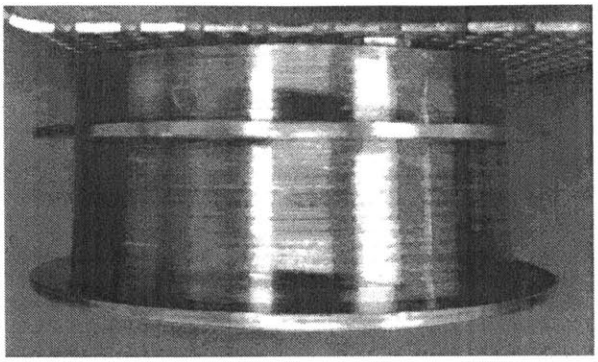

Figure 3-4: Gap between PCS former and perforated sheet to reduce conduction.

grooves. The main groove away from the perforated sheet holds 4 layers of wire and 12 turns in each layer. The groove close to the perforated sheet also holds 4 layers but 6 turns in each layer. The winding grooves were separate so that the PCS can be wound in the main groove neatly while the transition winding in the smaller groove can be slightly disordered.

In order to reduce conduction through the PCS-former-perforated-sheet path, a gap was left between the PCS former and the sheet. When a PCS former was bolted to the perforated sheet, a washer was placed on each screw between the former and the sheet to lift the former. This gap can effectively decrease conduction from the PCS to the environment, eventually reducing the required heating power. A picture of a gap between a PCS former and the perforated sheet is shown in Figure 3-4.

3.1.3 Winding Main Coil

Each main coil was wound onto a mandrel with a winding machine. A length of 10 m wire was left in the beginning for the PCS and joint. During winding, a snug tension was maintained in the wire to make sure the turns were tight. A picture of the winding machine is shown in Figure 3-5a.

After all turns were wound in the winding groove, the perforated sheet, with a PCS former bolted on it, was mounted on side of the mandrel. Another length of 10 m wire was left in the end, again for the PCS and joint, before the wire was cut. Figure 3-5b shows a wound coil with PCS former mounted.

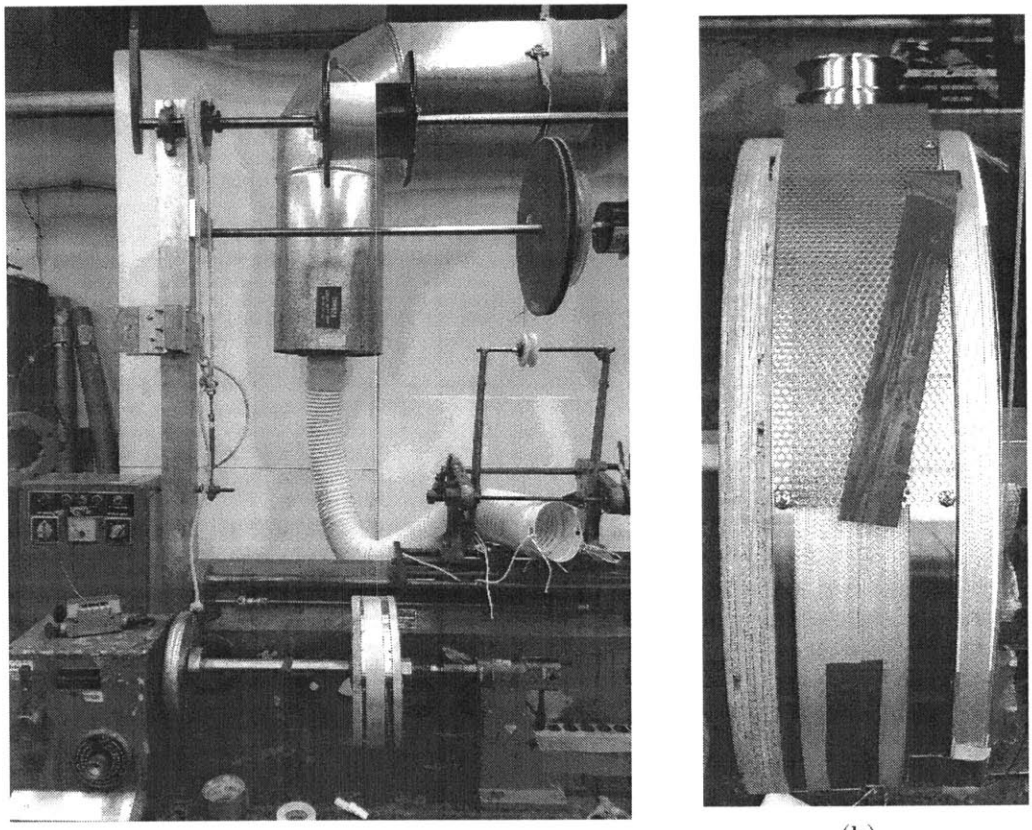

(a) (b)

Figure 3-5: (a) Coil being wound in the winding machine. (b) PCS former mounted to a wound coil.

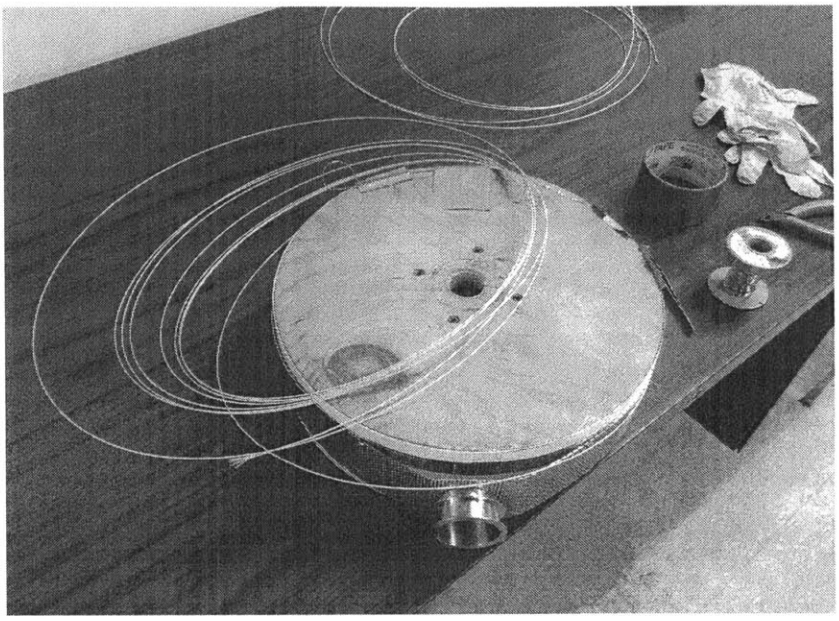

(a)

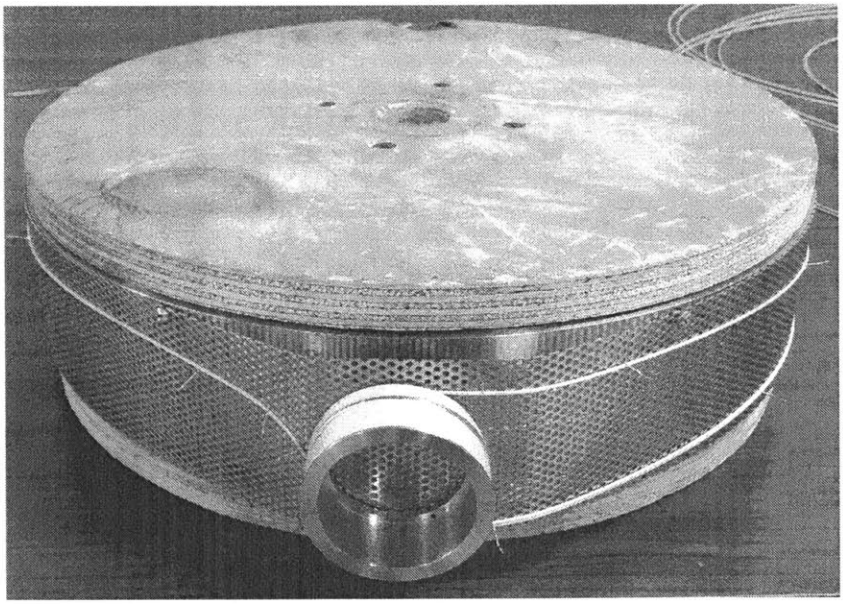

(b)

Figure 3-6: (a) Loose wires before winding PCS. (b) Wound PCS with transition wires tied to perforated sheet.

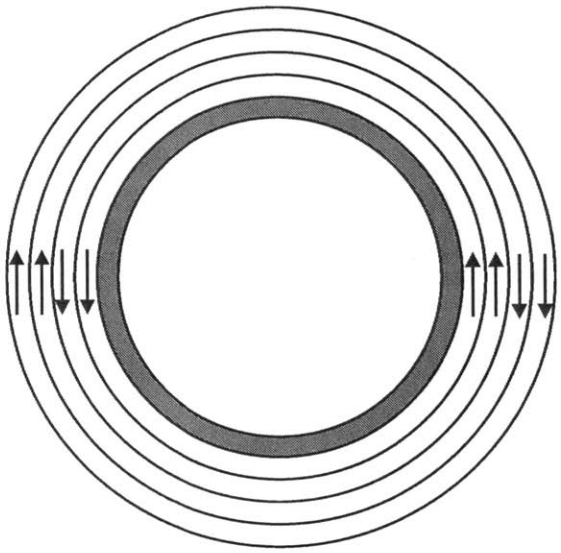

Figure 3-7: In the 4 layers of a PCS, the currents in the inner two layers and outer two layers were opposite.

3.1.4 Winding PCS

After the wire was wound onto the mandrel and cut from the original spool, the coil was removed from the winding machine. Since the PCS former was on the side and its axis was perpendicular to the axis of the main coil, it was hard to wind a PCS with a winding machine. The PCS's were wound manually. Figure 3-6 (a) and (b) show the PCS before and after being wound, respectively.

The PCS's were non-conductively wound. The two terminal wires from the main coil were wound in the PCS in their designated directions, so that the currents in the inner two layers and outer two layers were in opposite directions. This winding method, however, resulted in a tiny PCS inductance of $\sim 10^{-5}$ H. A schematic drawing of the current directions in the four layers of a PCS is shown in Figure 3-7. The wires coming out of the PCS were then spliced with a superconducting joint.

In order to secure loose wires during heat treatment and handling, the PCS lead-in and -out wires were tied to the perforated sheet with thin stainless steel wires, with little room to move. The fixture prevented too much wire movement that might damage the wire.

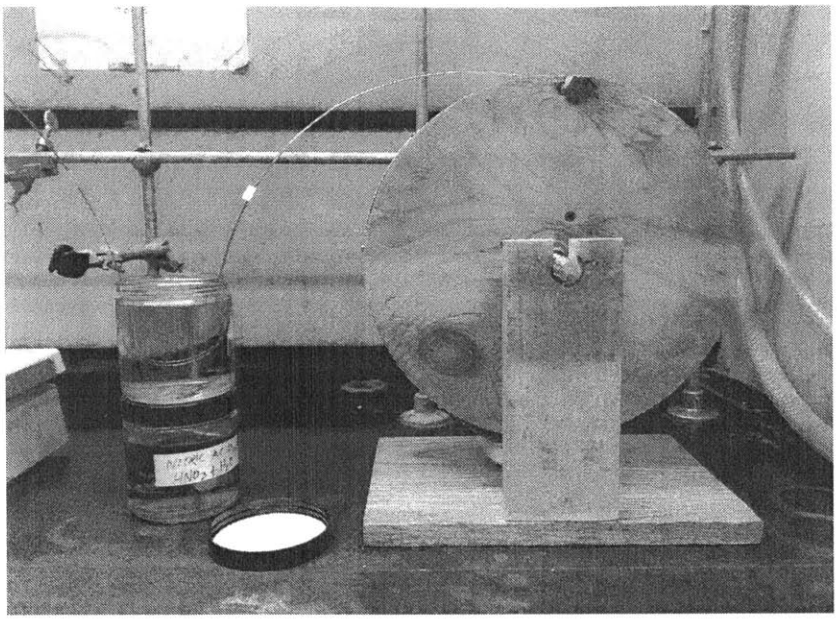

Figure 3-8: Wires, bent in "U" shape, being etched.

3.1.5 Making Joint

The coil joints were made basically in the same way as the short samples were made. First, 20-cm long S-glass insulation was removed from each wire tip. The wires were then bent in "U" shape 10 cm away from the tips. The "U" bottoms were then immersed in 5-cm-deep 15-20% nitric acid to etch Monel and copper layers. Nitric acid does not dissolve niobium. The tips of the wires were ~5-cm above nitric acid, so that the core of magnesium and boron powder remained intact. Figure 3-8 shows a photo of wires being etched.

After each terminal wire was etched, it was thoroughly cleaned with acetone. It was then sheared at a sharp acute angle to maximize the exposed surface area. The sheared tip was ~5 mm away from the etched base. A photo of a pair of sheared wire tips is shown in Figure 3-9.

A joint was then made in the same way as described in Section 2.4. The joint was dried in the air for a few hours before the sealing putty was fully cured. The spliced wires, with the joint, were then tied to the perforated sheet with thin stainless steel wires. Figure 3-10 shows a photo of a joint dried in the air.

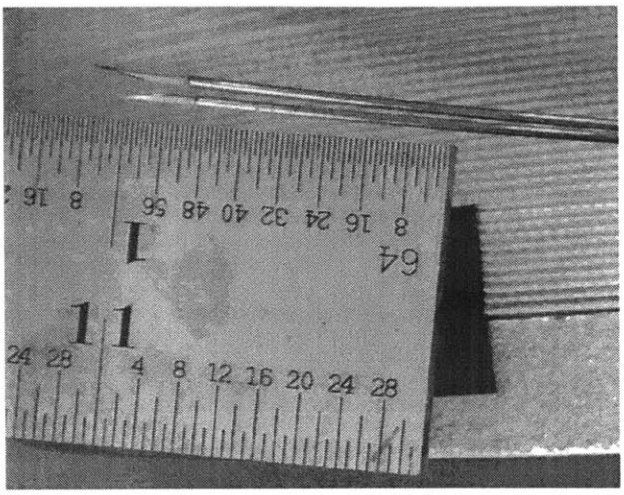

Figure 3-9: Wire tips sheared at a sharp acute angle, ~5 mm to the etched base.

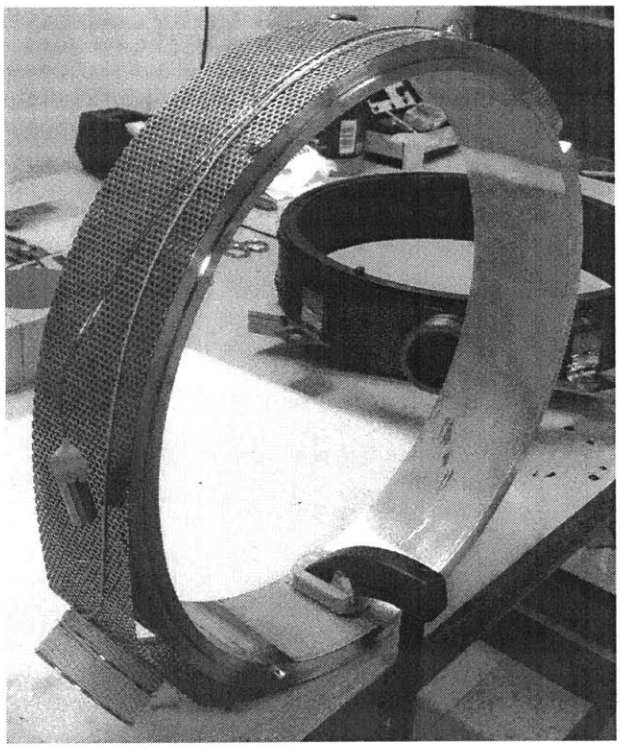

Figure 3-10: Sealed joint dried in the air.

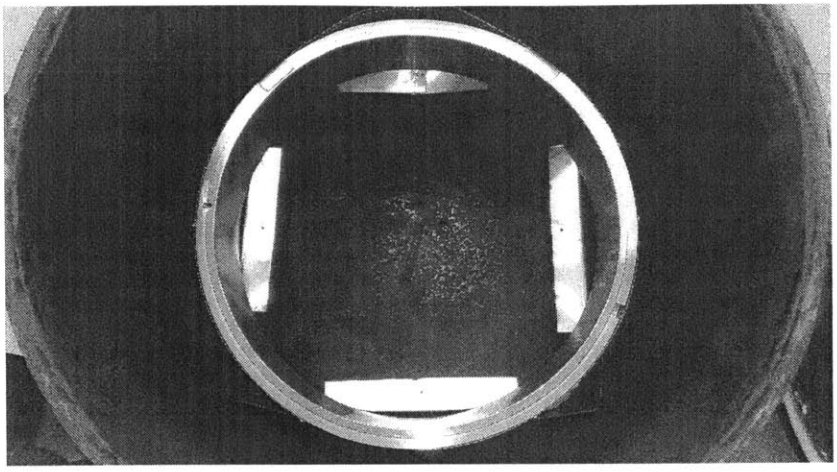

Figure 3-11: Coil, on a homemade rack, placed at the center of the stainless steel can.

3.2 Heat Treatment

After the main coil and the PCS were wound and the terminals spliced, the entire coil module was heat treated in a box furnace. MgB_2 wire needs to be heat-treated in argon environment, which cannot be sustained by the box furnace directly. A gas circulating and retaining system was developed to heat treat coil modules successfully.

3.2.1 Device

A stainless steel can was deployed to provided the required argon environment. Each coil module, when placed in the can, was supported by a homemade square stainless steel rack. The coil was not in direct contact with any surface of the can, so that the temperature in the coil was maintained relatively uniform during heat treatment. Two thin stainless steel tubes were connected to the can as the gas inlet and outlet.

3.2.2 Procedure

Once the gas system was set up in the box furnace, argon gas of 10 times of can volume was circulated to purge air completely from the system. The furnace was then turned on and kept at 100°Cfor 1 hour to dry the system.

At the end of the 1-hour baking stage, the furnace continued heating up. The

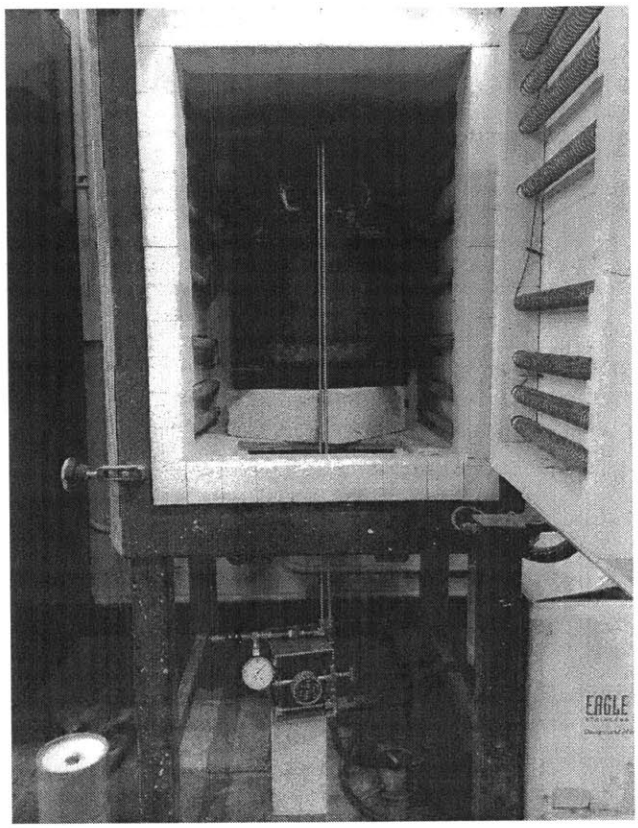

Figure 3-12: Stainless steel can placed at the center of the box furnace. Two stainless steel tubes connected to the can as the gas inlet and outlet.

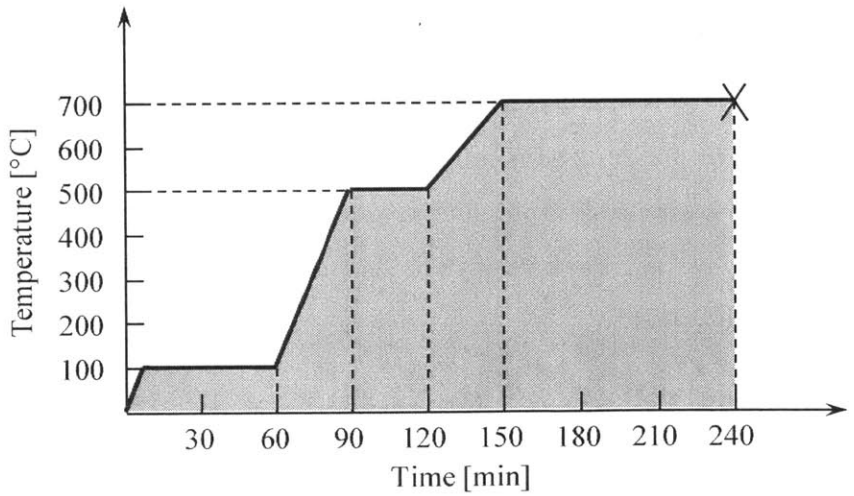

Figure 3-13: Heat treatment process for MgB_2 coil. Coil initially baked for 1 hour at 100°C, then heat-treated for 90 minutes at 700°C.

temperature rose from 100°Cto 500°Cin 30 min and kept at 500°Cfor 30 min. Then the temperature rose to 700°C, the designated temperature, in another 30 min and kept at 700°Cfor 90 min until heat treatment ended. When the heat treatment finished, the furnace was turned off, and the coil was cooled in the furnace naturally.

3.2.3 Key Issues

A few key issues was identified affecting coil performance, especially performance of the heat-treated superconducting joint.

(1) *Copper contamination.* Copper contaminates the reaction between magnesium and boron. Thus, copper should be kept away from the reaction site. However, our joint results have shown that copper does not affect the reaction if copper is >3 mm away from the site. In our joint, the sheared wire tips, where the reaction happened, were ~3 mm away from the etched edge of the copper layer in the wire. Every joint was proved to be superconducting.

(2) *Joint packing pressure.* As described in Section 2.4, a joint was packed with Mg+B powder to create a good contact between the exposed wire tips. The packing pressure, however, need not be extremely high. The pressure used by us to pack the powder was ~300 MPa, which was just enough to make powder compact.

(3) *Heat treatment pressure.* It is important to maintain a positive pressure during heat treatment to suppress vaporizing magnesium. A positive pressure, 35 kPa above atmospheric pressure, was kept with argon environment in our heat treatments, producing high-quality joints.

3.3 Finishing

After heat treatment, a few steps were taken to finish each coil.

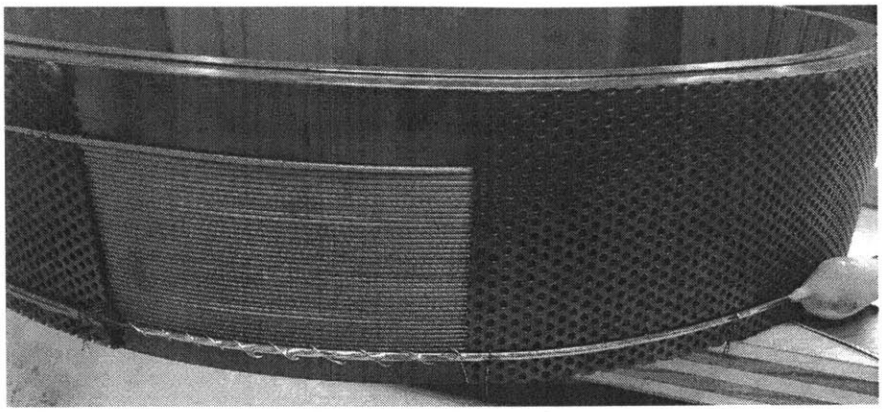

Figure 3-14: Section of wires soldered to protect the joint driven normal.

3.3.1 Soldering Terminal Wires

In order to protect the joint when it is driven normal, the two terminal wires were soldered together in a ~10-cm section right before the joint. In persistent mode, current in each coil module flows through the superconducting joint. In case the joint becomes normal, the soldered section will carry the entire current, saving the joint from permanent damage.

3.3.2 Insulating PCS

A PCS must be well insulated thermally to minimize heat loss to the environment. In this magnet, Styrofoam of 12-mm thick enclosed each PCS, and seams between Styrofoam pieces were sealed with Stycast epoxy. Before each PCS was sealed, two pieces of Manganin wire, each of 30 Ω, were wound and epoxied on the PCS winding, serving as the primary and secondary PCS heaters. Two thermocouples were implanted in each PCS as well to monitor the PCS temperature.

3.3.3 Soldering Copper Lugs

Two thin copper strips were soldered to each coil as the lugs of the coil. Adjacent coils were connected with copper jumpers bolted to the lugs. In each coil module, the copper lugs were soldered on two sides of the PCS, as depict by the schematic

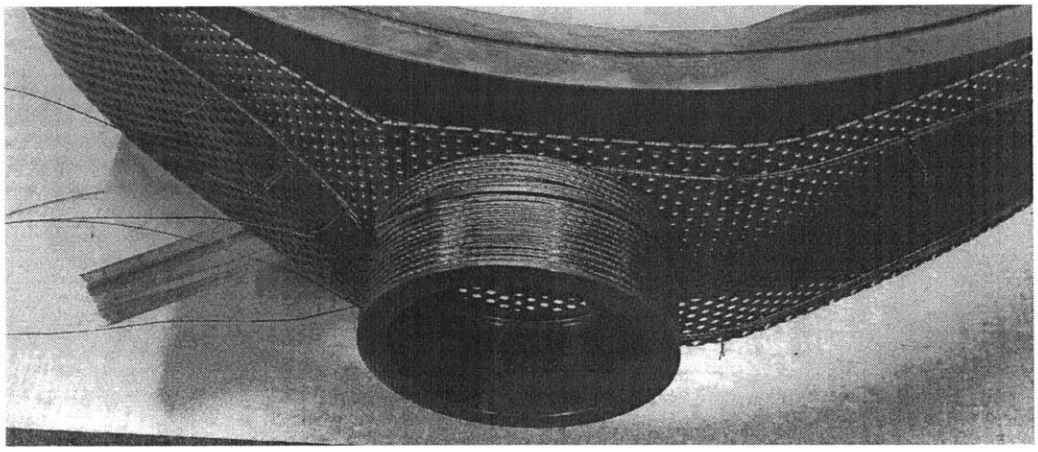

Figure 3-15: Two pieces of Manganin wire, each of 30 Ω, wound on a PCS as its heaters.

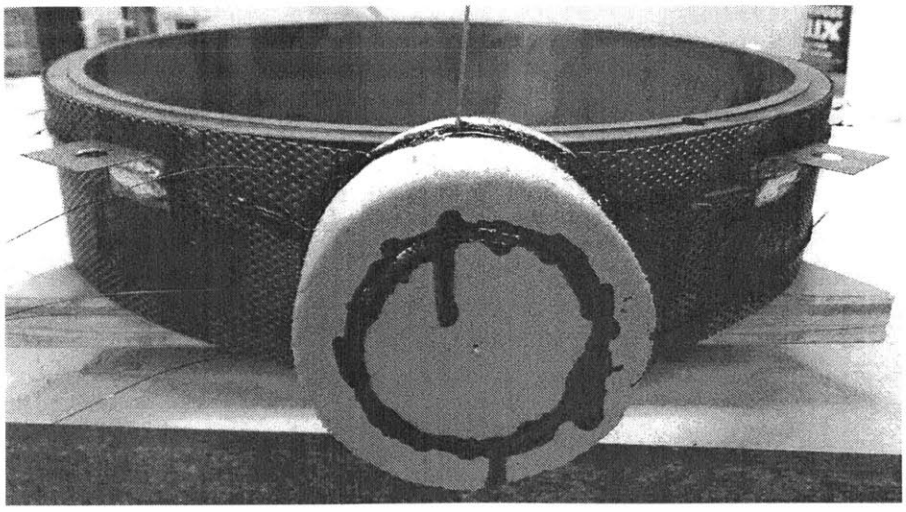

Figure 3-16: PCS enclosed by Styrofoam. On its sides, two copper lugs soldered to MgB_2 wire.

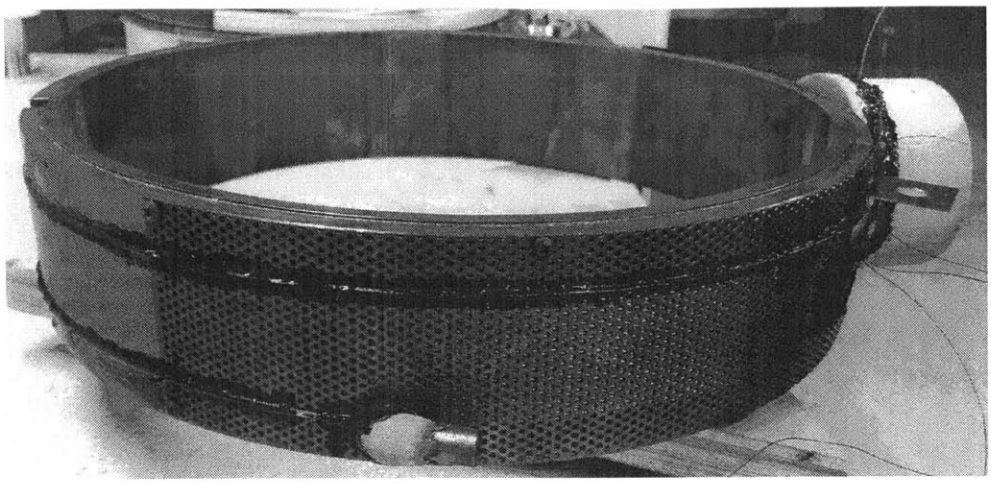

Figure 3-17: Joint and floating sections of wire epoxied to the perforated sheet for mechanical integrity.

drawing in Figure 2-7. As connected in this way, the current flows in the PCS and the joint when the PCS close (superconducting), and the current flows in the main coil when the PCS open (resistive).

Proper width and thickness were chosen for the copper strips to carry 100 A current. The copper strips had a width of 25 mm and a thickness of 0.5 mm, and a length of 10 mm from the jumper side to the MgB_2 wire side. With resistivity of 0.2 nΩ·m at 20 K [1], the total resistance of a copper lug is

$$R = \rho \frac{L}{A} = 1.6 \times 10^{-7}\ \Omega \tag{3.1}$$

When carrying 100 A current, a copper lug generated Joule heating of

$$P = I^2 R = 1.6\ \text{mW} \tag{3.2}$$

This heating power is small compared with the 2$^{\text{nd}}$ stage cooling power. Also, considering that the magnet was operated in persistent mode, the copper lugs only needed to carry current temporarily during charging/discharging stages.

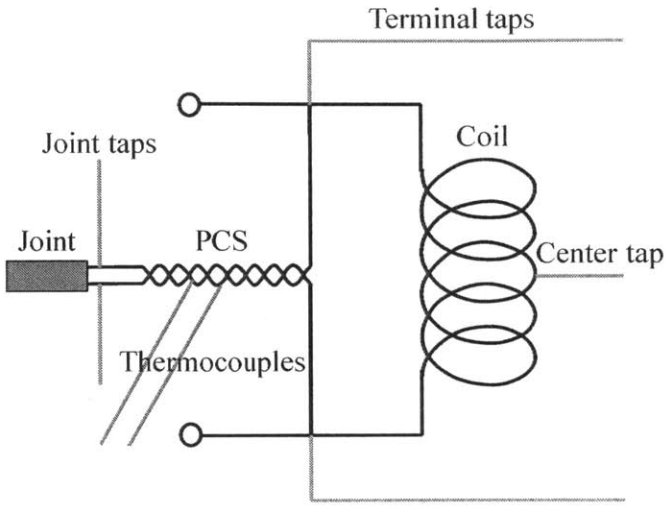

Figure 3-18: Schematic drawing of voltage taps for joint, coil and bridge voltages.

3.3.4 Epoxying Coil Parts

After the copper lugs were soldered, the joint and floating sections of wire were epoxied to the perforated sheet with Stycast for mechanical integrity. Thus, when the magnet energized, the floating sections of the wire were not moved by Lorentz force. Epoxying floating parts also prevented accidental damages to the coil.

In order to electrically insulate the copper lugs from the coil mandrel, as well as to strengthen the epoxy, a layer of fiber glass was inserted between each copper lug and the perforated sheet. Another layer of fiber glass was epoxied on top of each copper lug to reinforce the bond.

3.3.5 Instrumentation

On each coil, a pair of voltage taps at the coil terminals measured the coil voltage, and a pair of taps at the joint measured the joint voltage. Another voltage tap, attached to the middle of the main winding, formed a bridge circuit together with the terminal taps. Figure 3-18 shows schematically the positions of each voltage tap.

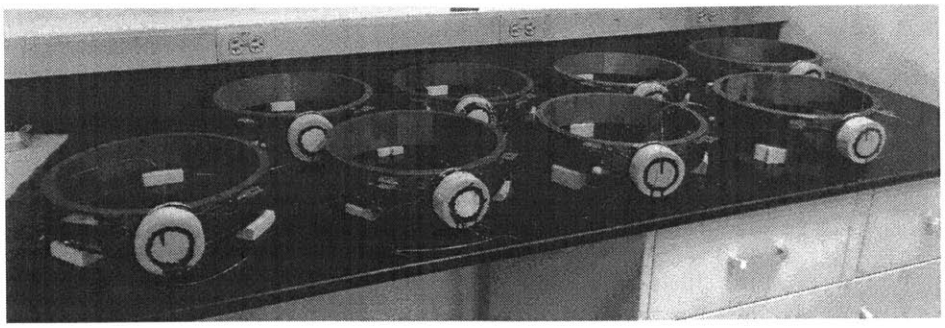

Figure 3-19: All 8 coils successfully completed with wind-and-react procedure.

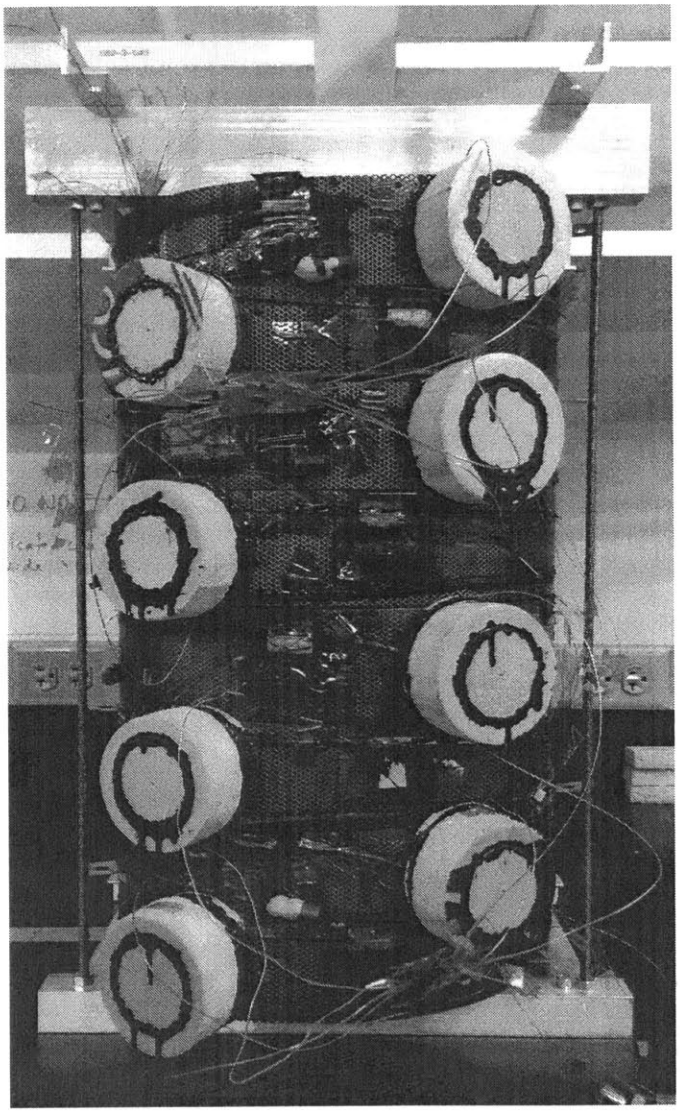

Figure 3-20: The 8 coils assembled, in the designated order, with aluminum beams and threaded rods.

3.4 Assembling

All 8 coils were successfully completed with the wind-and-react procedure. They were assembled in the designated order and fixed with aluminum beams and threaded rods, as shown in Figure 3-20. A thin layer of G-10 sheet was inserted at each contact between the magnet and the aluminum beams, electrically insulating the magnet from the rest of the system.

Chapter 4

Experiment Rig

A simple test rig was built to test single coils and a 3-coil subassembly in liquid helium. The rig contained radiation shields, current leads and supporting structures.

A full test rig was built to operate assembled magnet in solid nitrogen. The rig contains three subsystems of cooling, current leads and instrumentation.

In both tests, a cryostat of 432-mm diameter and 1324-mm depth was deployed to contain the cryogen and the test rig.

4.1 Simple Test Rig

In order to guarantee the performance of the assembled magnet, each of the 8 coils was tested in liquid helium individually before assembled. In addition, a 3-coil subassembly was put together and tested in liquid helium to evaluate performance of multi-coil assembly. A simple test rig, consisting the essential components, was built for these testing goals.

Figure 4-2 shows a schematic drawing of the simple test rig. The top flange was made from a 6.4-mm thick G-10 plate. Three 1/4-20 stainless steel threaded rods, attached to the top flange, were used to hang the coil. Another G-10 plate was bolted to the bottom of the threaded rods to support coils.

Five circular plates of 51-mm thick Styrofoam were inserted between the top flange and the cryogenic environment to reduce convective heat input. A layer of aluminum

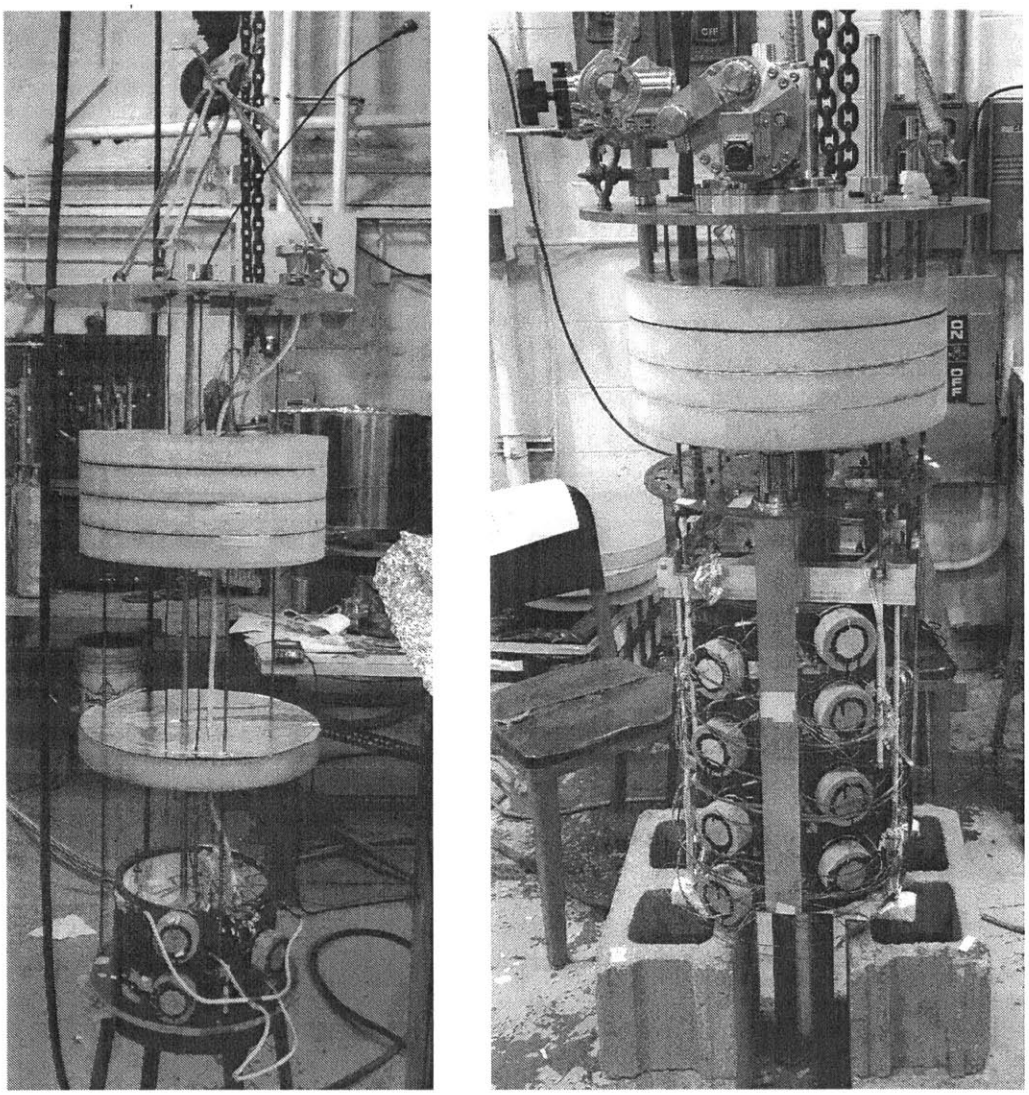

(a) (b)

Figure 4-1: (a) Simple test rig to test single coils and a 3-coil subassembly in liquid helium. (b) Full test rig to test the assembled magnet in solid nitrogen.

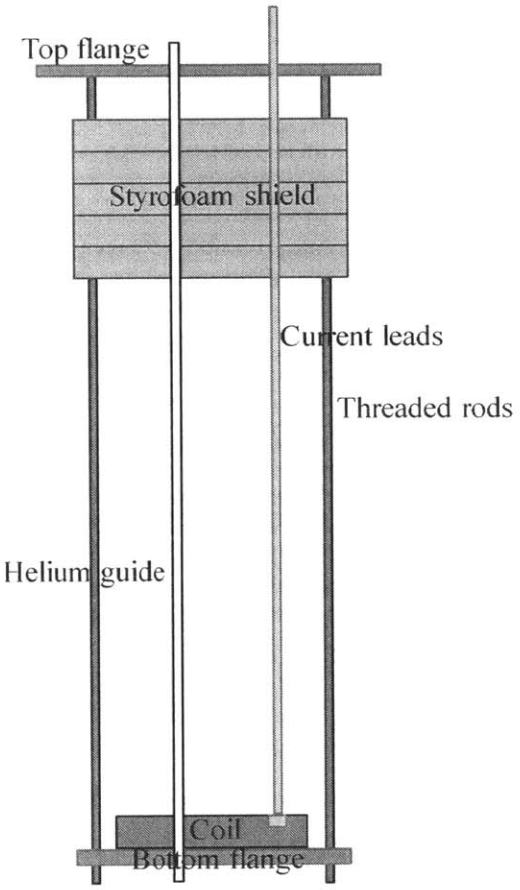

Figure 4-2: Schematic drawing of simple test rig.

foil was attached to each Styrofoam plate to reduce the radiative heat input. A thin-walled stainless steel tube was inserted through the top flange and the bottom flange to guide liquid helium transfer.

A pair of current leads was made of copper wires; each lead consisted of 7 AWG #12 ($\sim\Phi$2 mm) copper wires. The bottom of the copper wires were soldered to a pair of YBCO conductor bundles that was in turn bolted to the lugs on coils. Each YBCO conductor bundle was introduced to reduce conductive heat input to the cold environment through the current leads. Note that each YBCO bundle, containing four 6-mm wide YBCO tapes, had a total copper cross-section of 0.24 mm^2 vs. a $\sim$20 mm^2 copper cross-section in each copper lead.

In each test, a coil, or a coil subassembly, was first pre-cooled by liquid nitrogen to 77 K. The liquid nitrogen was then purged by pressurizing the cryostat before the liquid helium was transferred. Then, liquid helium was transferred to the cryostat to slowly cool the coil from 77 K to the testing temperature range, 4.2-15 K. In tests >4.2 K, the coil, placed above a liquid-helium pool at the cryostat bottom, was cooled by helium vapor. The distance between the coil and the liquid helium level determined the temperature of the coil: the farther away was the coil from the liquid helium level, the higher was the temperature of the coil. Two Cernox sensors were mounted at the top and bottom of each coil to monitor the coil temperatures at these locations during the test.

4.2 Full Test Rig

A full test rig was built to test the assembled magnet in solid nitrogen. Figure 4-1b shows the assembled test rig before it was inserted into the cryostat. The test rig included cooling, current leads, and instrumentation subsystems. Each subsystem is discussed below in detail.

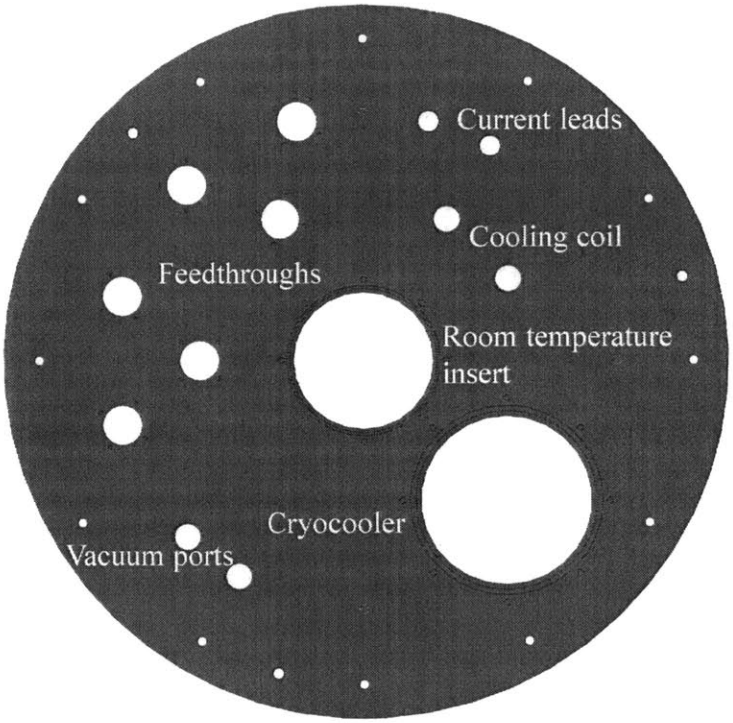

Figure 4-3: Drawing of top flange.

4.2.1 Structure

The top flange was made of a 13-mm thick stainless steel plate to fit the 432-mm cryostat. A Φ102-mm circular hole was cut at the center to mount a room-temperature insert for field mapping. Another Φ126-mm circular hole was cut off-centered to mount the cryocooler. A group of six holes was cut for hermatic feedthroughs. Three pairs of holes were cut in the flange, respectively, for the current leads, the inlet and outlet of the cooling coil, and the vacuum ports.

Four 1/4-20 threaded rods were tightened to the bottom of the flange as the main hanging structure. The shields and Styrofoam plates were fixed to the threaded rods with nuts. The magnet assembly was bolted to the bottom of the rods.

4.2.2 Cooling System

The cooling subsystem provides cooling power to the magnet and keeps it in the operation temperature range 10-15 K. The major cooling source is a GM 2-stage cryocooler. The load map of this cryocooler is shown in Figure 4-6. According to the performance data, shown in Figure 4-6, the cryocooler 2^{nd} stage provides cooling powers of 8 W and 15 W, respectively, at 10 K and 18 K, enough for this magnet to operate in persistent-mode over this temperature range.

During magnet charge-up when all 8 PCS's need to be open with the switch heaters on, the system puts an additional heating load of 6 W, making the total load exceed the 2^{nd} stage cooling capacity. Thus, liquid helium was deployed as an effective, but inefficient, source and forced through a cooling coil, wound from 13-mm diameter copper tube. The cooling coil of 36 turns of copper tube, was placed right next to the inner wall of the magnet, as shown in Figure 4-7. Two 0.25-mm wall 13-mm diameter stainless steel tubes were connected to the inlet and outlet of the copper coil. The thin-walled stainless steel tubes reduce conductive heat input from the top flange at approximately room temperature to the cryogenic environment.

Two circular copper plates of diameter 419-mm were in close contact with the 1^{st} and 2^{nd} stages of the cold heads. The upper copper plate, connected to the 1^{st} stage,

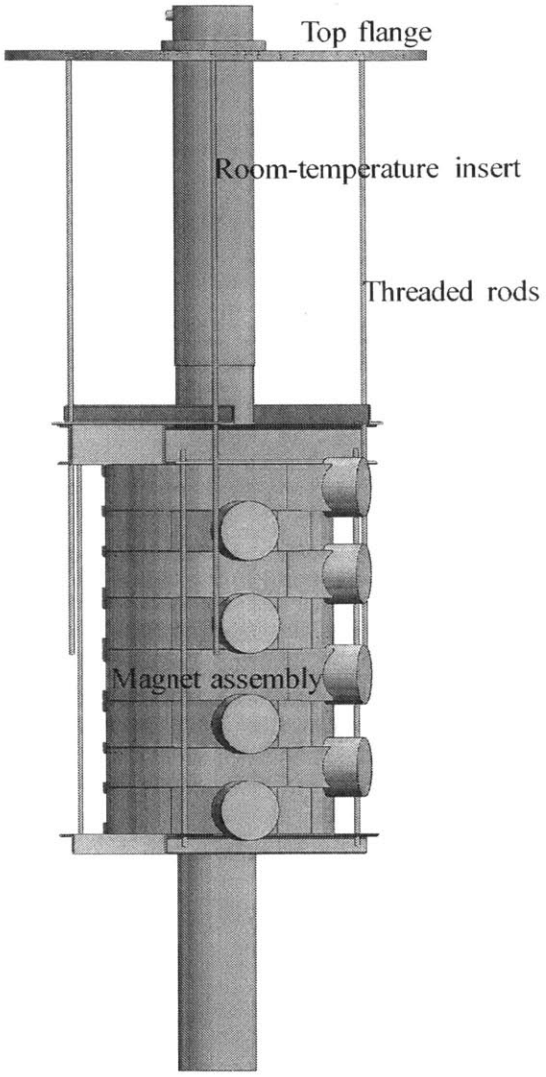

Figure 4-4: Drawing of the full test rig main structure: top flange, room-temperature insert, four stainless steel rods, and magnet assembly.

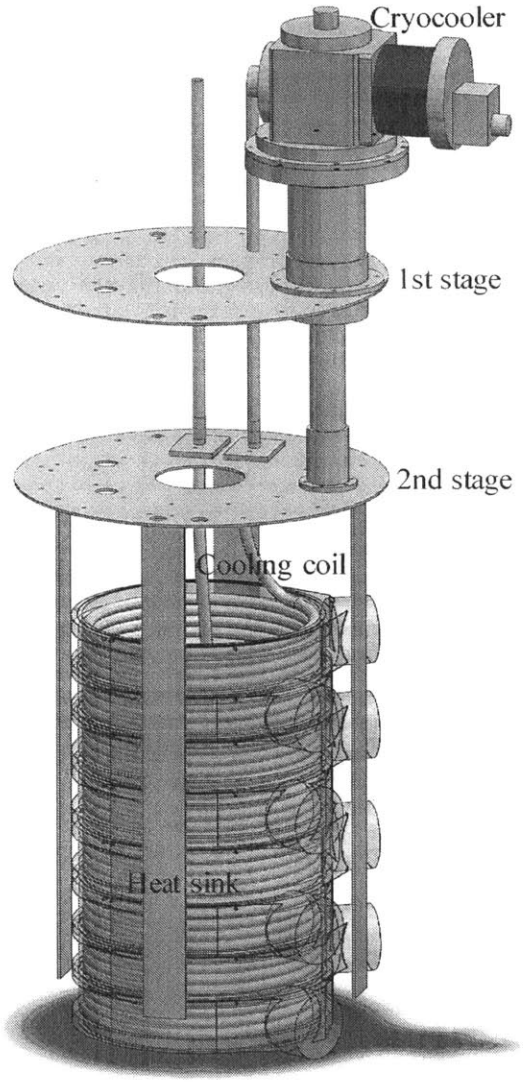

Figure 4-5: Drawing of cooling subsystem: GM 2-stage cryocooler, cooling coil, and heat sink.

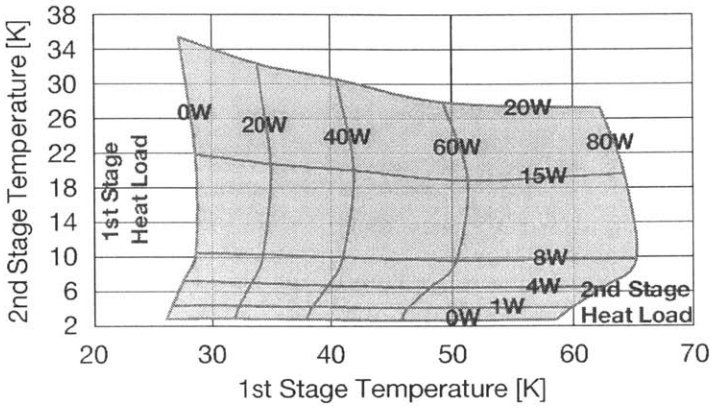

Figure 4-6: Cryocooler performance data.

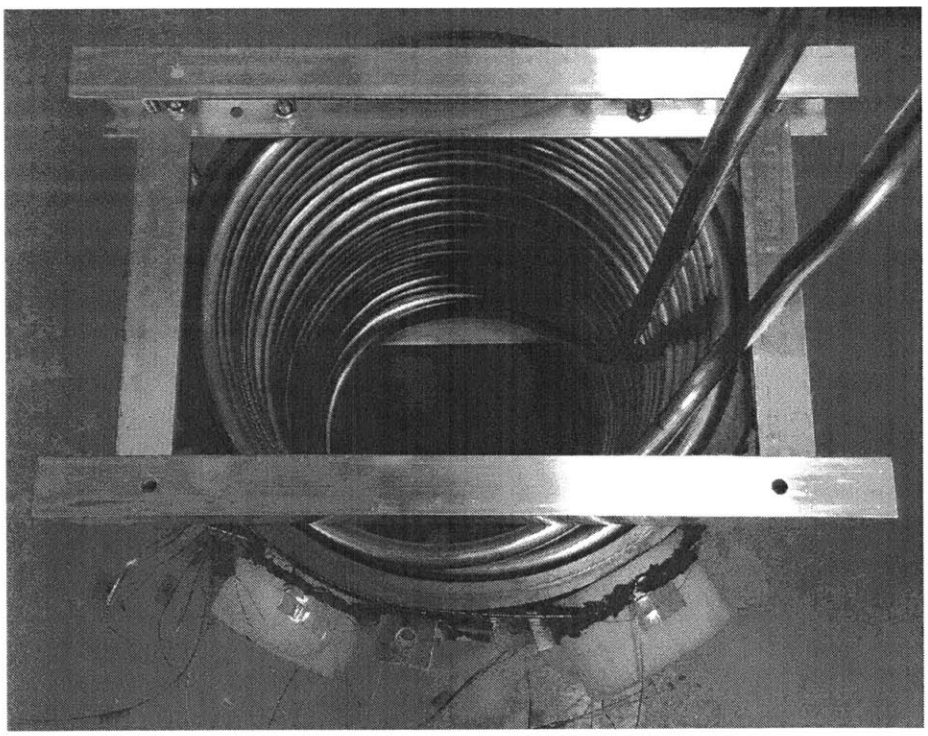

Figure 4-7: Copper cooling coil in the magnet bore.

was deployed to reduce the heat input from the top of the cryostat to the cryogenic environment. The lower copper plate, connected to the 2nd stage, was made of OFHC copper that has better thermal conductivity than normal copper at 10-15 K. Together with four OFHC copper bars bolted to it, the plate served as the heat sink to the cold mass.

The upper copper plate firstly served as a shield to reduce radiative heat input from the top flange. Secondly, it thermally anchored other parts of the test rig, absorbing conductive heat input from the top flange. The plate was fixed to the four threaded rods with aluminum nuts, as shown in Figure 4-8a. Aluminum nuts, instead of stainless steel ones, were used to enhance the conduction between the copper plate and the threaded rods. A section of the instrumentation wires was attached to the copper plate, so that the conductive heat through the wires was significantly reduced before it was conducted further to the cold mass. Figure 4-8b shows the wires attached to the lower side of the Styrofoam plate. Later, when assembling completed, the wires were pressed firmly against the upper copper plate. Two aluminum annuli were placed on the inlet and outlet of the cooling coil. Two copper bars were soldered to the current leads. They are shown in Figure 4-8c. Both the aluminum annuli and the copper bars had good thermal contact with the upper copper plate, so as to reduce the conductive heat input through the cooling coil and the current leads.

In the test system, solid nitrogen was directly poured in the cryostat, without a separate container. The inner wall of the cryostat and the outer wall of the room-temperature insert also conducted heat from outside to the cold mass. In order to restrain this heat input, both walls were anchored to the upper copper plate through copper strips, as shown in Figure 4-9. These copper strips, with a total cross-section of $\sim$80 mm^2, are enough for thermal conduction of 50 W over a distance of 5 mm with a temperature difference of $\sim$6 K.

Four OFHC copper bars, each 610-mm long, 51-mm wide and 3-mm thick, were bolted to the lower copper plate as extended heat sink into solid nitrogen. These bars, with a total cross-section of 612 mm^2, are sufficient to carry 1 W of heat over a distance of 610 mm with a temperature difference of $\sim$1 K. This magnet, surrounded

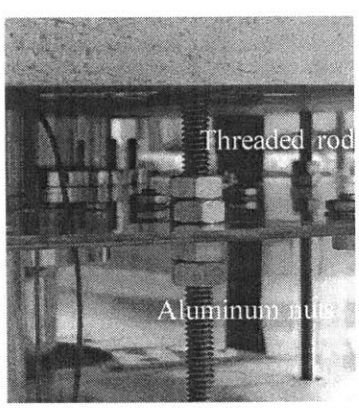

(a)

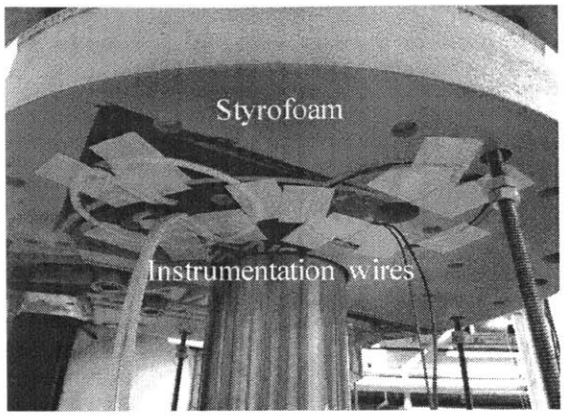

(b)

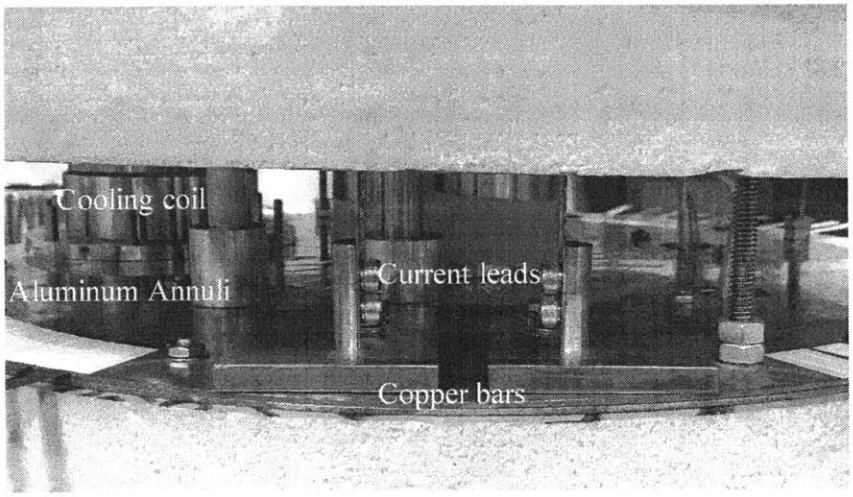

(c)

Figure 4-8: (a) Each stainless steel rod thermally connected to the copper plate through two pairs of aluminum nuts. (b) Instrumentation wires attached to the lower side of Styrofoam plate, to be pressed against copper plate. (c) Inlet and outlet of cooling coil thermally anchored through aluminum annulus; current leads thermally anchored through copper bars.

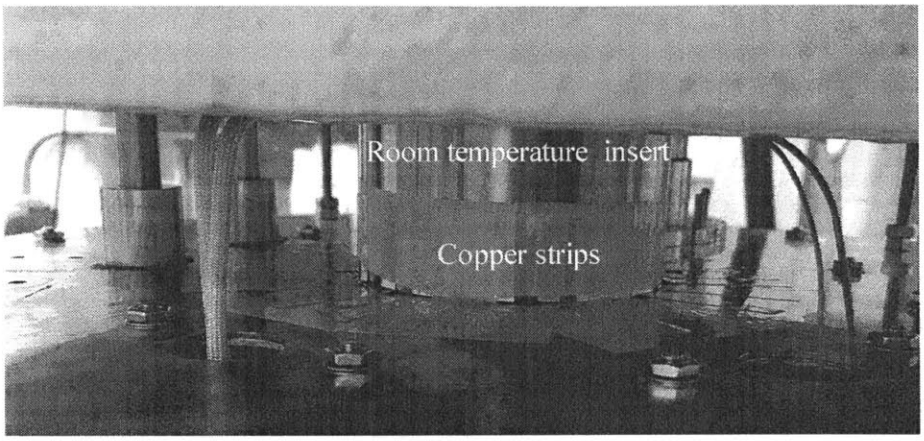

(a)

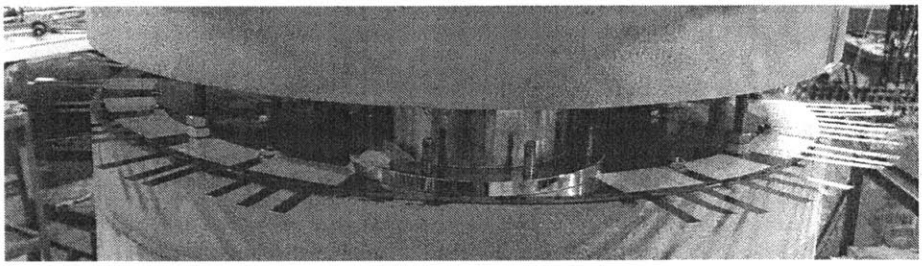

(b)

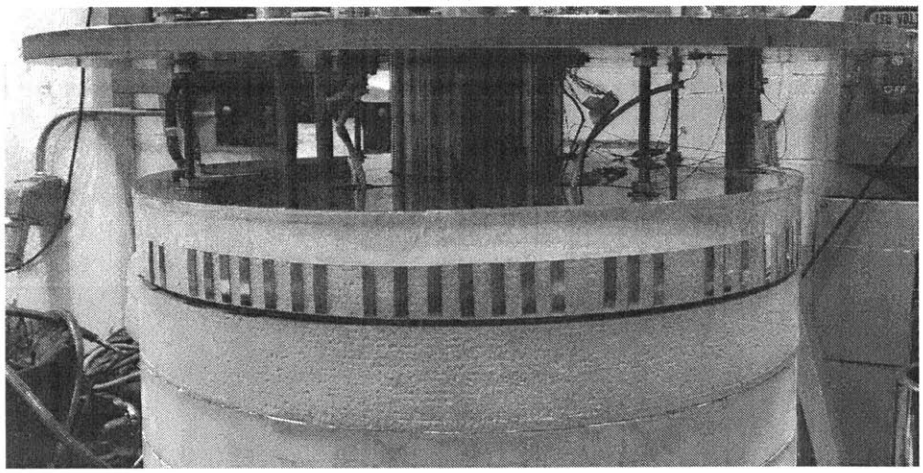

(c)

Figure 4-9: (a) Copper strips connect the outer wall of room-temperature insert to upper copper plate. (b) Copper strips attached to the edge of upper copper plate. (c) Copper strips bent around the Styrofoam plate to be pressed against the inner wall of the cryostat.

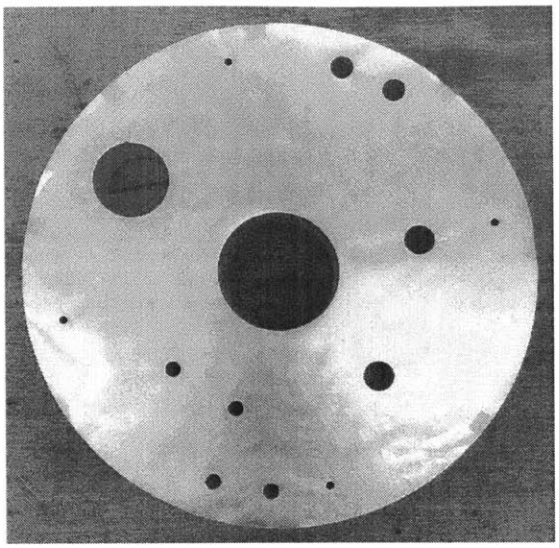

Figure 4-10: Aluminum foil attached to Styrofoam plate.

by a volume of solid nitrogen, is not a conduction-cooled magnet. During cooling, however, the copper bars, inserted in the solid nitrogen, helped conduct heat away from the magnet through the solid nitrogen.

4.2.3 Shields

Four circular Styrofoam plates, one above and three below the upper copper plate, were deployed to reduce conductive and convective heat input to the cold mass. A layer of aluminum foil was attached on the upper side of each Styrofoam plate to reduce radiative heat input.

4.2.4 Current Leads

A pair of current leads was designed to transport 100 A current from the room temperature environment to the cold mass with minimal heat input. Figure 4-11 shows a drawing of a pair of 100-A current leads, secured to the top flange and thermally anchored to the upper copper plate.

Each current lead consists of a lug, a copper band, a copper connector, and a brass-HTS (high temperature superconductor) hybrid lead. Figure 4-12 shows each

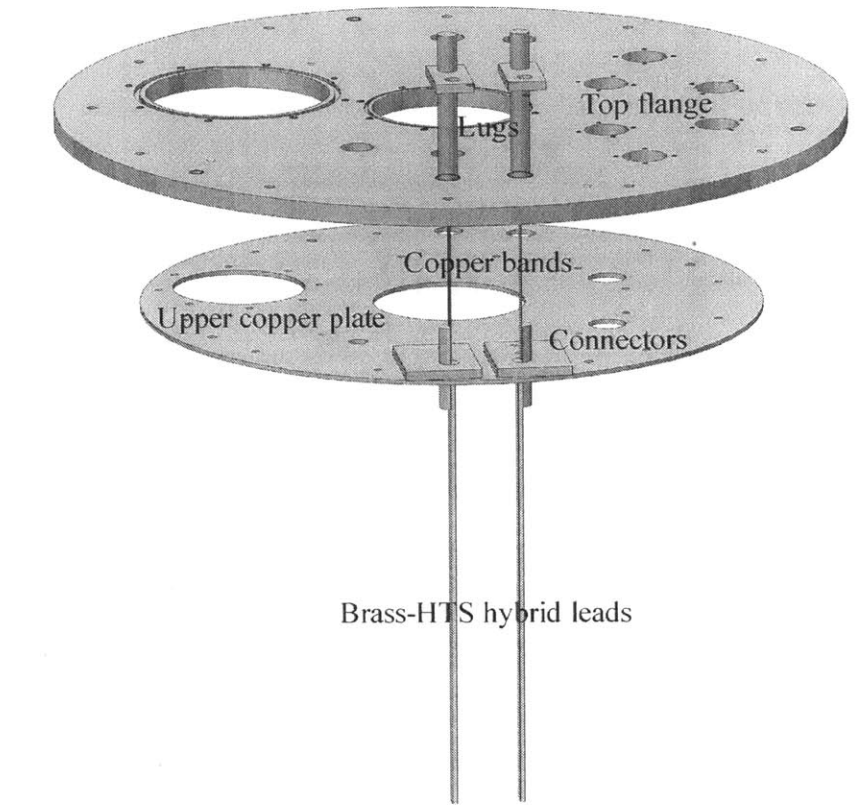

(a)

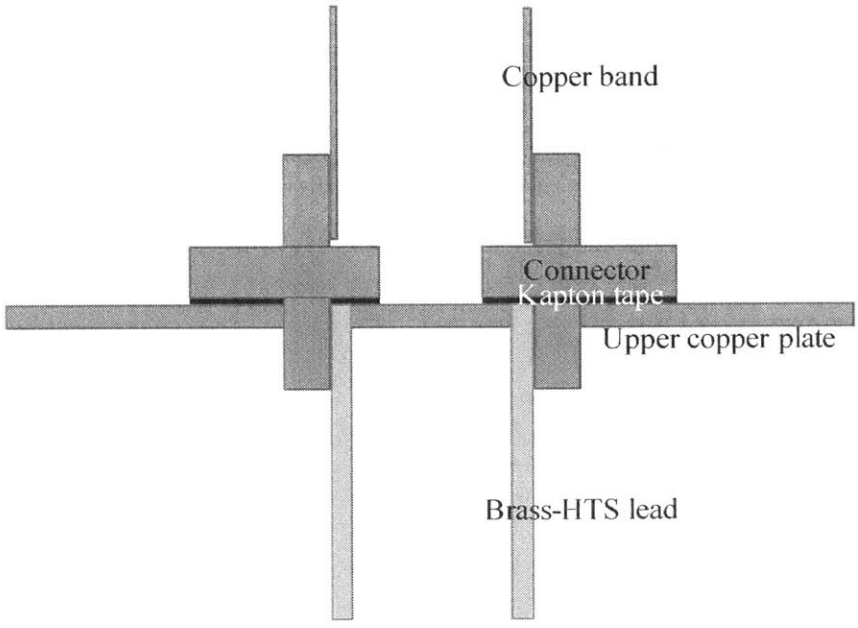

(b)

Figure 4-11: Current leads.

part of the current lead before assembling. The lugs stayed at room temperature, connecting the rest part of the current lead to the power cable. The copper bands connected the room temperature lugs to the intermediate copper connectors that were thermally anchored to the upper copper plate. The hybrid leads then carried current down to the magnet, with their bottom immersed in solid nitrogen.

Each homemade lug was made of a 6-mm thick copper bar soldered to a 13-mm diameter brass rod. The bottom of each brass rod, inserted in a nylon connector, was fixed in a 1/2-in NPT tapped hole on the flange with Stycast.

A copper band was soldered to the bottom of each brass rod. The copper band minimizes conductive heat input with an optimized combination of length and cross-section. The governing equation of conduction in the copper band is

$$A\bar{k}\frac{d^2T}{dz^2} + \frac{\bar{\rho}I^2}{A} = 0 \tag{4.1}$$

where A is the cross-sectional area of each band, l is the length of each band, $\bar{k}$ and $\bar{\rho}$ are the temperature-averaged (in the range 60-300 K) thermal conductivity and electrical resistivity, respectively. The boundary conditions of this differential equation are

$$T(0) = T_o \tag{4.2a}$$

$$T(l) = T_1 \tag{4.2b}$$

where $T_o \cong 300$ K is the room temperature and $T_1 \cong 60$ K is the temperature of the 1^{st} stage cold head. The heat input to the cold end is then

$$Q = -A\bar{k}\frac{dT}{dz}\bigg|_{z=l} = \bar{k}(T_o - T_1)\frac{A}{l} + \frac{\bar{\rho}I^2}{2}\frac{l}{A} \tag{4.3}$$

The optimal parameters of copper band was derived by differentiating Q with respect to A/l and equating it to 0. The optimal parameters satisfies

$$\frac{A}{l} = I\sqrt{\frac{\bar{\rho}}{2\bar{k}(T_o - T_1)}} \tag{4.4}$$

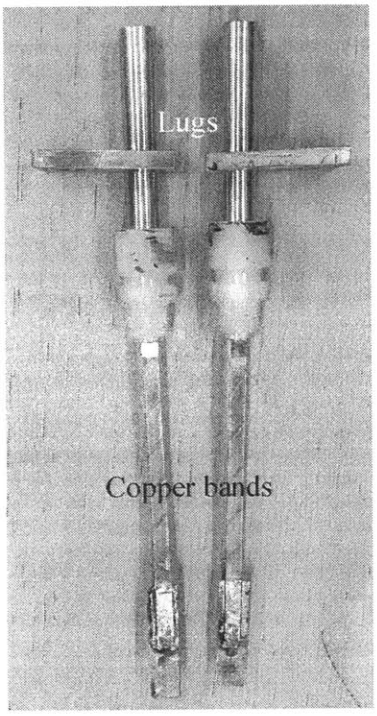

(a)

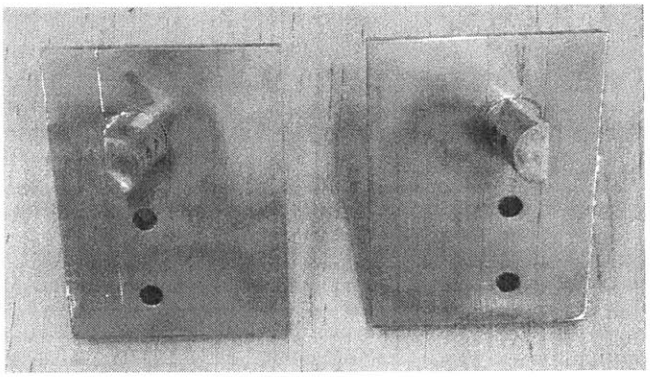

(b)

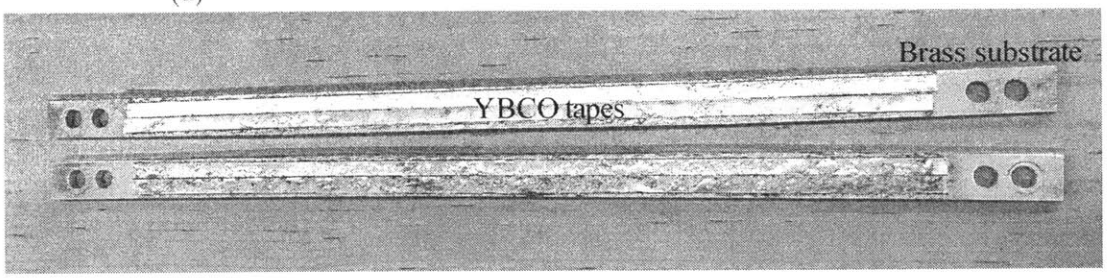

(c)

Figure 4-12: Parts of current leads: (a) lugs and copper bands soldered; (b) back side of copper connectors, Kapton tape insulated; (c) hybrid leads, YBCO HTS conductors soldered on brass bars.

The peak charging current is $I = 100$ A. The copper band length $l = 150$ mm is determined by the distance between the top flange and the upper copper plate. Together with $\bar{k} = 460$ W/mK and $\bar{\rho} = 1 \times 10^{-8}$ Ωm for copper in the range 60-300 K, the optimal cross-sectional area of the copper bands, calculated from Equation 4.4, is 3.2 mm^2. The idle conductive heat leak through each copper band, while not conducting current, is

$$Q = \frac{A\bar{k}(T_o - T_1)}{l} = 2.4 \text{ w} \tag{4.5}$$

Since this magnet was operated in persistent mode, the current leads only needed to carry current temporarily during charging or discharging, for ~10 min in each period. In order to further reduce the idle conductive heat leak, the required cross-section of copper bands must be reduced. The brass rods, during charging/discharging periods, were cooled by liquid nitrogen. In this way, the entire copper bands, cooled from both ends, were at 60-77 K, having a much smaller electric resistivity $\bar{\rho}' = 2 \times 10^{-9}$ Ωm with only a slightly larger thermal conductivity $\bar{k} = 500$ W/mK. Under this cooling condition, a current lead with a much smaller cross-section can still have the same resistance thus generate the same Joule heating as conventional current leads. The modified copper band cross-section is

$$A' = \frac{\bar{\rho}'}{\bar{\rho}} A = 0.64 \text{ mm}^2 \tag{4.6}$$

The new idle conductive heat leak through each copper band with this cross-section is 0.48 W.

A copper connector, in the middle of each current lead, had three functions: (1) thermally anchoring the current lead to the 1st stage cold head; (2) connecting the copper band and a brass-HTS hybrid lead; (3) insulating the current lead from the rest of the system. The copper band was bolted to the upper arm of the connector, and the hybrid lead was bolted to the lower arm of the connector, as shown in Figure 4-14.

The copper connector, body firmly pressed against the upper copper plate for thermal anchoring, was electrically insulated from the copper plate. As shown in

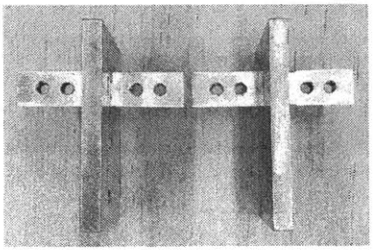

(a)

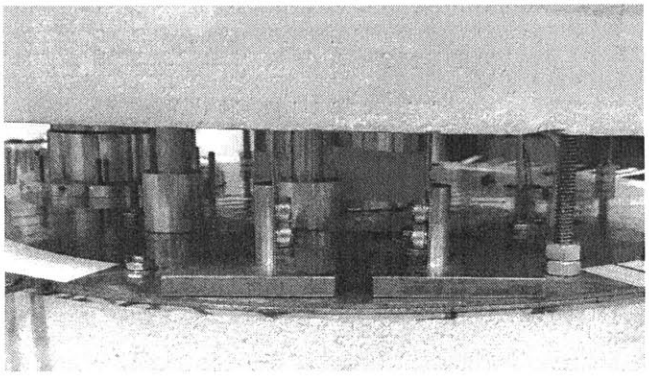

(b)

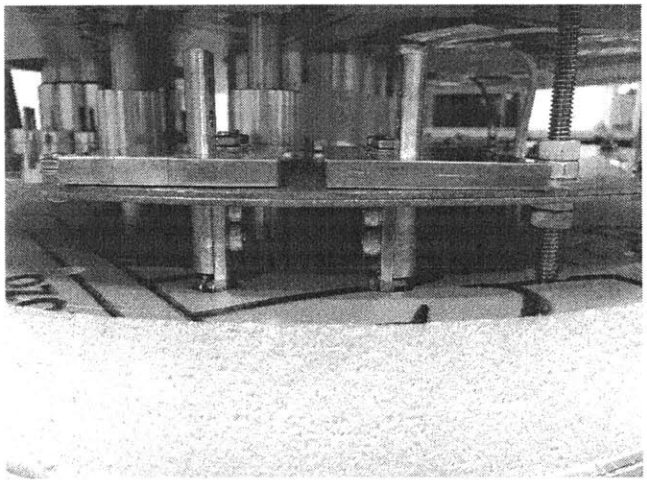

(c)

Figure 4-13: (a) Side view of copper connectors. (b) Copper bands bolted to the upper arm of the connectors. (c) Brass-HTS hybrid leads bolted to the lower arm of the connectors.

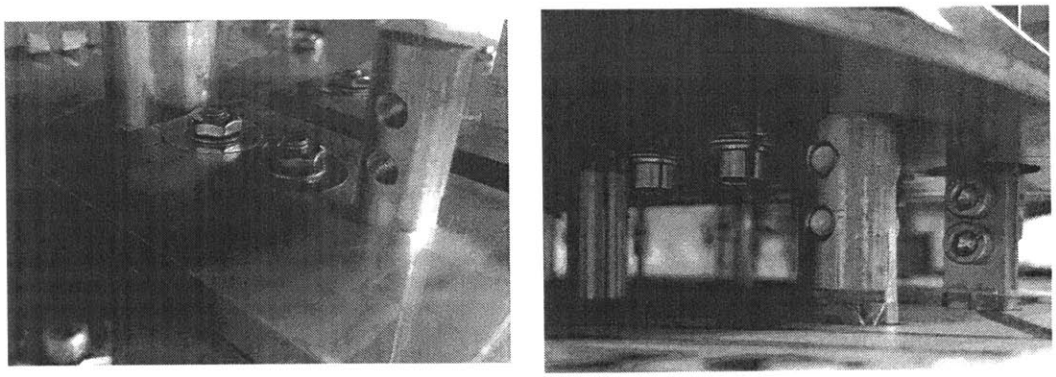

(a) (b)

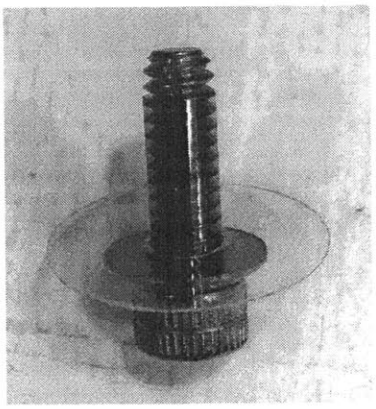

(c)

Figure 4-14: (a) Top side of the connectors. (b) Bottom side of the connectors. (c) Insulated screws.

Figure 4-12b, the lower face of its body that touched the copper plate was covered by a layer of Kapton tape. The screws that bolted the connector to the plate were insulated by Kapton tape as well. Both the screw heads and the nuts were shimmed with mica washers. Thus, the current leads were strictly insulated from the rest of the system.

The brass-HTS hybrid leads were designed to conduct 100 A current from the intermediate connectors at 60-70 K to the magnet at 10-15 K. Six 4-mm wide YBCO superconductors, each able to carry 100 A at 77 K, were soldered on a brass substrate. The brass substrate, each 11-mm wide, 3-mm thick and 300-mm long, was deployed to stabilize the temperatures in the HTS tapes and share current in emergent events when all HTS tapes fail.

In the temperature range 10-70 K, brass has $\bar{k} = 30$ W/mK and $\bar{\rho} = 4.5 \times 10^{-8}$ Ωm [1]. The conductive heat input through each brass substrate from the 1st stage cold head to the solid nitrogen is

$$Q = \frac{A\bar{k}(T_1 - T_2)}{l} = 0.12 \text{ W} \tag{4.7}$$

In case part or all of a brass substrate needs to share 100 A, the Joule heating in every centimeter of a current-sharing section is

$$Q = \frac{\bar{\rho} I^2 l}{A} = 0.22 \text{ W} \tag{4.8}$$

Normally, there would be only conductive heat leak of 0.12 W through each hybrid lead and no Joule heating. This heat is relatively small compared with the 2nd stage cooling power of 8 W at 10 K.

4.2.5 Heat Leak

Three types of heat leak, conductive, convective and radiative, brought heat from the room temperature environment to the cryogenic environment. The cryostat was essentially vacuum during the test, i.e., convective heat input was minimal.

Radiative heat input from the top flange (~300 K) to the upper copper plate (~60 K), with an aluminum shield in between, can be estimated with:

$$Q = \frac{A\sigma(T_o^4 - T_1^4)}{\frac{1-\epsilon_o}{\epsilon_o} + 1 + \frac{1-\epsilon_s}{\epsilon_s} + \frac{1-\epsilon_s}{\epsilon_s} + 1 + \frac{1-\epsilon_1}{\epsilon_1}} \tag{4.9}$$

In the equation, A is the area of the flange and the shield and the copper plate, σ is the Boltzmann constant, T_o and T_1 are the temperatures of the top flange and the upper copper plate, respectively, ϵ_o, ϵ_s and ϵ_1 are the emissivities of the flange, aluminum foil and copper plate, respectively. This equation also approximates the view factors between all surfaces to 1. With $\epsilon_o = \epsilon_1 = 0.6$ and $\epsilon_s = 0.1$, the radiative heat input from the top flange to the upper copper plate is $Q = 3$ W. Similarly, the

radiative heat input from the upper copper plate to the lower copper plate (~10 K), with 2 aluminum shields in between, can be estimated to be $Q = 5$ mW.

The paths of conductive heat input include: the outer wall of the room-temperature insert, four threaded rods, current leads, stainless steel extensions of the cooling coil, instrumentation wires, and the inner wall of the cryostat. The walls of the insert and the cryostat, the threaded rods and the cooling coil extensions are made of stainless steel. The current leads and instrumentation wires are made of copper. The temperature-averaged thermal conductivities $\bar{k}_{\mathrm{ss,80-300\,K}} = 13$ W/mK, $\bar{k}_{\mathrm{cu,80-300\,K}} = 460$ W/mK, $\bar{k}_{\mathrm{ss,4-80\,K}} = 4.5$ W/mK, and $\bar{k}_{\mathrm{cu,4-80\,K}} = 1300$ W/mK [1] were used to estimate the total conductive heat leak.

The total cross-sectional area of the stainless steel parts is

$$A_{\mathrm{rods}} + A_{\mathrm{walls}} + A_{\mathrm{tubes}} = 1.3 \times 10^{-4} + 1.8 \times 10^{-3} + 2 \times 10^{-5} \cong 2 \times 10^{-3}\ \mathrm{m}^2 \quad (4.10)$$

The distance between the top flange and the 1st stage is 0.1 m. Through the stainless steel parts:

$$Q = \frac{A\bar{k}(T_o - T_1)}{l} = 60\ \mathrm{W} \quad (4.11)$$

Through the two current leads:

$$Q = \frac{A\bar{k}(T_o - T_1)}{l} = 0.9\ \mathrm{W} \quad (4.12)$$

Through the instrumentation wires

$$Q = \frac{A\bar{k}(T_o - T_1)}{l} = 2\ \mathrm{W} \quad (4.13)$$

The total conductive heat leak from the room temperature environment to the 1st stage cold head is ~60 W, in which conduction through the wall of the cryostat is the largest contributor. Including radiative heat leak, according to the cryocooler performance data, the 1st stage would stable around 50 K.

Conductive heat leak from the 1st stage to the 2nd stage can be estimated similarly.

Through the stainless steel parts:

$$Q = \frac{A\bar{k}(T_1 - T_2)}{l} = 1.8 \text{ W} \tag{4.14}$$

Through the instrumentation wires

$$Q = \frac{A\bar{k}(T_1 - T_2)}{l} = 0.12 \text{ W} \tag{4.15}$$

Through the two current leads, a total heat input of 0.24 W was calculated in Section 4.2.4. The total heat input from the side of the cryostat and the room-temperature insert is ~2 W, according to the manufacturers. The total heat input to the cold mass is then ~4 W. According to the performance data shown in Figure 4-6, the 2nd stage cold head delivers a cooling power of 4 W at ~6 K.

4.2.6 Instrumentation

As described in Sections 3.3.2 and 3.3.5, each coil had two pairs of voltage taps on its joint and across its terminals, respectively. There was also, on the coil, a center voltage tap, a pair of PCS heaters and a pair of thermocouples in the PCS. Besides those, 8 Cernox temperature sensors and 8 thermocouples were installed at different locations on the test rig. Figures 4-15 and 4-16 show the locations and labeling of these temperature sensors. A cryogenic Hall sensor, free to move along the axis, was placed on the magnet axis.

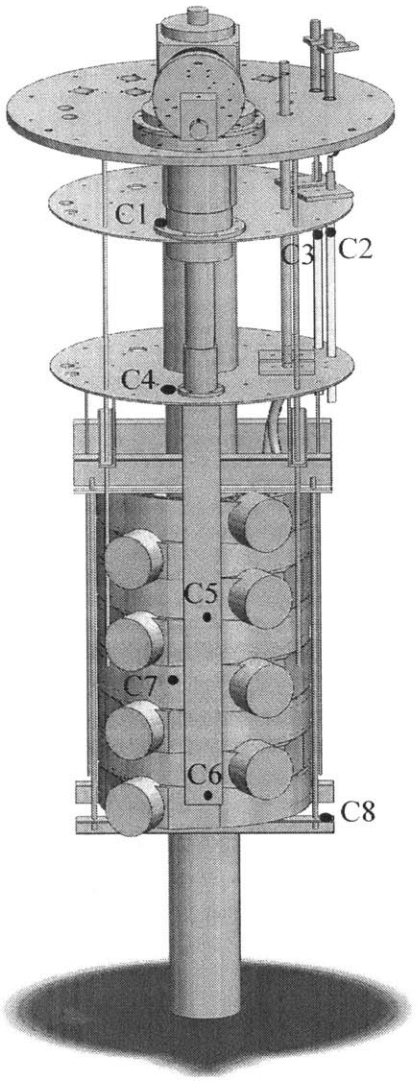

Figure 4-15: Locations of 8 Cernox sensors. C1: 1st-stage cold head; C2: hybrid lead +; C3: hybrid lead -; C4: 2nd-stage cold head; C5: heat sink middle; C6: heat sink bottom; C7: magnet middle; C8: magnet bottom.

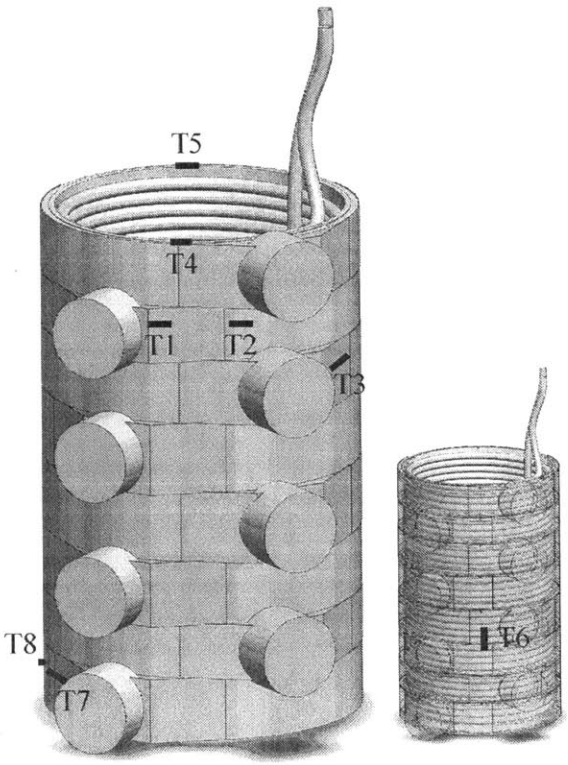

Figure 4-16: Locations of 8 thermocouples. T1: Coil 2 PCS; T2: Coil 2 right lug; T3: Coil 3 PCS; T4: Magnet top front; T5: Magnet top back; T6: Cooling coil bore; T7: Coil 8 PCS; T8: Coil 8 left lug.

Chapter 5

Performance

5.1 Solid Nitrogen

In order to obtain crystalline rather than foamy solid nitrogen (SN2), the liquid nitrogen (LN2) has to be solidified gradually. Nitrogen has a saturation liquid-to-solid phase transition at 63.16 K and 93.45 torr (0.122 atm). In this test, the following procedure was employed to solidify nitrogen, initially liquid at 77.364 K at 1 atm:

1. fill 77-K LN2 into the cryostat;
2. Pump on the LN2 to cool the liquid;
3. At ~65 K, stop pumping and turn on the cryocooler to further cool and solidify the nitrogen.

Pumping was stopped at ~65 K when the nitrogen was still in liquid phase. Continuous pumping to its triple point could cause the nitrogen to solidify too fast and unevenly, forming foamy SN2 [36]. With the cryocooler on, the LN2 could solidify from the cold copper bars attached to the 2^{nd} stage, and form crystalline solid gradually.

The total initial LN2 volume required was estimated based on the SN2 volume in the cold mass and LN2 volume lost through vaporization from 77 K to 65 K. To fill the space around the magnet, a total volume of $V = 0.06$ m^3 is needed. The density

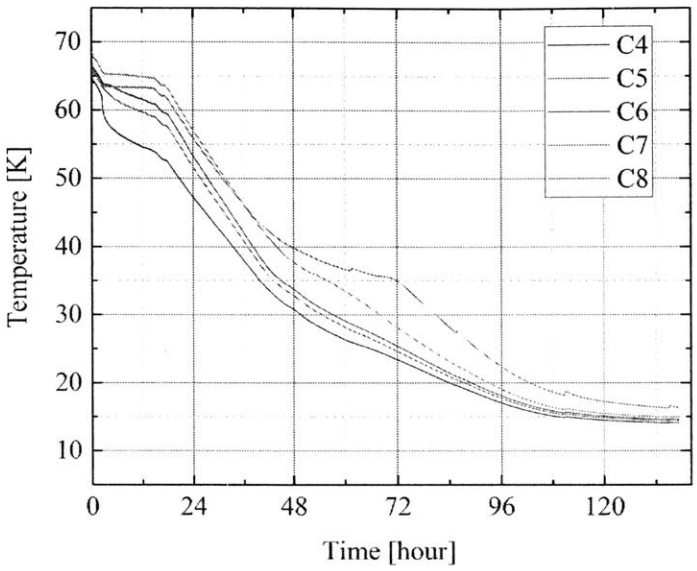

Figure 5-1: Measured temperature vs. time plots, from ~65 K to ~15 K, of the SN2, cooled by a cryocooler.

of LN2 at 77 K is $\rho = 807$ kg/m^3. Therefore, the required LN2 mass is

$$m = \rho V = 48 \text{ kg} \tag{5.1}$$

which corresponds roughly to a 77-K liquid volume of ~60 liters. Assume an amount of x kg of nitrogen needs to be vaporized to bring the 48 kg of LN2 from 77 K to 65 K. The approximate enthalpy balance equation is

$$m(h_{77K,l} - h_{65K,l}) = x(h_{77K,g} - h_{77K,l}) \tag{5.2}$$

Plug in the enthalpy data of nitrogen [1], I obtained $x = 6$ kg. Thus, a total of 54 kg LN2 was initially poured into the cryostat.

The cryocooler was able to cool the 60 kg nitrogen from 65 K to 15 K in less than a week. Figure 5-1 shows cooling curves measured at different Cernox sensor locations. Two plateaus in the curves at 63 K and 35 K, respectively, indicate the liquid-solid and solid-solid phase transitions of nitrogen. The cooling rates were 7×10^{-5} K/s during

solidification and 2.5×10^{-4} K/s after solidification, slower than the cooling rate of 0.001 K/s used by T. Nakamura [36], guaranteeing crystalline SN2. The temperature difference between the heat sink and the bottom of the SN2, when the temperature eventually stabled at ~15 K, was <1 K, proving an even temperature distribution in SN2.

An important characteristic of SN2 is that at ~50 K its thermal conductivity increases as temperature decreases. Together with heat capacity decreasing with decreasing temperature, SN2 has a relatively large thermal diffusivity at cryogenic temperature. Table 5.1 summarizes and compares the thermal diffusivities of solid neon (SNe), SN2 and copper [1]. Noting that most fluids have thermal diffusivities in the order of 1 mm^2/s, SN2 has a fairly large diffusivity below 10 K. Considering thermal diffusivity, the ideal operating temperature for SN2 is <20 K, so as to have prompt temperature response in SN2.

When operated at 10-15 K, because of much greater thermal conductivity compared with other common insulating materials such as Kapton, Nylon, Mylar used in superconducting magnets [1], the temperatures at different locations in the magnet were within 1 K. Figure 5-2 shows temperature vs. time plots at the top, middle and bottom of the magnet, respectively. The data indicate that although no thermally conductive (e.g., copper) connectors were placed between adjacent coils in the magnet, SN2 has proven an effective agent in making the magnet temperature nearly

Table 5.1: Thermal Diffusivities of SNe, SN2, and Cu in 5-60 K Range [1]

T $[K]$	SNe	SN2	Cu
5	35	157	3.6×10^5
10	22	70	1.7×10^5
20	0.27	0.58	2.9×10^4
30	–	0.22	8000
34	–	0.16	5000
37	–	0.18	3500
40	–	0.17	2800
50	–	0.13	1200
60	–	0.12	600

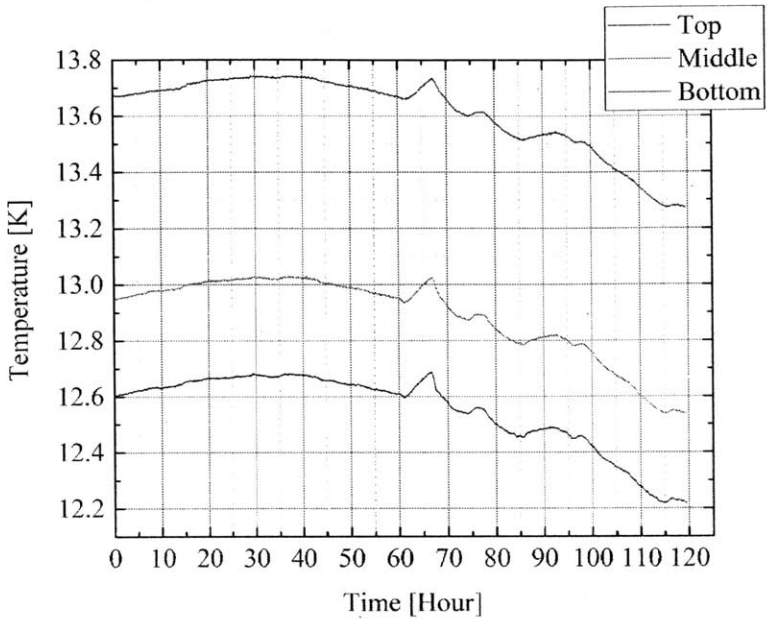

Figure 5-2: Temperatures, within 1 K at the top, middle and bottom of the magnet, plotted vs. time.

uniform [24]. In the following sections, when a magnet temperature is mentioned, it refers to the middle temperature.

One drawback of SN2 is its relatively large thermal contraction. Common metals, including copper and stainless steel, have linear thermal contraction coefficients between 0.02% and 0.03% when cooled from 65 K to 10 K. However, SN2, when cooled from its triple point 63 K to 10 K, has a thermal contraction coefficient of 3%. This difference in thermal contraction may cause damage to mechanically vulnerable or unsecured parts immersed in SN2, e.g., HTS tapes. Figure 5-3 shows a photo of a short piece of YBCO tape kinked by SN2. Other parts, as long as they were epoxied to a rigid surface or reinforced with copper tapes, turned out to be intact.

5.2 Joint

Because the resistance of a superconducting joint is too small to be measured with four-probe method, I wound a small coil, equipped with a PCS and terminated with

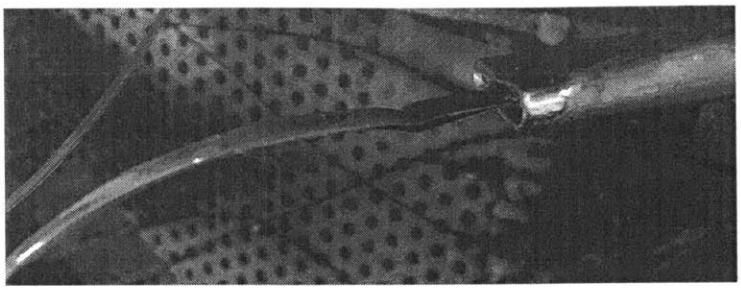

Figure 5-3: YBCO tape kinked by SN2 due to different thermal contraction coefficients.

a joint, and measured its field decay to determine the upper limit of joint resistance.

The coil, with the PCS open, was charged to 75 A at 5 K. It warmed up slowly in gas helium until it quenched at 25 K. During 8-15 K over a period of ~4.5 hours, the coil maintained a persistent current of 74.6 A without any observable decay, as shown in Figure 5-4. Since the coil has a designed inductance of $3 \times 10{-}5$ H, the calculated joint resistance is then given by:

$$R = \frac{L}{I}\frac{\Delta I}{\Delta t} = 3 \times 10^{-12}\ \Omega \tag{5.3}$$

The joint resistance has an upper limit of 3 pΩ, small enough for persistent-mode operation of a typical MRI magnet having even more than 10 such joints.

5.3 Persistent Current Switch

5.3.1 Open/Close in Helium

A sample PCS was tested in both liquid and gas helium. It required 3 W in liquid helium at 4.2 K and 1 W in gas helium at 5 K, respectively, to keep the PCS above 40 K and open, i.e., in the resistive state. In gas helium at 5 K, the PCS was cooled from 40 K to 5 K in 3 minutes, as shown in Figure 5-5.

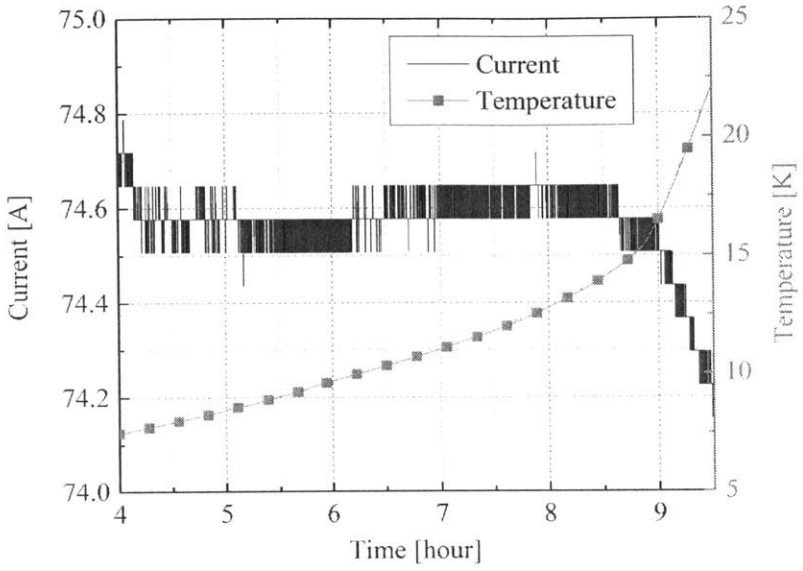

Figure 5-4: Current and temperature vs. time plot of a small-coil test. Current, persistent at 8-15 K for 4.5 hours, indicating joint resistance <3 pΩ.

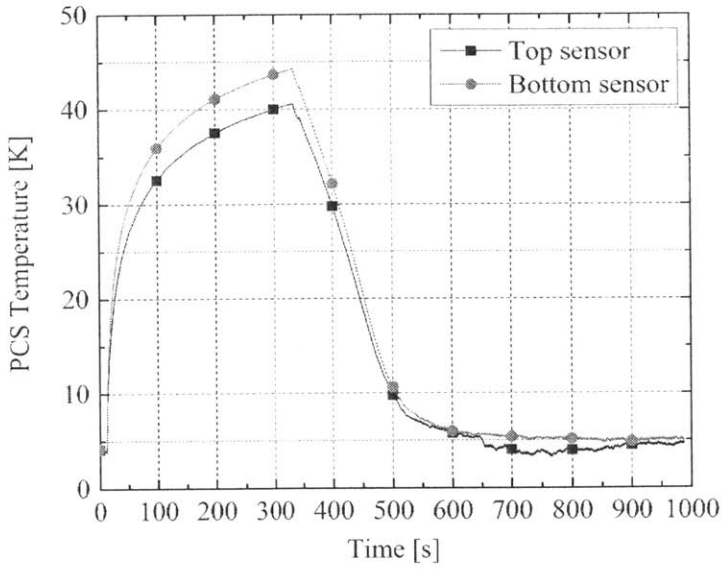

Figure 5-5: Temperature vs. time plot of PCS open/close operation in helium vapor. PCS required 1 W to remain open. It closed in 3 minutes.

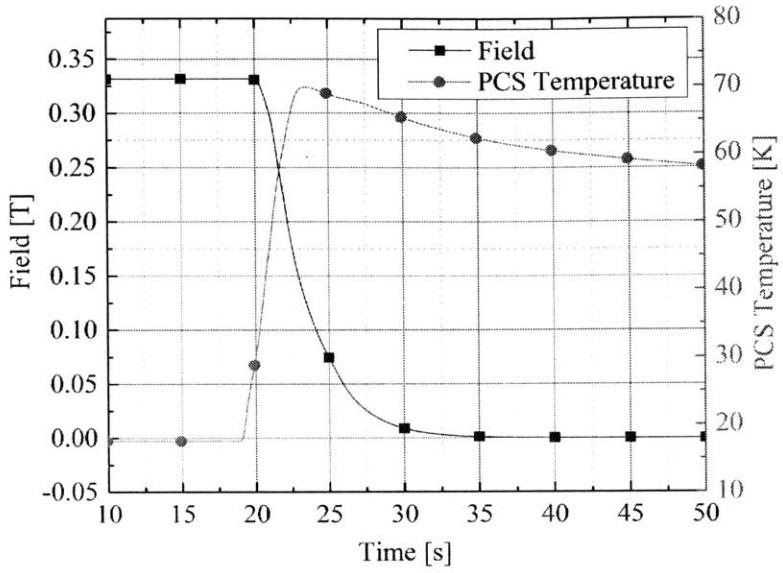

Figure 5-6: Field and temperature vs. time plots during a PCS dump, showing a dump time constant of 3 s. PCS remained below 70 K.

5.3.2 Protection

Each of the 8 coils was protected by a detect-and-activate-the-heater (for short, detect-and-heat) protection technique [1]. Each PCS, as introduced in Section 2.7, served as the dump resistor. When a normal zone is detected, the PCS heater is turned on, heating the PCS above 40 K, which in turn triggers the dump of the stored magnetic energy to protect the normal zone.

As shown in Figure 5-6, in a test, the dump was triggered in 1 s when 0.4 A was put into the PCS heater. A fast-acting capacitor-based switching circuit can shorten this activation time to less than 0.1 s. The measured dump time constant was 3 s, fast enough to protect the magnet operating at 100 A. The PCS, after absorbing the energy, remained below 70 K, so that the thermal stress caused by the temperature gradient would not damage the wire in the PCS.

5.4 Single Coil Persistent-Mode

Upon successful joint result and protection operation of a PCS, I proceeded to manufacture and subsequently test all 8 coil modules. Each coil was tested in persistent mode at 100 A up to 18 K and at 50 A up to 31 K, at which most coils quenched. Figure 5-7 and Figure 5-8 show the persistent-mode operation at 100 A of Coil 3 and 50 A of Coil 7 (Coil 1 through 8 label coils top to bottom). In the 50-A test, Coil 7 current remained constant at 50 A until the coil temperature rose to 26 K, when the current started to decay slightly. The coil quenched from 50 A at 31 K. The result of 100-A test indicated the feasibility of persistent-mode operation at 100 A in the range 10-15 K.

5.5 3-Coil Assembly

5.5.1 Charge and Discharge

A 3-coil subassembly of the 8-coil magnet was assembled and tested in a helium vapor environment to prepare for the test of the full magnet. Because each coil formed a complete superconducting loop, it was interesting to explore the charging and discharging process. Based on the circuit analysis in Section 2.5, each coil in this 3-coil assembly can be charged and discharged simultaneously when all PCS's are open. I successfully achieved charge-and-discharge operation up to 30 A, with a short ($\sim$200 s) period of persistent field in between, as shown in Figure 5-9.

5.5.2 Persistent-Mode Operation

Thereafter, I charged the 3-coil assembly to a target current of 100 A at 5 K. The assembly was warmed up by natural convective heating of helium vapor to a target temperature range 10-15 K. When the top temperature of the assembly reached 10 K, a slight field decay was observed. I then circulated liquid helium to cool the assembly and let it warm up to observe its subsequent field response. The field decayed again at 11 K from 99 A to 98.5 A. After the second decay, the center field was persistent

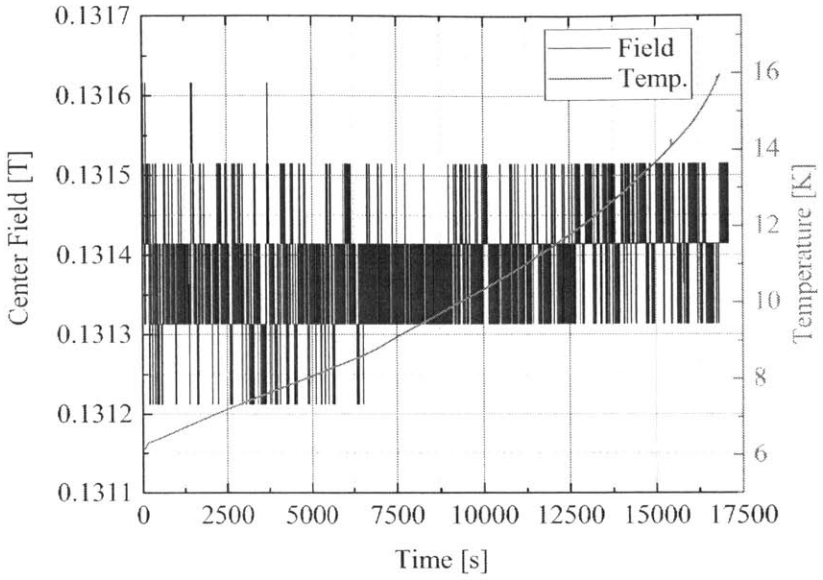

Figure 5-7: Persistent-mode operation of Coil 3 at 100 A in the range 6-16 K.

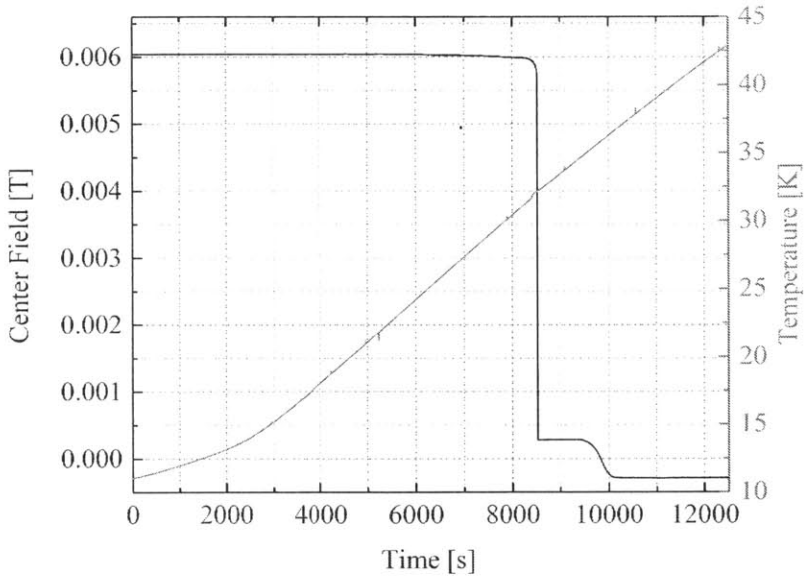

Figure 5-8: Persistent-mode operation of Coil 7at 50 A. Field decayed at 26 K. Coil quenched at 31 K.

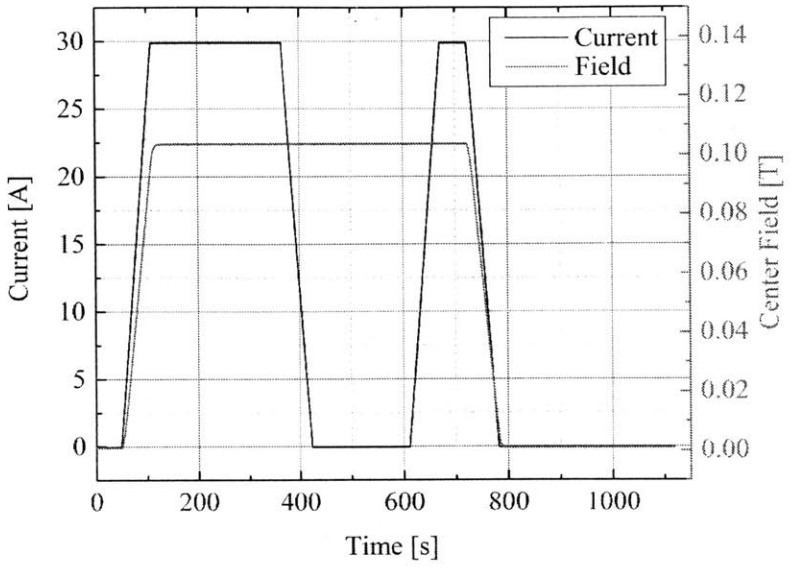

Figure 5-9: Current and field vs. time plots during charge-and-discharge operation of a 3-coil assembly. The assembly appeared in persistent mode for a period of ~200 s.

at 0.333 T for 3 hours, in the range 5-12 K, before it decayed again at 12 K. The 0.333-T center field corresponded to a current of 98.5 A. The field and temperature vs. time plots are shown in Figure 5-10. Overall, in the 3-coil assembly, persistent-mode operation was observed over three periods, each a few hours in duration.

Although the subassembly did not operate at a target current of 100 A in the desired temperature range, it still carried persistent currents, 100 A and 98.5 A, as long the average assembly temperature remained within ranges up to, respectively, 10 K and 12 K. The <1 A/K current drop from 10-12 K indicates a persistent current of ~95 A up to 15 K.

A bridge circuit was set up across each coil to detect a possible resistive coil voltage. By examning the bridge voltages, I found that with the top warmest coil (Coil 1 in the subassembly, and Coil 6 in the whole magnet) the start of its resistive voltage at each persistent-field level coincided with that of field decay, as plotted in Figure 5-11.

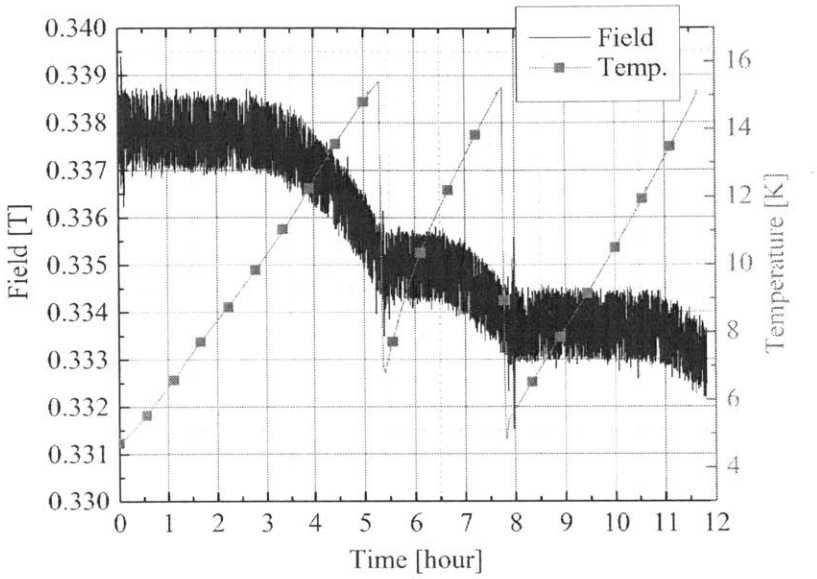

Figure 5-10: Field and temperature vs. time plots of a 3-coil assembly in persistent-mode operation observed over three periods, each a few hours in duration as the assembly temperature continuously rose from a starting temperature. Field decayed at 10 K, 11 K, and 12 K, with currents at 100 A, 99 A, and 98.5 A, respectively.

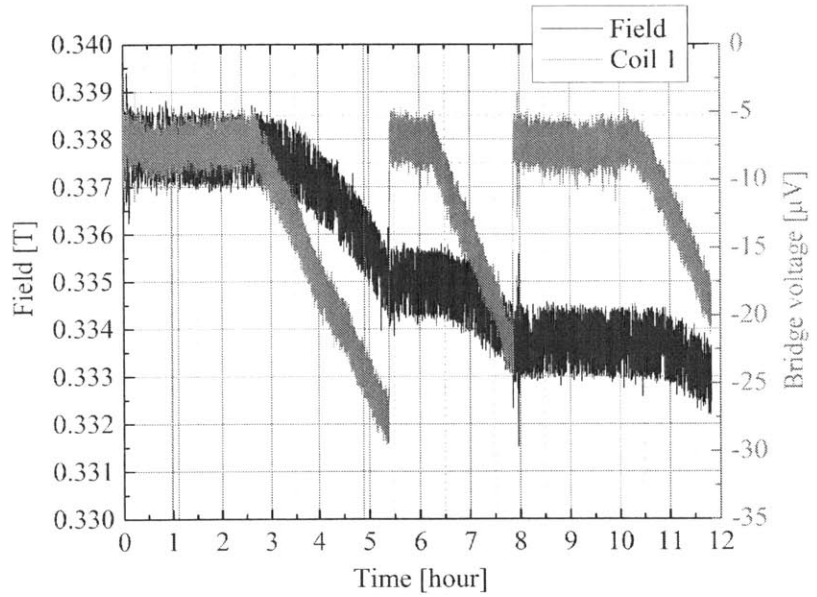

Figure 5-11: Coil 1 bridge voltage and field vs. time plots at three persistent-mode fields. At each field level, the field decays when the voltage begins to rise.

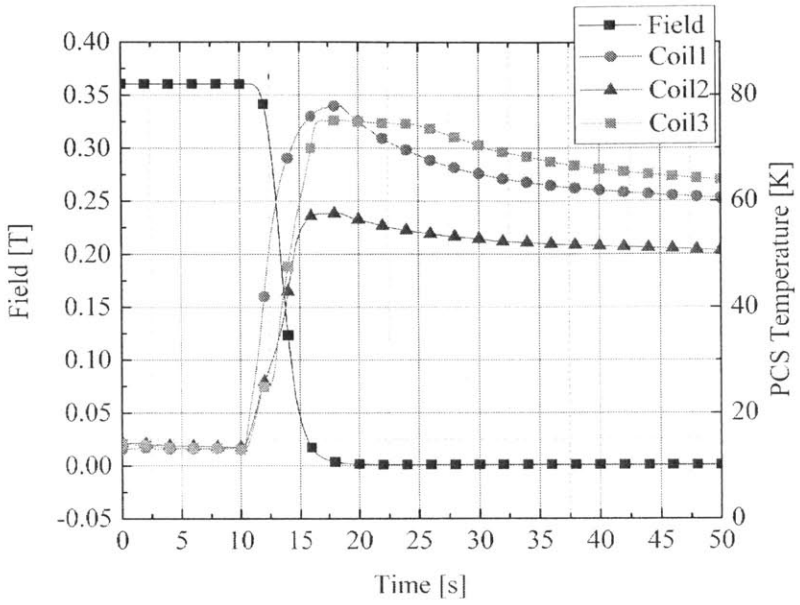

Figure 5-12: Center field and PCS temperatures vs. time plots of the 3-coil assembly during a dump. Each PCS temperature remained below 80 K.

Using the bridge voltage, I estimated the average resistance in Coil 1 to be

$$\bar{R} = \frac{2\bar{V}_b}{I} = \frac{25 \times 10^{-6}}{100} = 2.5 \times 10^{-7}\ \Omega \tag{5.4}$$

This result matches the value estimated from the field decay

$$\bar{R} = L\frac{dI}{dt}\frac{1}{I} = 0.2 \times \frac{1}{7200} \times \frac{1}{100} = 2.8 \times 10^{-7}\ \Omega \tag{5.5}$$

5.5.3 Protection

In the 3-coil assembly, where the coils were connected in series, all coils needed to be dumped simultaneously to avoid unwanted high current induced by mutual inductance. The dump curve of the assembly is plotted in Figure 5-12. During this dump sequence, PCS temperature sensors indicated that each PCS remained below 80 K.

5.6 Full Magnet

The full magnet of 8 coil modules was assembled and tested in solid nitrogen. The test rig and instrumentation were described in Chapter 4.

5.6.1 PCS in SN2

The open and close operation of the PCS's in SN2 was less prompt than the same operation in gas or liquid helium. Figure 5-13 shows the temperature vs. time plots of a PCS during a typical complete open-and-close cycle. PCS open time depends on heating power; with a 1-W heating power, a PCS fully opened in ~10 minutes. Each PCS required a heating power of 0.7 W to maintain at >40 K, compared with 1 W in gas helium and 3 W in liquid helium. It took each PCS ~25 minutes to fully close in SN2, in comparison with 3 minutes in gas helium. To open in SN2, a PCS heated up the SN2 around it; to close it, additional thermal energy stored in the surrounding SN2 needed to be taken away, requiring longer cooling time or stronger cooling power. In contrast, when a PCS was cooled by helium vapor, its surrounding was always replenished with cold helium vapor, making the PCS to close much quickly. Schematic drawings in Figure 5-15 indicate different thermal environments for the two cases.

Two approaches can facilitate PCS close operation: (1) place a PCS next to the cold head; (2) provide additional cooling power to the system. In my thesis, the second approach, though not practical in a real system, was employed with additional cooling from liquid helium. During another test, liquid helium was continuously transferred through the cooling coil to provide an additional cooling power. A volume meter was connected to the outlet of the cooling coil to measure the helium vapor. From the outlet helium volume flow rate measurement, I estimated a cooling power of 8 W. With this additional 8 W, the PCS was closed in ~10 minutes.

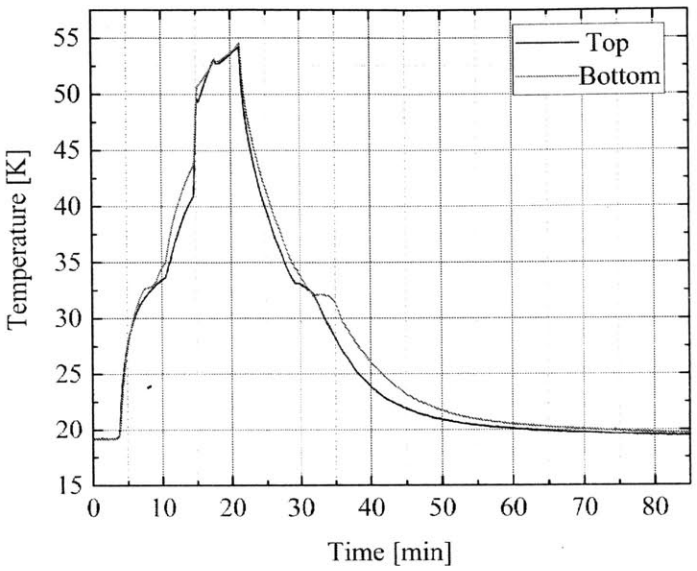

Figure 5-13: Temperature vs. time plots of PCS open/close operation in SN2 at 19 K.

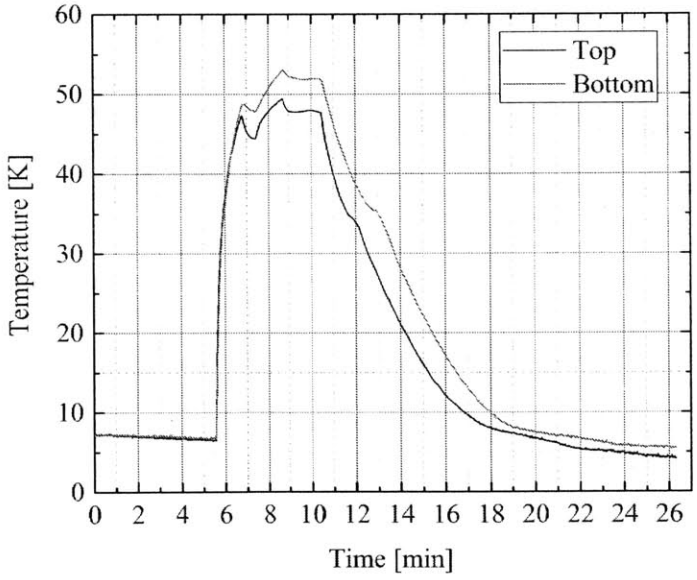

Figure 5-14: Temperature vs. time plots of PCS open/close operation in SN2 at 7 K, with 8 W additional cooling power.

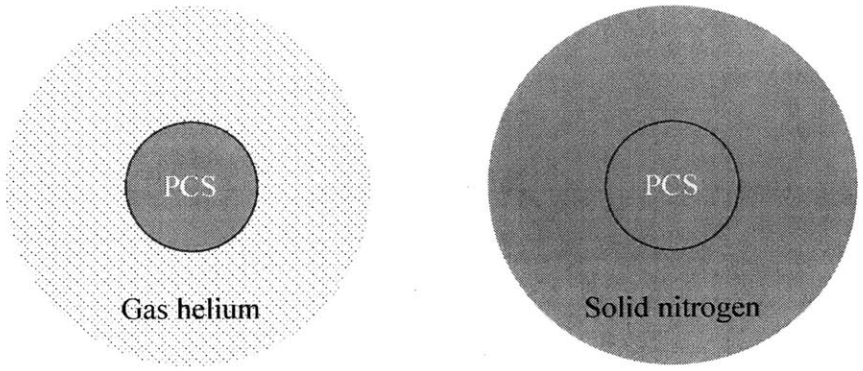

Figure 5-15: Left: helium vapor surrounding a heated PCS constantly replenished with cold helium vapor; right: SN2 surrounding a heated PCS.

5.6.2 Field Homogeneity During Charge Operation

As discussed in Section 2.5, the currents in all coils should remain constant during charging operation, and closing of the PCS's should not affect the current in each coil. Axial field mapping data could be used to infer the magnet current distribution.

Figure 5-16 shows three sets of axial field mapping results, at 10 A, of the magnet: 1) in driven mode while each PCS was fully open; 2) in driven mode while each PCS was closed; and 3) in persistent mode. A total of 25 points were mapped, axially 20-mm apart from each other. The field data agree very well, proving that the current did not change during the entire charging operation.

5.6.3 Winding Geometry Error

As shown in Figure 5-17, a measured field profile slightly deviated from the designed profile. Since the measured field in Figure 5-17 was with the magnet in driven mode, the current must be the same in all coils. This implies that the observed field deviation must have been caused by deviations in the winding parameters, i.e., dimensions, precise location of each turn.

Assuming I wound each coil accurately within its coil former, I concluded that the axial field deviation must have come from errors in the location of each coil when I assembled them to the magnet. The least squares method can be used to calculate the axial shifts by which I assembled each coil. The field at each of the 25 mapped

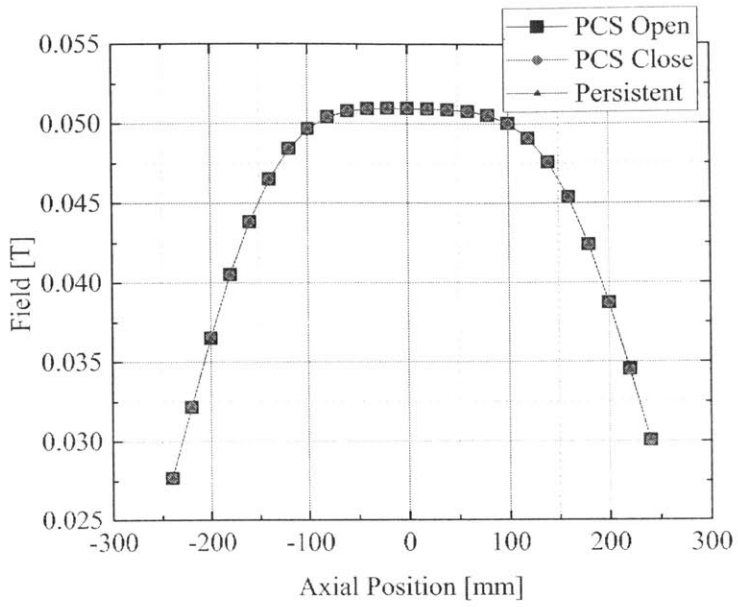

Figure 5-16: Three sets of axial field mapping results, at 10 A, of the magnet: 1) black squares, in driven mode with each PCS open; 2) red circles, in driven mode with each PCS close; and 3) blue triangles, in persistent mode.

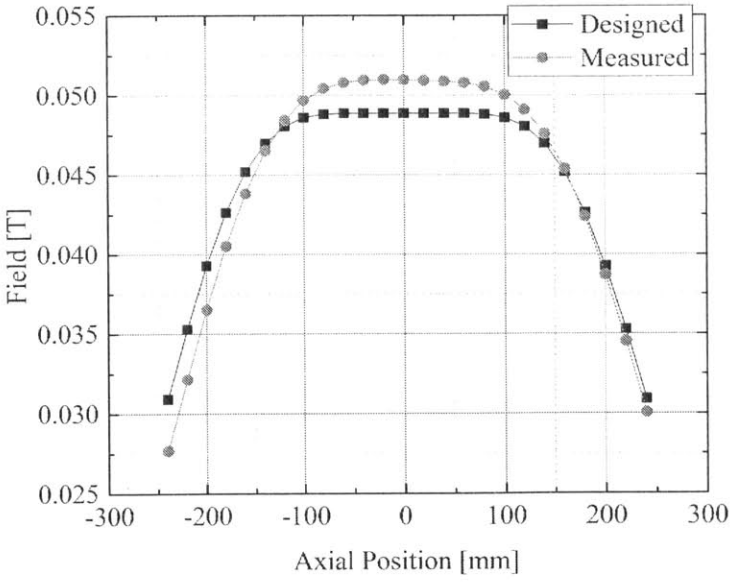

Figure 5-17: Measured axial field profile slightly deviated from designed profile.

points B_i was contributed from all 8 coils:

$$B_i = \sum_{j=1}^{8} b_{ij} \tag{5.6}$$

b_{ij} is the field generated by Coil j at point i. The field deviation at each point δB_i can be determined by

$$\delta B_i = \sum_{j=1}^{8} \delta b_{ij} = \sum_{j=1}^{8} \frac{\partial b_{ij}}{\partial x} \delta x_j \tag{5.7}$$

δB_i is the difference between measured and designed field values. $\partial b_{ij}/\partial x \equiv A_{ij}$ was calculated for each coil at each point. A_{ij}, together with a column of 1's, forms a 25 $\times$ 9 matrix. Detailed values of this matrix were summarized in Appendix B. Applying the general linear least squares method to solve for δx_j, the axial shift of coil j is governed by the following equation

$$\delta x_j = \left(\boldsymbol{A}^T \boldsymbol{A}\right)^{-1} \boldsymbol{A}^T B_i \tag{5.8}$$

To start with, the difference in field was calculated by subtracting the designed field values from the measured values. Applying Equation 5.8 with a calculated field gradient matrix $\boldsymbol{A}$, we can get a group of shifts of the 8 coils as summarized in Table 5.2. Here, Coil 1 through 8 label coils from top to bottom. The field generated by these shifted coils is much closer to the measured field, as shown in Figure 5-18.

In this regression, Coil 6 and Coil 7 have relatively large shifts, with which the calculated field gradients at the mapping points are no longer accurate. The same least squares method was iterated to improve the accuracy of results. To iterate, I calculated the field gradient matrix with the adjusted coil positions and the field differences between the measured and the calculated fields after the first regression. After two such iterations, the calculated axial field profile agrees the measured profile

Table 5.2: Coil Shifts After 1st Regression

Coil 1	Coil 2	Coil 3	Coil 4	Coil 5	Coil 6	Coil 7	Coil 8
-1.8 mm	-5.6 mm	-3.5 mm	4.4 mm	6.3 mm	16.7 mm	16.1 mm	9.8 mm

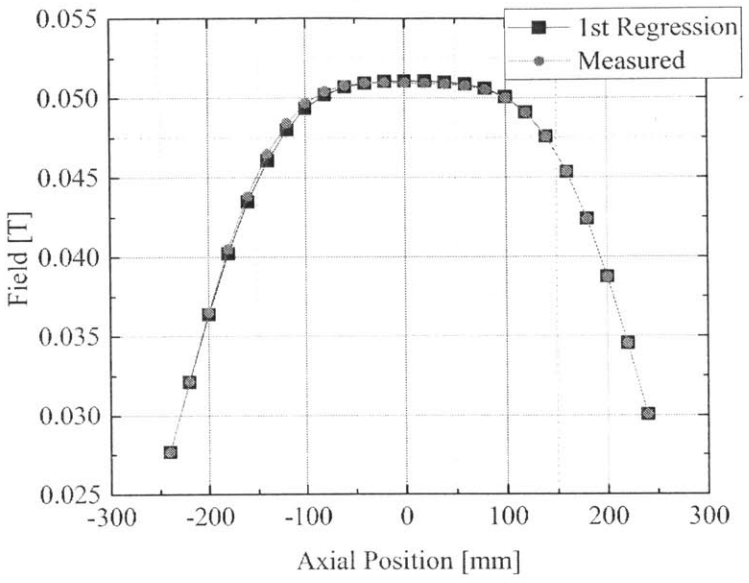

Figure 5-18: Axial field profiles, measured and after 1st regression.

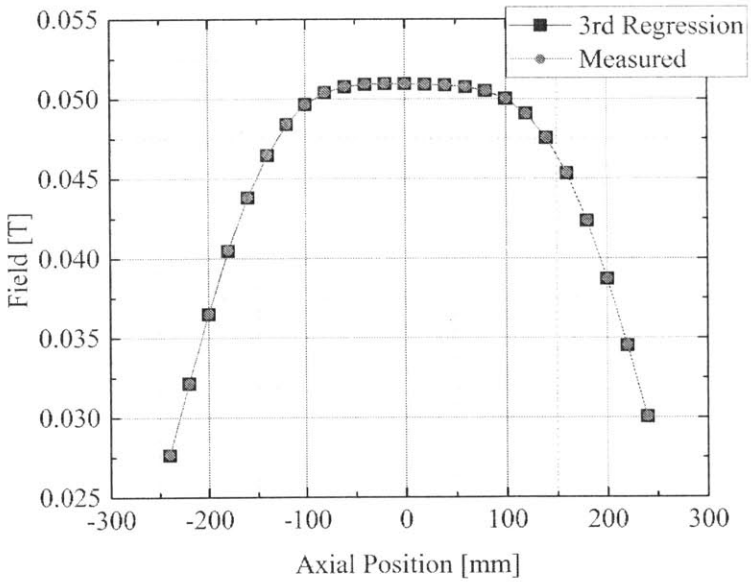

Figure 5-19: Axial field profiles, measured and after 3rd regression.

Table 5.3: Coil Shifts After 3rd Regression

Coil 1	Coil 2	Coil 3	Coil 4	Coil 5	Coil 6	Coil 7	Coil 8
0.6 mm	-0.7 mm	0.8 mm	-0.2 mm	-0.2 mm	1.6 mm	-1.9 mm	2.0 mm

Table 5.4: Overall Coil Shifts

Coil 1	Coil 2	Coil 3	Coil 4	Coil 5	Coil 6	Coil 7	Coil 8
-1.8 mm	-6.1 mm	-3.1 mm	4.2 mm	5.4 mm	14.1 mm	17.1 mm	11.9 mm

very well. The coil shifts in the third regression, all <2 mm, are summarized in Table 5.3. The calculated axial field profile after three regressions is plotted with the measured profile in Figure 5-19. The total coil shifts from original positions are summarized in Table 5.4.

Some of the shift values are too large to be true. This is because I only considered the axial shifts of the coils and neglected other possible variables, such as thickness and width of each coil and location of each turn. In order to simplify the regression operation, I chose the most significant variable, axial shift, as the only variable in Equation 5.7. Although, in this way, the regressions do not give the exact winding geometries, this simplification that gives an "equivalent" axial shift of each coil has proven to be useful. After the axial coil displacements are identified, they can be minimized by placing shims in between adjacent coils.

5.6.4 Persistent-Mode Operation

The magnet was operated in persistent mode in the temperature range 10-15 K, and it was able to sustain a persistent center field of >0.47 T up to 15 K.

The magnet was first energized to 70 A at 13 K. It was able to sustain a persistent field of 0.35 T for 5 days. Its center field, as shown in Figure 5-20, fluctuated around 0.3508 T during a period of 120 hours (5 days). However, the field trace does not suggest any discernible field decay. In addition, the axial field distribution mapped on the 1st day matched that on the 7th day, reconfirming no decay along the entire axis. These results demonstrate that the magnet can sustain a persistent center field of 0.35 T at 13 K. Over this 120-hour period, the maximum and minimum measured

fields were 0.35085 T and 0.35070 T respectively, which indicated a field decay, if there was any, could be no larger than 3.5 ppm/hour.

The magnet was further energized to 100 A at 9 K. After an initial field decay when temperature rose (Figure 5-22), as shown in Figure 5-23 the magnet was able to keep a persistent center field of 0.47 T at 13 K. As the temperature further rose, the magnet was able to maintain a slightly lower persistent field of 0.468 T from 11-14 K, as shown in Figure 5-24.

The axial field profile, at 9 K, initially similar to a 70-A persistent-mode profile, got distorted at higher temperatures. Figure 5-25 shows the field profiles at 9 K and then at 13 K, and again, after 2 days, at 13 K and 14 K. Even though the field profile got distorted during 2 days at 13 K, the field remained persistent and the distorted profile stayed unchanged, as demonstrated in Figure 5-26.

The axial field profile became distorted, because, I believe, each coil settled to its own persistent current level, different from those of the rest, i.e., at higher temperatures, a diverse performance among the coils became more distinct. The least squares method was employed to inversely calculate the current in each coil from the field profile. The field at each mapped point B_i can be summed from the contributions from the 8 coils:

$$B_i = \sum_{j=1}^{8} C_{ij} I_j \tag{5.9}$$

where C_{ij} is the field generated at point i from Coil j at 1 A, I_j is the actual current in Coil j. C_{ij} is a 25×9 matrix, with a column filled by 1's. The detailed values of this matrix is described in Appendix C. Using a measured field profile (Figure 5-26) and applying the least squares method, I obtained the current in each coil.

$$I_j = \left(\boldsymbol{C}^T \boldsymbol{C}\right)^{-1} \boldsymbol{C}^T B_i \tag{5.10}$$

The results are summarized in Table 5.5.

With this current distribution, the calculated axial field profile perfectly matches the measured profile, as shown in Figure 5-27. And this current distribution indicates that Coil 1 is the worst, and Coils 3, 4, 7 and 8 are better performers. The same

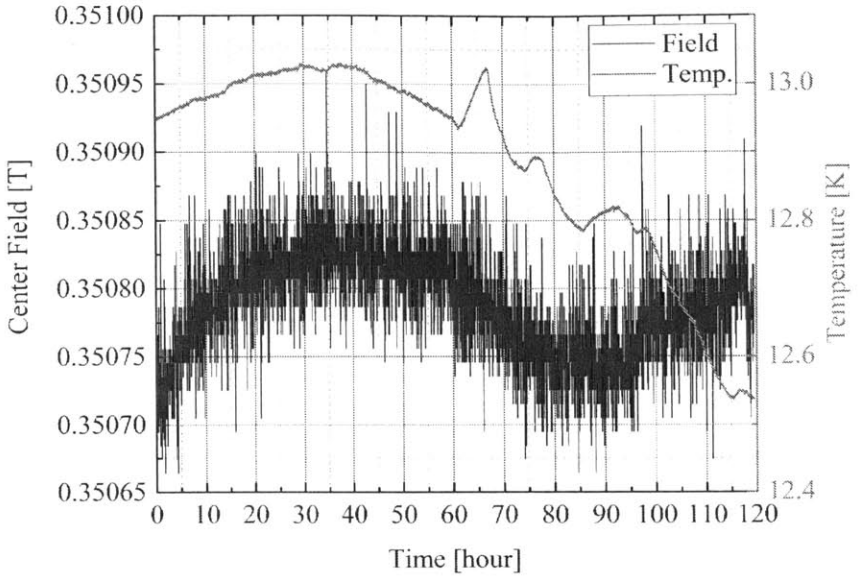

Figure 5-20: Center field and temperature vs. time plots at 70 A.

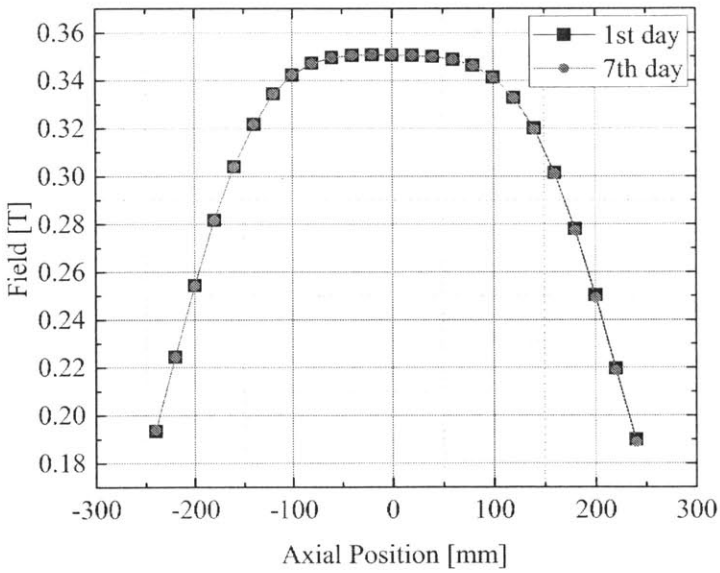

Figure 5-21: Axial field profiles mapped on 1st and 7th days while a center field of 0.35 T remained persistent.

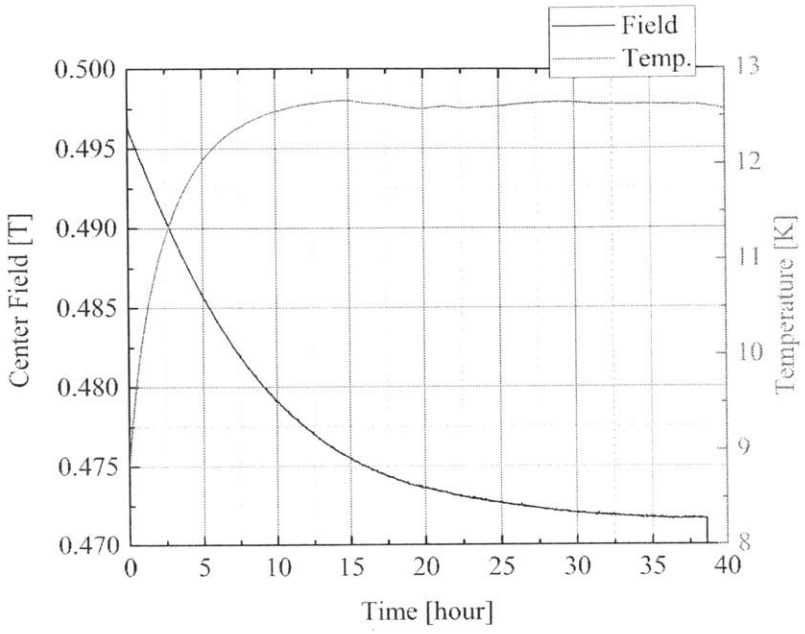

Figure 5-22: Center field and temperature vs. time plots at nominal 100 A from 9-13 K.

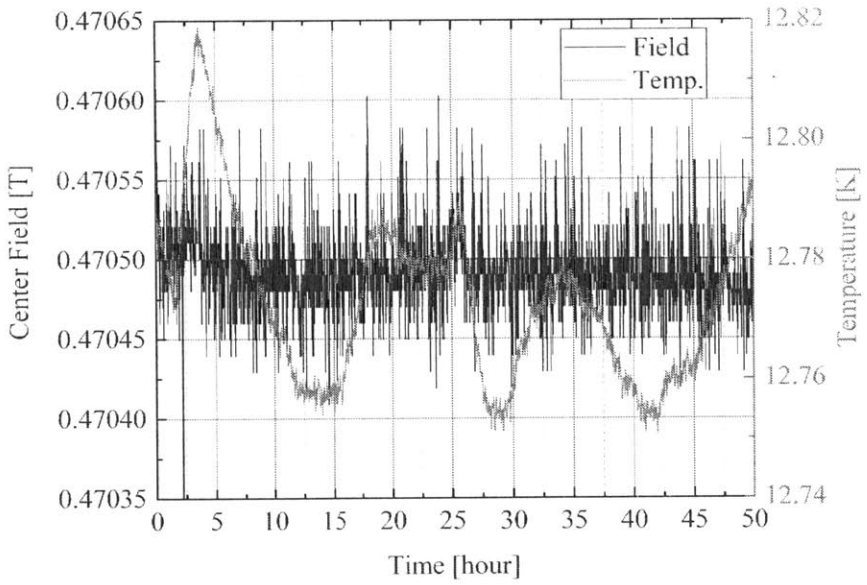

Figure 5-23: Center field and temperature vs. time plots in persistent mode at nominal 100 A at 13 K.

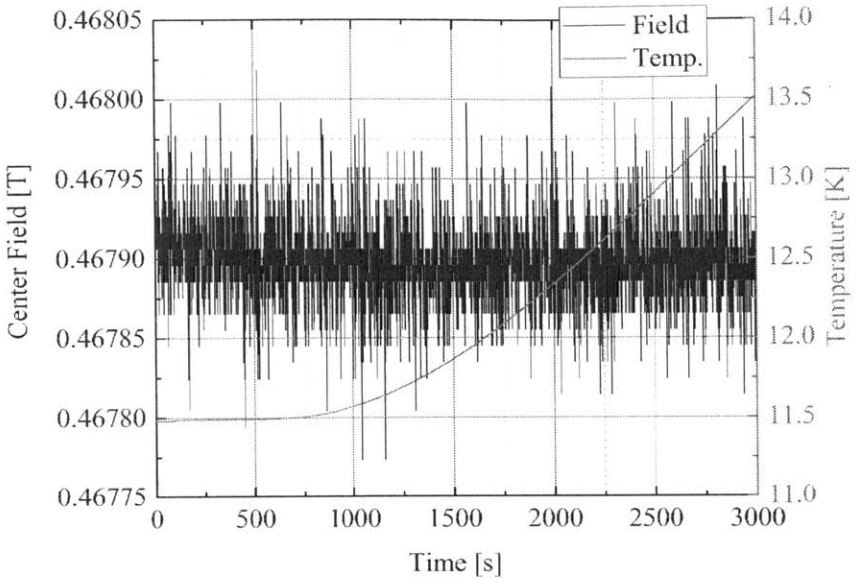

Figure 5-24: Center field and temperature vs. time plots in persistent mode at nominal 100 A from 11.5-14 K.

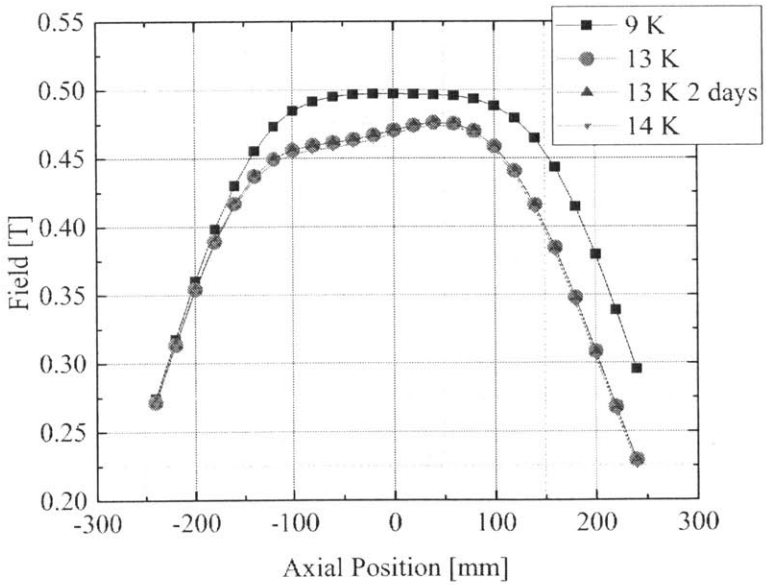

Figure 5-25: Axial 100-A persistent field profiles at 9 K, 13 K, and 14 K.

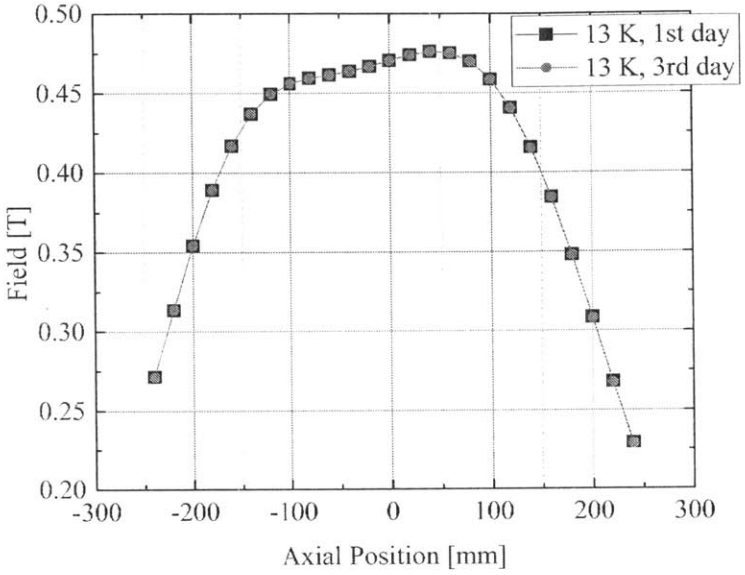

Figure 5-26: Axial persistent 0.47-T field profile at 13 K, mapped on the 1st (black squares) and 3rd days (red circles).

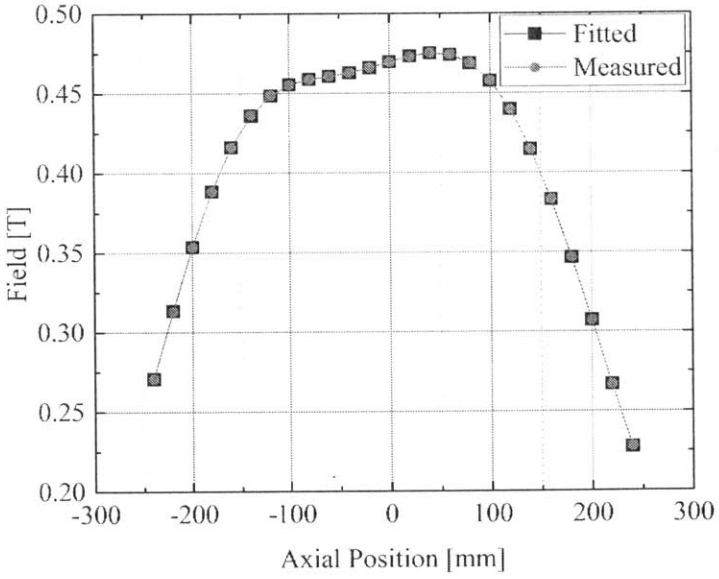

Figure 5-27: Axial field profiles: measured (red circles) and fitted (black squares).

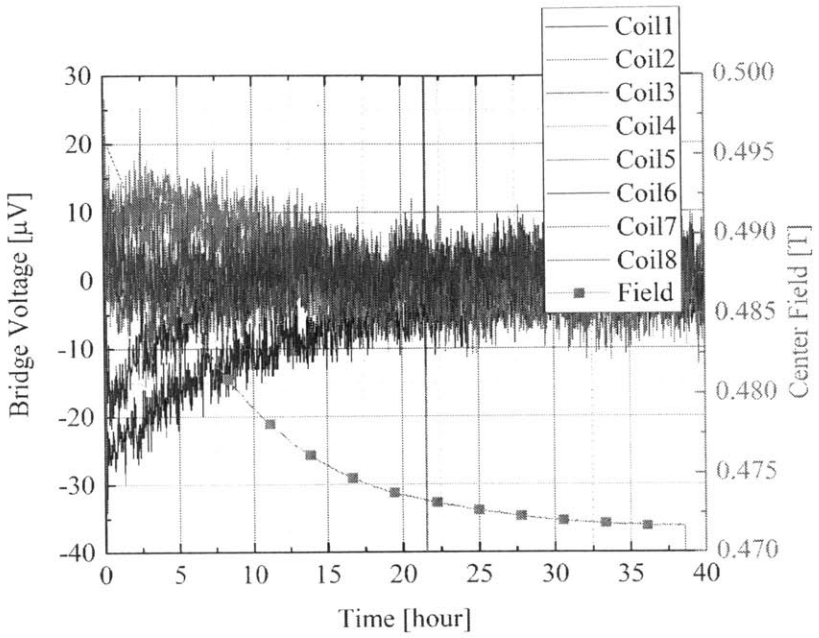

Figure 5-28: 8-coil bridge voltages and center field vs. time plots at nominal 100 A. Coils 1, 2, 5 and 6 show resistive voltages.

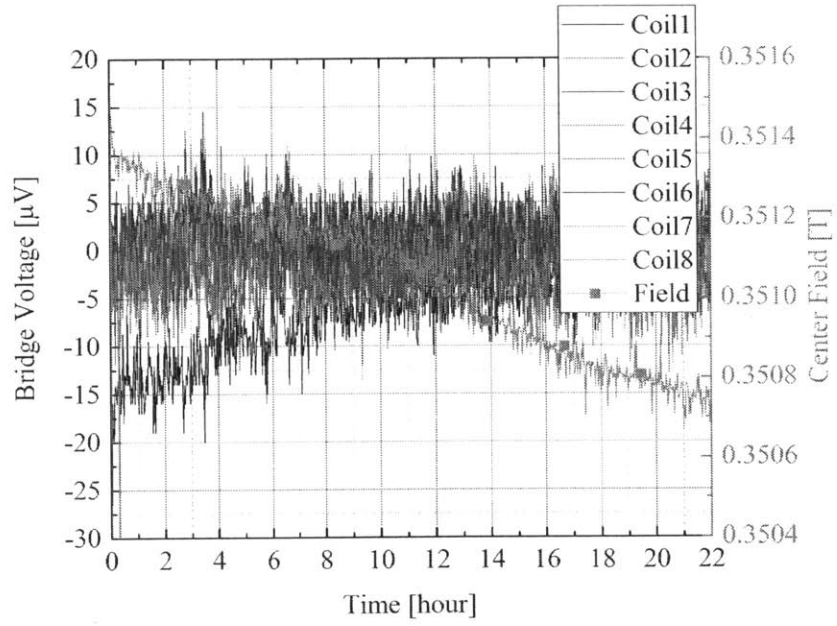

Figure 5-29: 8-coil bridge voltages and center field vs. time plots at nominal 70 A. Coil 1 shows a resistive voltage.

Table 5.5: Computed Current in Each Coil at 0.47 T

Coil 1	Coil 2	Coil 3	Coil 4	Coil 5	Coil 6	Coil 7	Coil 8
47.9 A	77.5 A	115.0 A	110.0 A	76.9 A	76.6 A	105.0 A	105.2 A

Table 5.6: Computed Current in Each Coil at 0.35 T

Coil 1	Coil 2	Coil 3	Coil 4	Coil 5	Coil 6	Coil 7	Coil 8
43.7 A	79.2 A	67.2 A	70.3 A	66.9 A	68.3 A	67.8 A	70.1 A

conclusion may be reached from voltage data analysis. Figure 5-28 shows the bridge voltages of the 8 coils while the field was decaying as the magnet temperature rose from 9 to 13 K. In the graph, Coils 1, 2, 5 and 6 show resistive voltages that undoubtedly caused the field to decay. In Coils 3, 4, 7 and 8 their bridge voltages remained zero. Agreement between the two methods proves that both axial shifts and current distribution analyses are valid.

Applying the same least squares method to the field profile at 70 A (Figure 5-21), the current in each coil was calculated and summarized in Table 5.6. Coil 1 had a calculated current of 43.7 A, the lowest among all coils. These current results match the bridge voltage data (Figure 5-29), and agreement verifies the inverse current analysis applied to 0.47-T field profile.

5.6.5 Protection

Each PCS serves also as the energy absorber of the magnet. Its protection function was tested with the PCS immersed in solid nitrogen. With the magnet in persistent mode at 100 A, all PCS heaters were manually activated, triggering a dump. The temperature of each PCS is plotted in Figure 5-30. During the dump, each PCS remained below 70 K.

Figure 5-31 shows the center field and 8 PCS temperature traces recorded at the beginning phase of a manually activated dump. This exercise was to verify that a PCS in each coil can absorb the magnet energy and thereby protect the magnet in case of a real quench. Note that at $t = 24$ s, after 3 seconds of the PCS heaters activation, the field started to decay.

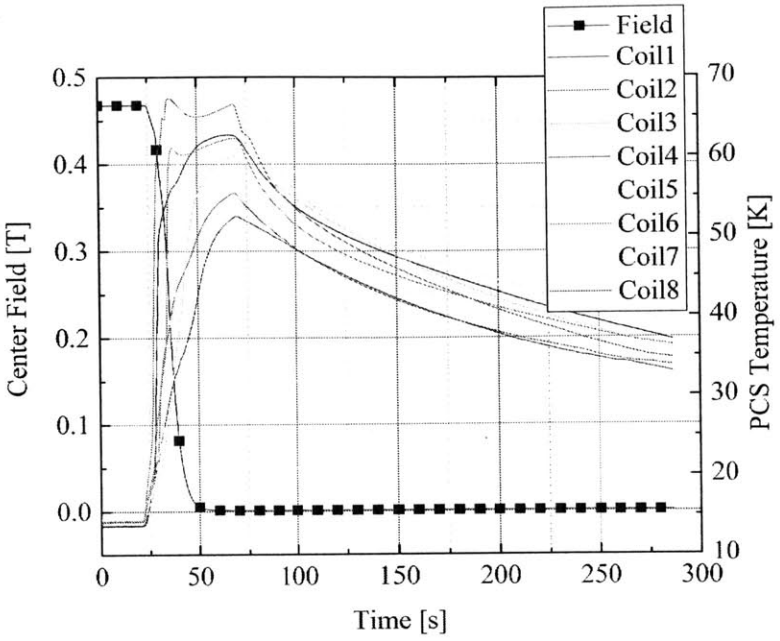

Figure 5-30: Center field and 8-PCS temperatures vs. time plots of a complete manually-activated dump.

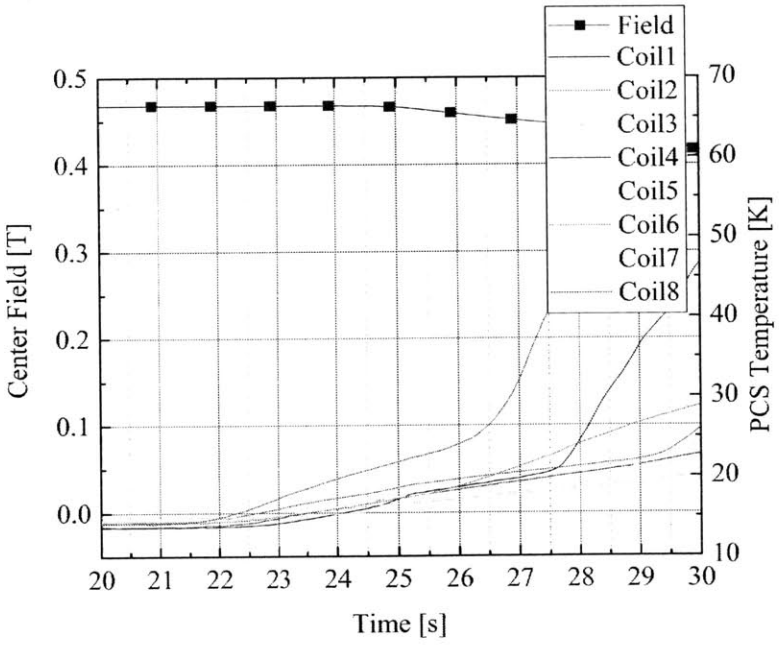

Figure 5-31: Center field and 8-PCS temperatures vs. time plots at the beginning phase of a manually-activated dump.

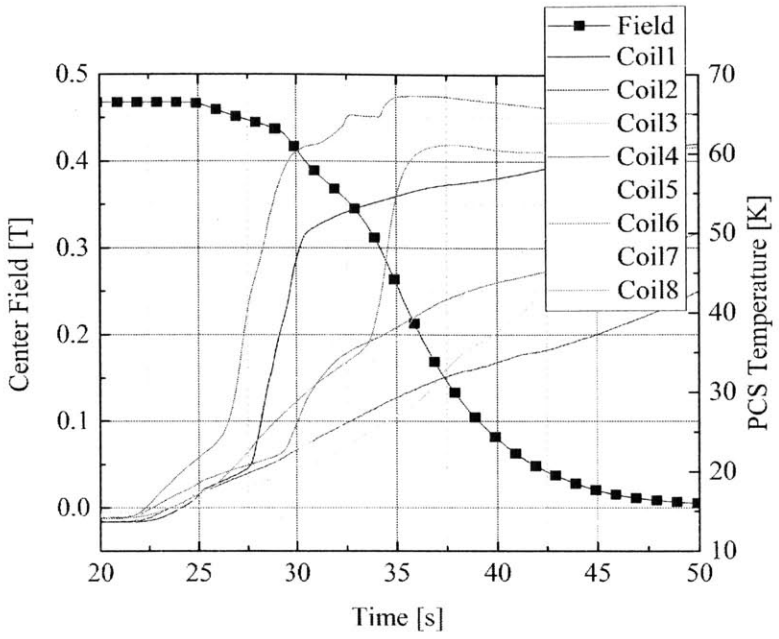

Figure 5-32: Center field and 8-PCS temperatures vs. time plots during the first 50 s of a manually-activated dump.

Figure 5-32 shows plots of the same dump to $t = 50$ s. In 10 seconds, the field decayed to half of its initial value, and in 25 seconds the field almost decayed entirely.

5.6.6 Screening Current Field

The magnet was wound with monofilament ($\sim\Phi$0.4 mm) MgB_2 wire, one important consequence of which is a magnetization much greater than that of multifilamentary NbTi used in MRI magnets now in marketplace. Magnetization manifests as a screening-current field (SCF), degrading the spatial field homogeneity of a magnet. Because a SCF is still much smaller than the main magnet field thus difficult to accurately detect, the remnant field, which is a residual field after the magnet is energized and then de-energized, was measured and used to estimate the order of magnitude of SCF.

The axial field was mapped after the magnet had been dumped from 100-A persistent-mode operation, as shown in Figure 5-33. The remnant field was not homogeneous along the axis. Its peak value was -0.09 mT, $\sim$200 ppm of the center field

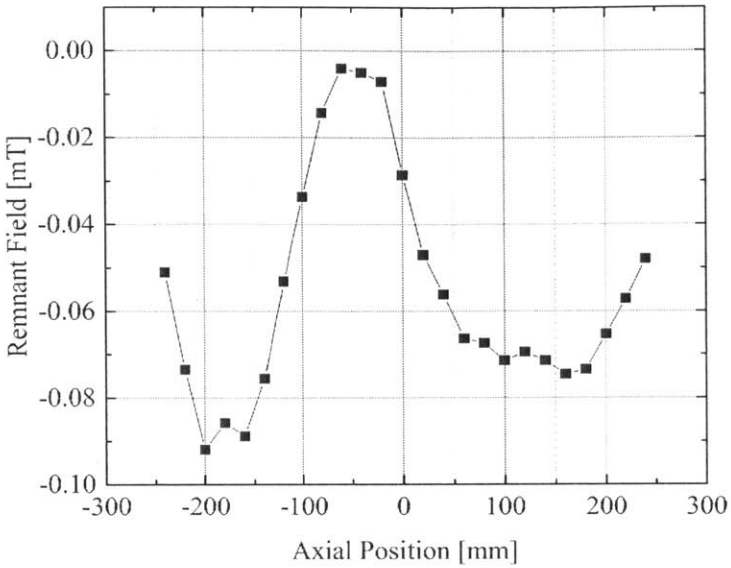

Figure 5-33: Axial remnant field profile after a dump from persistent-mode operation at 100 A.

at 100 A. This remnant field suggested an SCF, while the magnet is fully energized, about several hundreds of ppm of the center field. A ferro-shimming should be able to effectively deal with this field inhomogeneity.

Chapter 6

Conclusions

Persistent-mode operation was successfully achieved with this MgB_2 magnet composed 8 separate coil modules, each with its own PCS and terminated with a superconducting joint. The success may well lead MgB_2 as a viable rival to NbTi.

Although I have already demonstrated that flux jumping in monofilament MgB_2 wire is not a design/operation issue [28,34], the error field induced by screening current field will be significantly greater than that of <50-μm NbTi filaments. Still, ferro-shimming, though more powerful would be required, should be able to cope with this challenge. Clearly a splicing technique for multiilamentary MgB_2 successfully developed at MIT back in 2008 [25] needs to be further refined to make it more reliable so that with multifilamentary MgB_2 wire screening current field becomes a non-issue.

Because of the splicing technique, as well as the brittleness of MgB_2 wire, wind-and-react procedure, well established with Nb_3Sn magnets, may be necessary for MgB_2 magnets. The cost and work associated with reaction in this magnet were manageable. Nevertheless, at MIT, we are also developing a splicing technique for reacted MgB_2 monofilament wires.

The idea of modularization works well with wind-and-react procedure; it makes the reaction easier and confines the damage to a single coil if anything bad happens. In this magnet, because 1 coil turned out to be bad, our modular approach was proven a useful production method.

In the absence of liquid helium, solid nitrogen considerably enhances the thermal capacity of a cold mass, providing good thermal stability to the magnet. Solid nitrogen also maintained a uniform temperature environment around the magnet. However, a large thermal contraction of solid nitrogen may cause damage to mechanically vulnerable parts of the magnet, necessitating these parts be protected. A PCS may open and close slower in solid nitrogen than in helium, thus it is better to be placed outside solid nitrogen or close to a cooling source.

The completion of this MgB_2 magnet project at the MIT Francis Bitter Magnet Lab may be considered as a major milestone in the MgB_2 MRI magnet technology. It has proven that MgB_2 is a promising option especially for the next generation liquid-helium-free MRI magnet system. It is expected to promote further R&D work in this technology, and ultimately to proliferation of the MgB_2 MRI magnet in the near future.

Appendix A

Inductance Matrix

The values of self and mutual inductances between each pair of coils are summarized in Inductance Matrix $\boldsymbol{M}$ [2].

$$[\boldsymbol{M}] = \begin{bmatrix} M_{11} & M_{12} & M_{13} & M_{14} & M_{15} & M_{16} & M_{17} & M_{18} \\ M_{21} & M_{22} & M_{23} & M_{24} & M_{25} & M_{26} & M_{27} & M_{28} \\ M_{31} & M_{32} & M_{33} & M_{34} & M_{35} & M_{36} & M_{37} & M_{38} \\ M_{41} & M_{42} & M_{43} & M_{44} & M_{45} & M_{46} & M_{47} & M_{48} \\ M_{51} & M_{52} & M_{53} & M_{54} & M_{55} & M_{56} & M_{57} & M_{58} \\ M_{61} & M_{62} & M_{63} & M_{64} & M_{65} & M_{66} & M_{67} & M_{68} \\ M_{71} & M_{72} & M_{73} & M_{74} & M_{75} & M_{76} & M_{77} & M_{78} \\ M_{81} & M_{82} & M_{83} & M_{84} & M_{85} & M_{86} & M_{87} & M_{88} \end{bmatrix} \quad (A.1)$$

$$= \begin{bmatrix} 40.6 & 14.1 & 13.4 & 6.19 & 6.86 & 3.53 & 4.10 & 2.27 \\ 14.1 & 40.6 & 6.19 & 13.4 & 3.53 & 6.86 & 2.27 & 4.10 \\ 13.4 & 6.19 & 44.5 & 3.21 & 18.7 & 19.8 & 9.49 & 1.35 \\ 6.19 & 13.4 & 3.21 & 44.5 & 1.98 & 18.7 & 1.35 & 9.49 \\ 6.86 & 3.53 & 18.7 & 1.98 & 40.6 & 1.27 & 18.0 & .898 \\ 3.53 & 6.86 & 1.98 & 18.7 & 1.27 & 40.6 & .898 & 18.0 \\ 4.10 & 2.27 & 9.49 & 1.35 & 18.0 & .898 & 40.6 & .655 \\ 2.27 & 4.10 & 1.35 & 9.49 & .898 & 18.0 & .655 & 40.6 \end{bmatrix} \text{ mH}$$

Here, M_{ii} is the self inductance of Coil i, M_{ij} is the mutual inductance between Coils i and j. Coil 1 to 8 are labeled as shown in Figure 2-2.

Appendix B

Field Gradient Matrix

The field gradient matrix $\boldsymbol{A}$ used in the inverse calculation of axial coil positions includes one column of 1's and 8 columns of $\partial b_{ij}/\partial x$, forming a 25×9 matrix. The matrices used in the first, second and third regressions are listed in Tables B.1, B.2 and B.3, respectively.

Table B.1: Field Gradient Matrix I

1	4.70E-06	7.60E-06	5.60E-06	2.30E-06	1.10E-06	5.00E-07	4.00E-07	2.00E-07
1	1.50E-06	7.40E-06	6.70E-06	2.90E-06	1.30E-06	6.00E-07	4.00E-07	2.00E-07
1	-2.20E-06	6.10E-06	7.60E-06	3.60E-06	1.60E-06	8.00E-07	4.00E-07	3.00E-07
1	-5.20E-06	3.30E-06	8.00E-06	4.60E-06	2.10E-06	9.00E-07	6.00E-07	3.00E-07
1	-7.10E-06	-2.00E-07	7.30E-06	5.60E-06	2.70E-06	1.20E-06	7.00E-07	4.00E-07
1	-7.60E-06	-3.70E-06	5.40E-06	6.70E-06	3.40E-06	1.50E-06	8.00E-07	5.00E-07
1	-7.20E-06	-6.20E-06	2.00E-06	7.40E-06	4.20E-06	1.90E-06	1.00E-06	6.00E-07
1	-6.40E-06	-7.40E-06	-1.70E-06	7.60E-06	5.20E-06	2.40E-06	1.30E-06	7.00E-07
1	-5.30E-06	-7.50E-06	-5.10E-06	6.60E-06	6.20E-06	3.00E-06	1.60E-06	9.00E-07
1	-4.30E-06	-6.80E-06	-7.30E-06	4.40E-06	7.10E-06	3.70E-06	2.00E-06	1.10E-06
1	-3.40E-06	-5.80E-06	-8.00E-06	1.10E-06	7.60E-06	4.60E-06	2.40E-06	1.40E-06
1	-2.70E-06	-4.80E-06	-7.80E-06	-2.60E-06	7.20E-06	5.80E-06	3.10E-06	1.70E-06
1	-2.10E-06	-3.90E-06	-6.90E-06	-5.50E-06	5.50E-06	6.90E-06	3.90E-06	2.10E-06
1	-1.70E-06	-3.10E-06	-5.80E-06	-7.20E-06	2.60E-06	7.80E-06	4.80E-06	2.70E-06
1	-1.40E-06	-2.40E-06	-4.60E-06	-7.60E-06	-1.10E-06	8.00E-06	5.80E-06	3.40E-06
1	-1.10E-06	-2.00E-06	-3.70E-06	-7.10E-06	-4.40E-06	7.30E-06	6.80E-06	4.30E-06
1	-9.00E-07	-1.60E-06	-3.00E-06	-6.20E-06	-6.60E-06	5.10E-06	7.50E-06	5.30E-06
1	-7.00E-07	-1.30E-06	-2.40E-06	-5.20E-06	-7.60E-06	1.70E-06	7.40E-06	6.40E-06
1	-6.00E-07	-1.00E-06	-1.90E-06	-4.20E-06	-7.40E-06	-2.00E-06	6.20E-06	7.20E-06
1	-5.00E-07	-8.00E-07	-1.50E-06	-3.40E-06	-6.70E-06	-5.40E-06	3.70E-06	7.60E-06
1	-4.00E-07	-7.00E-07	-1.20E-06	-2.70E-06	-5.60E-06	-7.30E-06	2.00E-07	7.10E-06
1	-3.00E-07	-6.00E-07	-9.00E-07	-2.10E-06	-4.60E-06	-8.00E-06	-3.30E-06	5.20E-06
1	-3.00E-07	-4.00E-07	-8.00E-07	-1.60E-06	-3.60E-06	-7.60E-06	-6.10E-06	2.20E-06
1	-2.00E-07	-4.00E-07	-6.00E-07	-1.30E-06	-2.90E-06	-6.70E-06	-7.40E-06	-1.50E-06
1	-2.00E-07	-4.00E-07	-5.00E-07	-1.10E-06	-2.30E-06	-5.60E-06	-7.60E-06	-4.70E-06

Table B.2: Field Gradient Matrix II

1	5.00E-06	7.50E-06	5.50E-06	2.40E-06	1.20E-06	6.00E-07	4.00E-07	3.00E-07
1	1.80E-06	7.60E-06	6.60E-06	3.10E-06	1.50E-06	8.00E-07	4.00E-07	3.00E-07
1	-1.80E-06	6.50E-06	7.60E-06	3.80E-06	1.90E-06	9.00E-07	5.00E-07	3.00E-07
1	-5.00E-06	4.20E-06	8.00E-06	4.80E-06	2.30E-06	1.20E-06	7.00E-07	4.00E-07
1	-7.00E-06	9.00E-07	7.60E-06	5.80E-06	2.90E-06	1.40E-06	8.00E-07	4.00E-07
1	-7.60E-06	-2.80E-06	5.90E-06	6.80E-06	3.70E-06	1.80E-06	1.00E-06	6.00E-07
1	-7.30E-06	-5.70E-06	2.70E-06	7.60E-06	4.50E-06	2.30E-06	1.20E-06	6.00E-07
1	-6.40E-06	-7.30E-06	-1.00E-06	7.50E-06	5.60E-06	2.90E-06	1.50E-06	6.00E-07
1	-5.40E-06	-7.60E-06	-4.50E-06	6.30E-06	6.60E-06	3.70E-06	1.90E-06	1.00E-06
1	-4.40E-06	-7.10E-06	-7.00E-06	3.80E-06	7.40E-06	4.50E-06	2.40E-06	1.20E-06
1	-3.50E-06	-6.20E-06	-8.00E-06	3.00E-07	7.60E-06	5.60E-06	3.00E-06	1.60E-06
1	-2.80E-06	-5.10E-06	-7.90E-06	-3.20E-06	6.70E-06	6.70E-06	3.80E-06	2.00E-06
1	-2.20E-06	-4.20E-06	-7.10E-06	-5.90E-06	4.50E-06	7.60E-06	4.60E-06	2.40E-06
1	-1.80E-06	-3.30E-06	-6.00E-06	-7.40E-06	1.20E-06	8.00E-06	5.80E-06	3.10E-06
1	-1.40E-06	-2.60E-06	-4.90E-06	-7.60E-06	-2.40E-06	7.40E-06	6.80E-06	3.90E-06
1	-1.20E-06	-2.10E-06	-3.90E-06	7.00E-06	-5.40E-06	5.40E-06	7.50E-06	4.90E-06
1	-9.00E-07	-1.70E-06	-3.10E-06	-6.00E-06	-7.10E-06	2.10E-06	7.50E-06	5.90E-06
1	-7.00E-07	-1.30E-06	-2.50E-06	-4.90E-06	-7.70E-06	-1.70E-06	6.50E-06	6.90E-06
1	-6.00E-07	-1.10E-06	-1.90E-06	-4.00E-06	-7.20E-06	-5.00E-06	4.10E-06	7.50E-06
1	-5.00E-07	-9.00E-07	-1.60E-06	-3.20E-06	-6.20E-06	-7.20E-06	8.00E-07	7.50E-06
1	-4.00E-07	-7.00E-07	-1.30E-06	-2.50E-06	-5.30E-06	-8.00E-06	-2.90E-06	6.20E-06
1	-3.00E-07	-5.00E-07	-1.00E-06	-2.00E-06	-4.20E-06	-7.80E-06	-5.70E-06	3.70E-06
1	-3.00E-07	-4.00E-07	-8.00E-07	-1.60E-06	-3.30E-06	-6.90E-06	-7.30E-06	2.00E-07
1	-3.00E-07	-4.00E-07	-7.00E-07	-1.30E-06	-2.70E-06	-5.80E-06	-7.60E-06	-3.40E-06
1	-2.00E-07	-4.00E-07	-5.00E-07	-1.00E-06	-2.10E-06	-4.70E-06	-7.00E-06	6.00E-06

Table B.3: Field Gradient Matrix III

1	5.00E-06	7.50E-06	5.50E-06	2.40E-06	1.20E-06	6.00E-07	4.00E-07	2.00E-07
1	1.90E-06	7.60E-06	6.50E-06	3.10E-06	1.40E-06	7.00E-07	4.00E-07	3.00E-07
1	-1.80E-06	6.50E-06	7.50E-06	3.80E-06	1.80E-06	9.00E-07	6.00E-07	3.00E-07
1	-4.90E-06	4.20E-06	8.00E-06	4.80E-06	2.30E-06	1.10E-06	7.00E-07	3.00E-07
1	-6.90E-06	8.00E-07	7.60E-06	5.80E-06	2.90E-06	1.30E-06	8.00E-07	5.00E-07
1	-7.70E-06	-2.80E-06	5.80E-06	6.80E-06	3.70E-06	1.70E-06	1.00E-06	5.00E-07
1	-7.30E-06	-5.60E-06	2.80E-06	7.60E-06	4.50E-06	2.10E-06	1.30E-06	7.00E-07
1	-6.50E-06	-7.20E-06	-1.00E-06	7.50E-06	5.50E-06	2.80E-06	1.60E-06	8.00E-07
1	-5.40E-06	-7.60E-06	-4.50E-06	6.30E-06	6.50E-06	3.50E-06	2.00E-06	1.00E-06
1	-4.40E-06	-7.10E-06	-7.00E-06	3.80E-06	7.40E-06	4.40E-06	2.40E-06	1.30E-06
1	-3.50E-06	-6.20E-06	-8.00E-06	3.00E-07	7.60E-06	5.40E-06	3.10E-06	1.50E-06
1	-2.80E-06	-5.10E-06	-7.80E-06	-3.20E-06	6.80E-06	6.50E-06	3.90E-06	2.00E-06
1	-2.20E-06	-4.10E-06	-7.10E-06	-5.90E-06	4.60E-06	7.50E-06	4.80E-06	2.50E-06
1	-1.70E-06	-3.30E-06	-6.00E-06	-7.40E-06	1.30E-06	8.00E-06	5.80E-06	3.10E-06
1	-1.40E-06	-2.70E-06	-4.90E-06	-7.60E-06	-2.30E-06	7.60E-06	6.80E-06	3.90E-06
1	-1.10E-06	-2.10E-06	-3.90E-06	-7.00E-06	-5.30E-06	5.90E-06	7.50E-06	4.80E-06
1	-9.00E-07	-1.70E-06	-3.10E-06	-6.00E-06	-7.10E-06	2.90E-06	7.40E-06	5.90E-06
1	-8.00E-07	-1.30E-06	-2.40E-06	-4.90E-06	-7.60E-06	-9.00E-07	6.20E-06	6.90E-06
1	-6.00E-07	-1.10E-06	-2.00E-06	-4.00E-06	-7.20E-06	-4.40E-06	3.70E-06	7.50E-06
1	-5.00E-07	-9.00E-07	-1.60E-06	-3.20E-06	-6.30E-06	-6.90E-06	2.00E-07	7.50E-06
1	-4.00E-07	-7.00E-07	-1.20E-06	-2.50E-06	-5.20E-06	-8.00E-06	-3.30E-06	6.20E-06
1	-3.00E-07	-6.00E-07	-1.00E-06	-2.00E-06	-4.30E-06	-7.80E-06	-6.10E-06	3.70E-06
1	-3.00E-07	-4.00E-07	-8.00E-07	-1.60E-06	-3.40E-06	-7.00E-06	-7.40E-06	2.00E-07
1	-2.00E-07	-4.00E-07	-7.00E-07	-1.30E-06	-2.70E-06	-6.00E-06	-7.60E-06	-3.30E-06
1	-2.00E-07	-3.00E-07	-6.00E-07	-1.00E-06	-2.10E-06	-4.90E-06	-6.90E-06	-6.00E-06

Appendix C

Field Generation Matrix

The field generation matrix $\boldsymbol{C}$ used in the inverse calculation of coil currents includes one column of 1's and 8 columns of field constant C_{ij}, forming a 25×9 matrix. The matrix used in the regression is listed in Table C.1.

Table C.1: Field Generation Matrix

1	0.00119	8.03E-04	5.18E-04	2.42E-04	1.31E-04	8.03E-05	5.33E-05	3.69E-05
1	0.00126	9.54E-04	6.38E-04	2.97E-04	1.57E-04	9.39E-05	6.13E-05	4.19E-05
1	0.00126	0.0011	7.79E-04	3.65E-04	1.89E-04	1.11E-04	7.10E-05	4.77E-05
1	0.00119	0.00121	9.36E-04	4.51E-04	2.29E-04	1.31E-04	8.28E-05	5.47E-05
1	0.00107	0.00127	0.00109	5.57E-04	2.80E-04	1.56E-04	9.71E-05	6.30E-05
1	9.23E-04	0.00125	0.00123	6.83E-04	3.44E-04	1.88E-04	1.15E-04	7.31E-05
1	7.72E-04	0.00117	0.00132	8.27E-04	4.25E-04	2.28E-04	1.36E-04	8.53E-05
1	6.34E-04	0.00104	0.00133	9.79E-04	5.25E-04	2.78E-04	1.63E-04	1.00E-04
1	5.15E-04	8.87E-04	0.00128	0.00112	6.45E-04	3.41E-04	1.97E-04	1.18E-04
1	4.17E-04	7.38E-04	0.00116	0.00122	7.85E-04	4.20E-04	2.40E-04	1.41E-04
1	3.38E-04	6.04E-04	0.00101	0.00127	9.36E-04	5.19E-04	2.94E-04	1.69E-04
1	2.75E-04	4.90E-04	8.48E-04	0.00124	0.00108	6.39E-04	3.61E-04	2.05E-04
1	2.25E-04	3.97E-04	6.99E-04	0.00115	0.0012	7.80E-04	4.46E-04	2.49E-04
1	1.86E-04	3.22E-04	5.69E-04	0.00101	0.00126	9.37E-04	5.51E-04	3.05E-04
1	1.54E-04	2.62E-04	4.61E-04	8.62E-04	0.00125	0.0011	6.76E-04	3.76E-04
1	1.29E-04	2.15E-04	3.73E-04	7.15E-04	0.00118	0.00123	8.19E-04	4.64E-04
1	1.09E-04	1.78E-04	3.03E-04	5.84E-04	0.00105	0.00132	9.71E-04	5.73E-04
1	9.22E-05	1.48E-04	2.48E-04	4.74E-04	9.05E-04	0.00133	0.00111	7.02E-04
1	7.88E-05	1.24E-04	2.04E-04	3.84E-04	7.56E-04	0.00128	0.00122	8.48E-04
1	6.78E-05	1.05E-04	1.69E-04	3.11E-04	6.19E-04	0.00116	0.00127	9.99E-04
1	5.86E-05	8.88E-05	1.41E-04	2.54E-04	5.03E-04	0.00101	0.00124	0.00114
1	5.10E-05	7.60E-05	1.19E-04	2.08E-04	4.07E-04	8.47E-04	0.00115	0.00123
1	4.47E-05	6.55E-05	1.01E-04	1.72E-04	3.30E-04	6.97E-04	0.00102	0.00127
1	3.93E-05	5.67E-05	8.60E-05	1.43E-04	2.69E-04	5.68E-04	8.70E-04	0.00123
1	3.47E-05	4.94E-05	7.38E-05	1.20E-04	2.20E-04	4.60E-04	7.23E-04	0.00113

Bibliography

[1] Yukikazu Iwasa. *Case Studies in Superconducting Magnets - Design and Operational Issues.* Springer, 2nd edition, 2009.

[2] Seungyong Hahn. Electromagnetic design of MgB_2 magnet. Personal communication.

[3] marketsandmarkets.com. Advances in magnetic resonance imaging (mri) market (2013-2018) - technology trend analysis – by architecture, field strengths, technology & applications in medical diagnostics with market landscape analysis – estimates up to 2018. *marketsandmarkets.com*, 2013.

[4] J. K. Hulm and B. T. Matthias. Overview of superconducting materials development. In S. Foner and B. B. Schwartz, editors, *Superconductor Materials Science–Metallurgy, Fabrication, and Applications.* Plenum Press, New York, 1981.

[5] Y. Lvovsky and P. Jarvis. Superconducting systems for mri—present solutions and new trends. *IEEE Trans Appl. Supercond.*, 15(2):1317–1325, June 2005.

[6] Da He, Hao Yu, and Yingyao Chen. Equity in the distribution of ct and mri in china: a panel analysis. *Int J Equity Health*, 12(39), 2013.

[7] Atlas of MS. Atlas of ms database - number of mri machines globally 2013.

[8] Centers for Disease Control and Prevention. Number of magnetic resonance imaging (mri) units and computed tomography (ct) scanners: Selected countries, selected years 1990–2009.

[9] Health PEI. Magnetic resonance imaging (mri) scan wait times.

[10] Philip Ward. French mri waiting times are 'worst in a decade'.

[11] J. G. Bendnorz and K. A. Müller. Possible high tc superconductivity in the ba-la-cu-o system. *Zeitschrift Für Physik B - Condensed Matter*, 64(2):189–193, 1986.

[12] Hiroshi Maeda, Yoshiaki Tanaka, Masao Fukutomi, and Toshihisa Asano. A new high-tc oxide superconductor without a rare-earth element. *Japanese Journal of Applied Physics Part 2-Letters*, 27(2):L209–L210, 1988.

[13] M. K. Wu, J. R. Ashburn, C. J. Torng, P. H. Hor, R. L. Meng, L. Gao, Z. J. Huang, Y. Q. Wang, and C. W. Chu. Superconductivity at 93-k in a new mixed-phase y- ba-cu-o compound system at ambient pressure. *Physical Review Letters*, 58(9):908–910, 1987.

[14] J. Nagamatsu, N. Nakagawa, T. muranaka, Y. Zenitani, and J. Akimitsu. Superconductivity at 39 k in magnesium diboride. *Nature*, 410(6824):63–64, 2001.

[15] A. Stenvall, I. Hiltunen, A. Korpela, J. Lehtonen, R. Mikkonen, J. Viljamaa, and G. Grasso. A checklist for designers of cryogen-free mgb2 coils. *Supercond. Sci. Technol.*, 20:386–391, 2007.

[16] D. Zhang, Z. K. Wang, S. T. Dai, J. Y. Zhang, N. H. Song, X. H. Li, F. Y. Zhang, X. J. Du, M. Qiu, Z. F. Zhang, T.B.Huang, Z.Q.Zhu, X.Xu, W.W.Zhou, G.M.Zhang, L.Y.Xiao, and L.Z.Lin. Research on mgb2 superconducting magnet with iron core for mri. *IEEE Trans Appl. Supercond.*, 20(3):764–768, 2010.

[17] D. Zhang, S. T. Dai, Z. K. Wang, J. Y. Zhang, N. H. Song, X. H. Li, F. Y. Zhang, X. J. Du, M. Qiu, Z. F. Zhang, W. W. Zhou, G. M. Zhang, L. Y. Xiao, and L. Z. Lin. Research on stability of mgb2 superconducting magnet for mri. *IEEE Trans Appl. Supercond.*, 21(3):2100–2103, 2011.

[18] Xiao Hang Li, Xiao Ji Du, Qing Bao, Ling Qi Kong, Li Yang Ye, and Li Ye Xiao. Design, development and experiment of a 1.5 t MgB_2 superconducting test magnet. *Cryogenics*, 49:286–90, 2009.

[19] Xiaohang Li, Dong Zhang, Jingye Zhang, Zhaoshun Gao, Shaotao Dai, Zhifeng Zhang, Dong Xia, Guomin Zhang, Dongliang Wang, Yanwei Ma, Liangzhen Lin, and Liye Xiao. A small 1.5 t persistent current operating test magnet using MgB_2 wire with high j_c joints. *IEEE Trans Appl. Supercond.*, 21(3):1616–1619, 2011.

[20] Susumu Mine, Minfeng Xu, Steve Buresh, Wolfgang Stautner, Christopher Immer, Evangelos T. Laskaris, and Kathleen Amm. Development of a compact 3 t MgB_2 magnet. *IEEE Trans Appl. Supercond.*, 24(3):4400404, 2014.

[21] Susumu Mine, Minfeng Xu, Ye Bai, Steve Buresh, Wolfgang Stautner, Christopher Immer, Evangelos T. Laskaris, and Kathleen Amm. Development of a 3 t-250 mm bore MgB_2 magnet system. *IEEE Trans Appl. Supercond.*, 25(3):4600604, 2015.

[22] Marco Razeti, Silvano Angius, Leonardo Bertora, Daniele Damiani, Roberto Marabotto, Marco Modica, Davide Nardelli, Mauro Perrella, and Matteo Tassisto. Construction and operation of cryogen free MgB_2 magnets for open mri systems. *IEEE Trans. Appl. Supercond.*, 18:882–886, 2008.

[23] M. Modica, S. Angius, L. Bertora, D. Damiani, M. Marabotto, D. Nardelli, M. Perrella, M. Razeti, and M. Tassisto. Design, construction and tests of MgB_2

coils for the development of a cryogen free magnet. *IEEE Trans. Appl. Supercond.*, 17:2196–2199, 2007.

[24] Weijun Yao, Juan Bascuñán, Woo-Seok Kim, Seungyong Hahn, Haigun Lee, and Yukikazu Iwasa. A solid nitrogen cooled MgB_2 "demonstration" coil for mri applications. *IEEE Trans Appl. Supercond.*, 18(2):912–915, 2008.

[25] Weijun Yao, Juan Bascuñán, Seungyong Hahn, and Yukikazu Iwasa. A superconducting joint technique for MgB_2 round wires. *IEEE Trans. Appl. Supercond.*, 19(3):2261–2264, 2009.

[26] Weijun Yao, Juan Bascuñán, Seungyong Hahn, and Yukikazu Iwasa. MgB_2 coils for mri applications. *IEEE Trans. Appl. Supercond.*, 20(3):756–759, 2010.

[27] Dong Keun Park, Jiayin Ling, Matt Rindfleisch, John Voccio, Seungyong Hahn, Juan Bascuñán, Michael Tomsic, and Yukikazu Iwasa. MgB_2 for mri magnets: Test coils and superconducting joints results. *IEEE Trans. Appl. Supercond.*, 22(3):4400305, 2012.

[28] Jiayin Ling, John Voccio, Youngjae Kim, Seungyong Hahn, Juan Bascuñán, Dongkeun Park, and Yukikazu Iwasa. Monofilament MgB_2 wire for a whole-body mri magnet: Superconducting joints and test coils. *IEEE Trans. Appl. Supercond.*, 23(3):6200304, 2013.

[29] Benjamin J. Haid. *A "permanent" high-temperature superconducting magnet operated in thermal communication with a mass of solid nitrogen.* PhD thesis, Massachusetts Institute of Technology, June 2001.

[30] Benjamin J. Haid, Haigun Lee, Yukikazu Iwasa, Sang-Soo Oh, Young-Kil Kwon, and Kang-Sik Ryu. Design analysis of a solid heat capacitor cooled "permanent" high-temperature superconducting magnet system. *Cryogenics*, 42:617, 2002.

[31] H. Kitaguchi and H. Kumakura. Superconducting and mechanical performance and the strain effects of a multifilamentary MgB_2/ni tape. *Superconductor Science and Technology*, 18(12):S248–S289, 2005.

[32] G Z Li, Y Yang, M A Susner, M D Sumption, and E W Collings. Critical current densities and n-values of MgB_2 strands over a wide range of temperatures and fields. *Supercond. Sci. Technol.*, 25:025001, 2012.

[33] Guangze Li, Jake B. Zwayer, Chris J. Kovacs, Michael A. Susner, Michael D. Sumption, Matthew A. Rindfleisch, Chee J. Thong, Michael Tomsic, and Edward W. Collings. Transport critical current densities and n-values of multifilamentary MgB_2 wires at various temperatures and magnetic fields. *IEEE Trans. Appl. Supercond.*, 24(3):6200105, 2014.

[34] Jiayin Ling. Monofilament MgB_2 wires for mri magnets. Master's thesis, Massachusetts Institute of Technology, 2012.

[35] Dong Keun Park, Seungyong Hahn, Juan Bascuñán, and Yukikazu Iwasa. Active protection of an MgB_2 test coil. *IEEE Trans. Appl. Supercond.*, 21(3):2402, 2011.

[36] T. Nakamura, I. Muta, K. Okude, A. Fujio, and T. Hoshino. Solidification of nitrogen refrigerant and its effect on thermal stability of htsc tape. *Physica C*, pages 1434–1437, 2002.